UNIVERSITY OF CALIFORNIA
SANTA CRUZ

DESTRUCTIVE GRAVITATIONAL ENCOUNTERS: OUTCOME AND IMPLICATIONS OF CATASTROPHIC COLLISIONS AND TIDAL SPLITTING IN THE POST-FORMATION OUTER SOLAR SYSTEM

A dissertation submitted in partial satisfaction
of the requirements for the degree of

DOCTOR OF PHILOSOPHY

in

EARTH SCIENCES
with an emphasis in PLANETARY SCIENCES

by

Naor Movshovitz

September 2015

The dissertation of Naor Movshovitz is approved:

Professor Francis Nimmo, Chair

Doctor Donald G. Korycansky

Professor Ian Garrick-Bethell

Tyrus Miller
Vice Provost and Dean of Graduate Studies

Contents

List of Figures

List of Tables

Abstract

Destructive gravitational encounters:
outcome and implications of catastrophic collisions and tidal splitting in the post-formation outer solar system

by

Naor Movshovitz

I present results from three theoretical numerical studies relating to destructive events in the lives of outer solar system satellites and smaller bodies. The first project is a study of the implications that a Late Heavy Bombardment in the outer solar system, such as predicted by the Nice model, might have had for the mid sized moons of Jupiter, Saturn, and Uranus. A Monte Carlo calculation shows that Mimas, Enceladus, Tethys, and Miranda each would almost certainly have experienced at least one catastrophic collision after formation. If true, these bodies would have disrupted and then reaccreted as scrambled mixtures of rock and ice – potentially preserving this signature in their present day structure. Conversely, if these satellites are fully differentiated today then they would have required a heat source sufficient for melting and differentiation in the absence of short half life radioactive elements. Tidal heating may have been sufficient for Tethys, Enceladus, and Miranda, but a differentiated Mimas would present a difficulty to either the Nice model or to the classical formation model of the Saturn system.

The second study is a numerical investigation of the expected outcome of destructive collisions between gravity-dominated bodies; in particular of the conditions required for a collision to be *catastrophic*, defined as one that leaves behind a surviving body with less than half the total colliding mass. In this study I focus on bodies with radii between 100 and 1000 km, a previously neglected size range, and derive a simple scaling law for the threshold impact energy required for disruption in this size range. This scaling law is expected to hold for all projectile-to-target size ratios and is independent of material, so long as elastic strength may be ignored. Compared with scaling laws existing in the literature the newly derived scaling generally predicts lower

threshold energy for disruption, except for highly oblique impacts by projectiles much smaller than the target.

The third project is a study of the tidal breakup of rubble piles by modeling the breakup of comet Shoemaker-Levy 9 in a rigid body code that, for the first time, treats non-spherical rubble pile elements. This introduces dilatation and grain locking as the major forces acting against gravity tides during the comet's close approach to Jupiter and changes the outcome of tidal encounters compared with that predicted by models using spherical elements. By comparing simulation results to the well-studied post-breakup morphology of comet SL9 we were able to constrain the progenitor's bulk density at 300–400 kg/m^3, half that of previous estimates.

Acknowledgments

This section must begin, as my graduate career did, with Erik Asphaug. Erik gave me an opportunity that turned out to be life changing (for the better) and if that had been all it would have been enough. But of course that was not all! Erik continued to provide support, education, opportunity, and friendship throughout my years in grad school and, I expect, beyond. I am particularly grateful for his relaxed advising style which helped me ease into a new life and new work with minimal stress.

Francis Nimmo took over as adviser when Erik moved away. A complete analysis of the ways in which Francis is a great adviser is beyond the scope of this work. I dare say Francis managed to get better quality research out of me than either of us expected. And he deserves special thanks for this because it meant going beyond the call of duty, with a full roster of grad students already depending on him. He makes it look effortless – hopefully it wasn't too bad.

I have worked closely and benefited from discussions with Don Korycansky throughout my time here and in particular over the past two years when we were both using the complex and unfamiliar hydrocode Spheral. Don's expertise in computational fluid dynamics provided a safety net over which I could tinker and experiment with incomplete understanding. Mike Owen is the chief architect of Spheral and without his help this work would not have been possible. I hope he considers the time he spent explaining the complexities of the code to me worth his while.

One cannot do computational science without computers, and I have been a demanding user of computational resources. Ed Boring provided a quick and complete solution to every requirement I had of the Planetary and Marine Computing network, and Shawfeng Dong did the same at the helm of the Hyades cluster. I suspect many of their users are unaware that this level of service is not the standard everywhere.

I learned from and enjoyed conversations with many faculty and students in the department. The planetary lab in particular was my main intellectual circle throughout my time here. Doug Hemingway, Erinna Chen and I spent much time together trying to understand points of planetary physics that we felt were inadequately addressed in textbooks. Tina Dwyer knew things the rest of us didn't and was happy to share. I thank them and hope they remember these conversations as fondly as I do.

Is it a coincidence that the Earth and Planetary Sciences department comprises almost uniformly wonderful individuals? I understand that great research draws great researchers, but why do we also seem to have the friendliest office staff, the most professional support staff, and the best social events? Year after year a new cohort shows up with more brilliant and hilarious students. Around the year 2011 I stopped trying to figure this out and decided to just enjoy the ride.

Previously published material

The text of this dissertation includes modified reprints from previously published material. Chapter 2 is a slightly edited reprint of Movshovitz, N., F. Nimmo, D. G. Korycansky, E. Asphaug, and J. M. Owen (2015), Disruption and reaccretion of midsized moons during an outer solar system Late Heavy Bombardment, *Geophysical Research Letters*, *42*, 256–263. Coauthor Nimmo directed the research. Coauthor Korycansky supported the research with additional simulations and analysis. Coauthor Asphaug provided data and insights from previous research and help with analysis. Coauthor Owen provided the computer code used in all new simulations. Chapter 4 is a slightly edited reprint of Movshovitz, N., E. Asphaug, and D. G. Korycansky (2012), Numerical Modeling of the Disruption of Comet D/1993 F2 Shoemaker-Levy 9 Representing the Progenitor By a Gravitationally Bound Assemblage of Randomly Shaped Polyhedra, *The Astrophysical Journal*, *759*(2), 93, doi: 10.1088/0004-637X/759/2/93. Coauthor Asphaug directed the research. Coauthor Korycansky supported the research with comparisons with previous work.

Chapter 1

Introduction

Collisions are a core component in any theory of solar system formation and evolution. In the inner solar system planetary embryos grow from kilometer sized planetesimals via collisions. Then the host of lunar- to Mars-size embryos becomes unstable and collisions continue until the terrestrial planets are left in their orderly orbits (*Chambers*, 2013). In the outer solar system planetesimals collide to grow the cores of the giant planets until they are capable of accreting and retaining gas directly from the nebula (*Pollack et al.*, 1996). Similar dynamics on a smaller scale most likely then produce the outer planet satellites from the giant planets' own miniature disks.

By the end of the first 100 million years after the formation of the pre-solar nebula, collisions, directed by gravity, had produced the terrestrial and giant planets along with most of their moons, the asteroids, and the comets. But the story was far from over and neither was the role of collisions. The asteroid belt lost most of its mass to a combination of collisional and dynamical evolution (*Morbidelli et al.*, 2009). Infrequent but giant collisions continued to shape the inner solar system; probably giving Earth its large Moon (*Canup and Asphaug*, 2001), possibly taking away Mercury's mantle (*Asphaug*, 2010). Later on migration of Jupiter and Saturn towards a mutual resonance (*Tsiganis et al.*, 2005) may have caused a brief but intense period of renewed chaos in both the inner (*Gomes et al.*, 2005) and outer system (*Barr and Canup*, 2010), when energetic collisions may have modified the surfaces of many satellites. Collisional grinding may have continued for a long time in the Kuiper belt (*Canup*, 2005) and indeed collisions continue, infrequently, to shape planetary evolution, including Earth's in the present day.

This simple story of solar system evolution, of course, contains many still-open questions regarding the details in each of its chapters. How did the first kilometer sized planetesimals form? Where precisely is the transition between accretion and erosion when planetesimals collide? How did the asteroid belt lose so much of its mass? Was there a Late Heavy Bombardment and if so, what caused it? These questions and others remain unsettled because the processes that control them are a complex combination of physics. Advances towards resolving some of these big questions happen incrementally, with answers usually leading to more questions. This dissertation, like many of its kind at this stage of planetary sciences, does not attempt to answer one big question but rather investigates several small and relatively simple ones, adding to the body of knowledge and perhaps, indirectly, to better understanding of our solar system.

This dissertation comprises three reports of relatively distinct investigations sharing the theme of destructive events in the solar system. The first is a report on a Monte-Carlo study of the possible implications of a Late Heavy Bombardment (LHB) on the mid-sized satellites of the outer solar system. We calculated the probability of the satellites of Jupiter, Saturn, and Uranus experiencing at least one catastrophic impact during a hypothetical Late Heavy Bombardment, such as predicted by the Nice model (*Gomes et al.*, 2005; *Tsiganis et al.*, 2005), and find it to be high for many of the smaller or closer-in satellites. In particular Mimas, Enceladus, Tethys, and Miranda would almost certainly have experienced several catastrophic impacts if they existed in their present orbits during the LHB. The cometary mass delivered to the Saturn system would have to be reduced by at least a factor of 30 compared with the value derived from the original Nice Model (*Barr and Canup*, 2010) in order to give Enceladus a decent chance to survive intact, and a factor of at least 100 to give Mimas any chance at all.

If true, this result has some interesting implications. First, these satellites are not large enough to melt and differentiate from the heat of accretion alone, in the absence of short-lived radioactive elements. If disrupted they would have reaccreted as scrambled mixture of rock and ice. Subsequent partial differentiation may have occurred with the help of tidal heating (*Chen and Nimmo*, 2008; *Dermott et al.*, 1988; *Meyer and Wisdom*, 2007), although probably not in the case of Mimas.

Second, some collisions would surely lead to mass loss, as reaccretion is not perfectly efficient, and this mass loss will likely affect the ice-to-rock ratio. This effect would be observable today and perhaps can help explain the diversity of composition among the Saturnian satellites. For

example, ice rich Tethys can be explained as a spall fragment from an impact into a differentiated body (*Asphaug and Reufer*, 2013; *Sekine and Genda*, 2012).

Finally, the surfaces of the disrupted satellites cannot possibly retain an impact history from before the LHB. Surface ages based on crater counts will have to be re-calibrated. In contrast the anomalously cratered surface of Iapetus (*Dones et al.*, 2009) is easily explained, as this satellite is too big and orbits too far to have experienced any disruptive impacts. These implications are discussed in more detail in chapter 2.

The second study, motivated by the first, is a re-examining of catastrophic disruption criteria for gravity dominated bodies. Prompted by a question from a reviewer of the manuscript submitted with the results of chapter 2 we compared the predictions of scaling laws for disruption criteria from existing literature (*Benz and Asphaug*, 1999; *Leinhardt and Stewart*, 2012) as well as our own simulations of impacts between 1000 km radius ice bodies. Finding enough disagreement to cause concern we carried out a thorough study of catastrophic impacts between bodies with radii from 100 to 1000 km, a previously neglected size range.

We derive from these simulation data a simple scaling law for the threshold impact energy required to disperse half the total colliding mass – a common definition of a *catastrophic* collision. This scaling law is expected to hold for all projectile-to-target size ratios and is independent of material, so long as elastic strength may be ignored. Compared with existing scaling laws, the predicted threshold for catastrophic disruption is significantly lower except for highly oblique and very small impactors.

The threshold for disruption by impact is an important parameter in many models of solar system evolution, particularly in post-formation evolution of asteroids (*Morbidelli et al.*, 2009). So called collisional grinding models are used to connect the primordial size distribution of the asteroid belt with the present day one – a connection with possible implications for models of planetesimal growth. Accretion efficiency during terrestrial planet formation also depends, of course, on the conditions that differentiate accretion from erosion (*Asphaug*, 2010). This transition is generally assumed to happen at some fraction of the threshold energy of catastrophic disruption, so that modifying the latter may have interesting implications to terrestrial planet formation as well.

The details of the newly derived scaling law and further discussion of its implications are given in chapter 3.

The last study does not involve a collision but rather a different type of destructive event – tidal splitting. Although less dramatic these events are frequent and interesting as they can be used to constrain basic properties of otherwise inaccessible small bodies.

Tidal splitting occurs when a heliocentric asteroid or comet passes close to a massive body and is sheared and disrupted. In this sense tidal splitting may be considered a type of collision but of course the physics involved is quite different. Gravity is still the main force: differential gravity from the planet driving the shear stresses in the interloper and self-gravity in the asteroid or comet providing the resisting force. But a new force comes into play that is both important and difficult to work with: friction. In so-called "strengthless" bodies, or rubble piles, friction can provide significant resistance to shearing. This is how the details of tidal splitting can be used to infer the properties of the disrupted rubble pile, in particular its bulk density or friction angle.

But friction is difficult to model, analytically or numerically, because it is a complex effect that combines microscopic surface friction and macroscopic grain interlocking and dilatation. Previous numerical models of tidal splitting have simulated rubble piles with collections of spherical elements and were therefore unable to capture these effects. In this work we advance the modeling of rubble- pile bodies by simulating the breakup of comet Shoemaker-Levy 9 during its close approach to Jupiter in July of 1992. We model the progenitor comet with a collection of rigid polyhedra instead of spheres, thus accounting for dilatancy and grain locking as well as elastic response. We obtain a pre-impact diameter of $\sim$1.5 km and a bulk density between 300 and 400 kg/m^3, half that predicted by spheres-based models (*Asphaug and Benz*, 1994).

Tidal disruption by Jupiter is not unusual among the population of short-period comets, as evidenced by numerous crater chains on Ganymede and Callisto (*Schenk et al.*, 1996). Similarly, comets coming too close to the Sun are tidally disrupted, the most famous being the Kreutz family of Sun-grazers (*Knight et al.*, 2010; *Marsden*, 1967). Asteroids, of higher density than comets, can be tidally disrupted as well, but only in encounters with correspondingly denser terrestrial planets. If we regard SL9 as a typical case, we may use the details of its final orbit to infer something about the physical properties of comets in general, and more broadly, about the physics of rubble piles. But perhaps more than a study of a particular event or even a class of events, this work demonstrates the importance of the granular and angular nature of rubble-pile surfaces and the importance of capturing the relevant physical effects in numerical models of

rubble piles.

The details of the model, results, and implications are given in chapter 4.

Chapter 2

Disruption and reaccretion of mid-sized moons during an outer Solar System Late Heavy Bombardment

This chapter is a slightly modified reprint of work previously published as Movshovitz, N., F. Nimmo, D. G. Korycansky, E. Asphaug, and J. M. Owen (2015), Disruption and reaccretion of midsized moons during an outer solar system Late Heavy Bombardment, *Geophysical Research Letters*, *42*, 256–263.

Abstract

We investigate the problem of satellite survival during a hypothetical late heavy bombardment in the outer solar system, as predicted by the Nice Model (Tsiganis, Gomes, Morbidelli, & Levison 2005, Nature 435). Using a Monte-Carlo approach we calculate, for satellites of Jupiter, Saturn, and Uranus, the probability of experiencing a catastrophic collision during the LHB. We find that Mimas, Enceladus, Tethys, and Miranda experience at least one catastrophic impact in every simulation. Because reaccretion is expected to be rapid, these bodies will have emerged as scrambled mixtures of rock and ice. Tidal heating may have subsequently modified the latter

three, but in the nominal LHB model Mimas should be a largely undifferentiated, homogeneous body. A differentiated Mimas would imply either that this body formed late, or that the Nice model requires significant modification.

2.1 Introduction

The lunar Late Heavy Bombardment (LHB; the apparent clustering of lunar basin ages around 3.9 Ga) can be explained by a model (*Gomes et al.*, 2005; *Tsiganis et al.*, 2005) that invokes a period of dynamical instability occurring long after planet formation. In this model, often called the Nice Model, the giant planets are formed in circular orbits, all inside of 20 AU, while an exterior disk of unaccreted planetesimals remains beyond 30 AU. Scattering of planetesimals due to chance encounters results in slow migration of the giant planets until Jupiter and Saturn reach a 1:2 mean motion resonance. The resulting dynamical instability destabilizes both the asteroid main belt and the exterior planetesimal disk. A careful choice of initial conditions can delay the onset of instability to about 700 My after planet formation, delivering enough planetesimal mass to the Earth- Moon system at 3.9 Ga to cause the lunar LHB (*Gomes et al.*, 2005).

The above scenario also predicts an LHB-like period in the outer Solar System. In fact, the higher collision probabilities and impact energies due to gravitational focusing by the giant planets suggest that the inner satellites of Jupiter, Saturn, and Uranus would have experienced a bombardment much more severe than the one supposedly responsible for the lunar basins. The concern is that this outer Solar System LHB should have resulted not just in cratering, but in significant, even catastrophic modification of the smaller satellites (e.g. *Barr and Canup*, 2010; *Nimmo and Korycansky*, 2012). The general vulnerability of the smaller satellites to catastrophic disruption and reaccretion has been noted by previous authors (e.g *Smith et al.*, 1982, 1986; *Zahnle et al.*, 2003), and the probability of satellite survival in the context of the proposed 3.9 Ga LHB was also calculated in (*Charnoz et al.*, 2009). Our contribution is to examine in detail the expected level of destruction experienced by each satellite.

In a previous study *Nimmo and Korycansky* (2012) have shown, using estimates of impactor populations (*Charnoz et al.*, 2009), collision probabilities (*Zahnle et al.*, 2003), and a scaling law for impact-induced vapor production (*Kraus et al.*, 2011), that several satellites (Mimas, Enceladus, Miranda) should have lost most of their ice content during the LHB, unless the total mass delivered to the outer Solar System was a factor of 10 smaller than predicted by the original Nice Model (*Barr and Canup*, 2010; *Dones and Levison*, 2013).

In this work we look again at the problem of satellite survival, this time focusing on disrup-

tion rather than vaporization. We calculate the probability of a satellite experiencing one or more impacts energetic enough to disperse more than 50% of the target's mass (not necessarily vaporized). We find that disruption is much more dangerous than vaporization, particularly for the inner satellites of Saturn. In fact, it seems very unlikely that these satellites could have survived the nominal LHB unmodified in their present orbits.

2.2 Method

For each satellite of interest we ask: What is the probability of it suffering at least one *catastrophic* collision, defined as a collision that disperses at least half the original target mass, during a hypothetical LHB? To answer this question we need to know the total mass of impactors delivered to the target satellite, the statistics of the impactor population (in particular, the size and velocity distribution of impacting bodies), and the effects of a given impact. We consider each of these elements in turn in the following sections, and then describe how they are used in a Monte-Carlo simulation of an outer Solar System LHB.

2.2.1 Total mass of impactors delivered to each target

The Nice model explanation for the lunar LHB requires a rather massive planetesimal disk external to the orbits of the giant planets. *Gomes et al.* (2005) suggest 35 earth masses ($M_{\rm E}$) in the initial disk. From the output of these simulations, several authors estimate the mass expected to strike Saturn between 0.06 and 0.37 $M_{\rm E}$ (*Barr and Canup*, 2010; *Charnoz et al.*, 2009; *Dones and Levison*, 2013). Later studies have suggested ways of reducing somewhat the predicted disk mass (e.g. *Nesvorný*, 2011; *Nesvorný et al.*, 2013). In this work we treat the total delivered mass as a free parameter, spanning the range suggested by previous studies and down to less than one percent of the canonical value.

The mass delivered to each satellite of interest is calculated based on the relative impact probabilities given by *Zahnle et al.* (2003, their table 1). *Zahnle et al.* (2003) report impact probabilities relative to Jupiter, $P_{\rm EC}^{\rm sat}$. We denote by $M_{\rm LHB}$ the total mass delivered to Jupiter, and thus $M_{\rm LHB}^{\rm sat} = P_{\rm EC}^{\rm sat} M_{\rm LHB}$. A satellite's relative probability of being hit scales with the square of its radius and inversely with its orbital distance (assuming an approximately circular orbit and strong gravitational focusing by the primary).

2.2.2 Mass dispersed by an impact[1]

An impact is characterized by the target's mass M and radius R, the impactor's mass m_i and radius r_i, and the impact velocity v_i (in the target's rest frame) and angle θ. We are interested in the gravity regime where material strength may be ignored. For a given target, and for impacts in the near-catastrophic regime, it is customary to make the assumption that the outcome is determined by the specific impact energy $Q = (m_i v_i^2)/(2M)$. More precisely, numerical simulations (*Benz and Asphaug*, 1999; *Leinhardt and Stewart*, 2012) show that, for a given target, the fraction of target mass that remains bound in the largest post-collision fragment is a linear function of Q:

$$\frac{M_{lr}}{M} = \max\Big(0, 1 - 0.5\frac{Q}{Q_D^*}\Big). \tag{2.1}$$

The parameter Q_D^* is the specific energy required to disperse half the target mass, and is a function of the target radius.

In this work we are interested in targets in the 100 to 1000 km range. To extend previous scaling laws for $Q_D^*(R)$ to this range we carried out a series of hydro-code simulations between ice bodies in the gravity regime using the parallel, SPH-based code `SPHERAL` (*Owen*, 2010, 2014; *Owen et al.*, 1998). We simulated impacts into targets with $R = 500$ km and $R = 1000$ km. Target and impactor materials were modeled with a Tillotson equation-of-state using parameters suitable for H_2O ice (*Melosh*, 1989). For each target we ran impacts with several specific energies, and for each value of specific energy we used two impactors ($r_i = 250$ km and $r_i = 200$ km) with different velocities, in order to verify velocity-independent scaling. Fitting a line to the remaining bound mass fraction vs. the specific impact energy, we thus determine $Q_D^*\big(R = 500 \text{ km}\big)$ and $Q_D^*\big(R = 1000 \text{ km}\big)$. Figure 2.1 shows these values next to values obtained previously for smaller targets by *Benz and Asphaug* (1999, their fig. 4), demonstrating a very good agreement between the different codes. (For more detail about the SPH simulations see Appendix A.)

We find that, for ice targets in the gravity regime, Q_D^* is well approximated by

$$Q_D^* \approx 0.05 \text{ J/kg} \times \Big(\frac{R}{1 \text{ m}}\Big)^{1.188}. \tag{2.2}$$

The above scaling law is valid for head-on impacts. Oblique impacts can be handled by consid-

[1]The scaling law used in this section has now been superseded by the work discussed in Chapter 3. In particular, eq. (2.2) should be replaced by the procedure described in sec. 3.5.

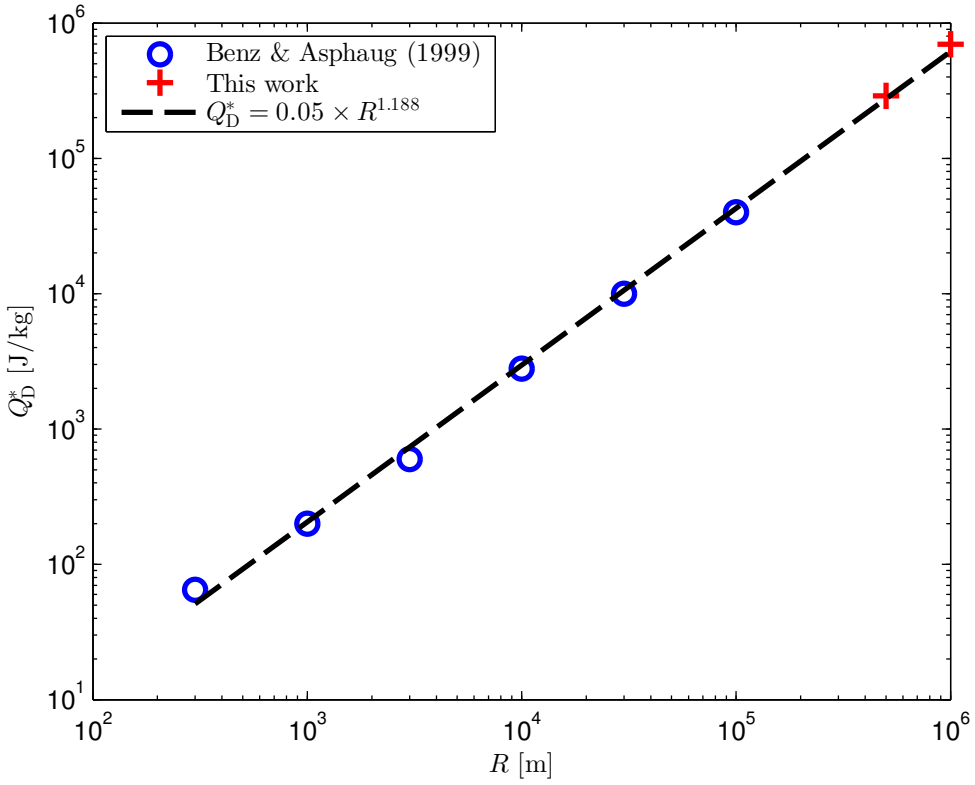

Figure 2.1: Impact energy required to disperse half the mass (Q^*_D) from an ice target in a gravity-dominated collision as a function of target radius (R) obtained from SPH simulations.

ering only the fraction of impactor volume that intersects the target (*Asphaug*, 2010; *Leinhardt and Stewart*, 2012).

Consider, for example, Mimas, the innermost satellite of Saturn. It has a radius of ∼200 km and a mass of $\sim 3.8 \times 10^{19}$ kg. By eq. (2.2), $Q^*_D \approx 10^5$ J/kg. In order of magnitude, the impact velocity of a heliocentric impactor is the satellite's orbital velocity, $v_{\rm orb} \approx 14$ km/s. A single 20 km radius ice impactor at this velocity carries enough energy to disperse half the satellite's mass. In the nominal Nice model Mimas is expected to encounter a total impactor mass equivalent to hundreds of such bodies.

In the high-energy but relatively low-velocity impacts simulated here, the ejected mass is not vaporized. This is not surprising, since significant shock-induced melting and vaporization of ice requires impact velocities higher than ∼8 km/s (*Kraus et al.*, 2011). In our numerical simulations it was necessary to use lower (but still supersonic) impact velocities so that a higher impactor-to-target size ratio can be used – a requirement of numerical resolution. In reality

some vapor production is bound to occur, but most of the mass ejected by the impact will be in the form of large, solid fragments. Unlike vaporized material, these fragments are expected to subsequently reaccrete in relatively short time (see below).

2.2.3 Impactor size and velocity distribution

The simple calculation shown above neglects some important details that may mitigate the destructive potential of a hypothetical LHB. First, eq. (2.1) assumes a gravity-dominated impact. If much of the mass delivered by the LHB came in the form of very small (< 1 km) impactors, we may expect heavy cratering but no significant mass loss from impacts. Second, eq. (2.1) assumes a head-on impact. If much of the delivered mass came in the form of one or two large (comparable to target size) impactors, the angle of impact would play an important role. A chance glancing impact could spend much of the mass budget to minimal effect. We therefore need to consider the statistics of the impactor population.

Third, and most important, eq. (2.1) predicts the mass of material initially escaping the gravity of the target body, but this material is not necessarily gone for good. Heliocentric impactors hit a satellite at roughly the orbital velocity, $v_{\rm imp} \approx \sqrt{3} v_{\rm orb}$. Material is ejected at a range of velocities up to about $v_{\rm imp}$, while the escape velocity from the primary at the orbital distance of the satellite is $v_{\rm esc}^P = \sqrt{2} v_{\rm orb}$. Thus much of the material that initially escapes the target goes into a similar orbit about the primary, and will eventually reaccrete. The timescale for reaccretion depends on the initial spread in semi-major axis given to the ejected material, which in turn depends on the velocity distribution of ejected material (e.g. *Gladman and Coffey*, 2009). But even a conservative estimate puts the reaccretion time scale at no more than some thousands of orbits. This is much shorter than the likely interval between impacts. As a result, although some mass loss may well occur, the main effect of multiple catastrophic impacts followed by prompt reaccretion will be to disrupt any pre-existing structure. We discuss this possibility further in section 2.4.

Impactor size distribution

The Nice model's trans-neptunian planetesimal disk is thought to be the progenitor of the present-day Kuiper Belt. So the currently observed size distribution in the Kuiper Belt can serve as a good starting point for a derived size distribution of LHB impactors. Here we adopt

the size distribution suggested by *Charnoz et al.* (2009), a distribution scaled to match the cratering record on Iapetus and designed to estimate the distribution in the primordial disk. The cumulative fraction N of planetesimals with radius greater than r is assumed to be a power law with two break points:

$$N(r) = \begin{cases} 1, & r < r_{\min}, \\ r_{\min}^{1.5} r^{-1.5}, & r_{\min} < r < 7.5, \\ 7.5\, r_{\min}^{1.5} r^{-2.5}, & 7.5 < r < 100, \\ 750\, r_{\min}^{1.5} r^{-3.5}, & 100 < r. \end{cases} \tag{2.3}$$

where r is measured in km and $r_{\min}$ is an arbitrarily chosen smallest impactor. For a given total mass in the population, the choice of $r_{\min}$ determines the total number of impactors.

With this size distribution, less than 0.2% of the mass is found in bodies smaller than 1 km in radius, justifying our use of energy scaling in eq. (2.1). However, more than 65% of the mass is found in bodies larger than 100 km, and so we must account for the collision angle.

The implementation of this size distribution is described in full detail in Appendix C.

Impact velocity distribution

The probability distribution of impact velocities is described in *Zahnle et al.* (1998) for hyperbolic impactors with isotropic inclinations, and making some assumptions about the planetesimals' velocities at infinity.

The collision angle θ can strongly influence the outcome of a collision. If we assume the canonical $\sin 2\theta$ distribution (*Shoemaker and Wolfe*, 1982), the median collision angle is 45 degrees. In oblique impacts between bodies of comparable size, a significant fraction of the impactor volume is sheared off and leaves the scene largely intact. As a result, a significant fraction of the impact kinetic energy is not coupled to the target, and should not be included in Q when calculating the mass ejected by the impact. We deal with this by following the same procedure as in *Leinhardt and Stewart* (2012), considering only the fraction of the impactor mass in the volume intersected by the target at impact.

Consider again the case of Mimas, but now assume a 100 km radius impactor. This impactor contains about half the mass the Nice model predicts was delivered to Mimas during an LHB.

A head-on impact is easily enough to destroy Mimas many times over. But at an impact angle of 60 degrees only 10% of the impactor volume intersects the target. This effect adds a strong stochastic element to the outcome of an LHB period that we must consider.

2.2.4 A Monte-Carlo model

For each target of interest, we simulate a series of random LHB events and look at the outcome.

An LHB event is defined by the total mass delivered to the target, $M_{\rm LHB}$. This is our main control parameter. We draw a random size, velocity, and angle, from the distributions discussed above. We calculate Q, the effective specific energy of the impact intersecting the target, and Q^*_D for the target. If $Q > Q^*_D$ we increment a catastrophic impact counter. We also keep track of super-catastrophic ($Q > 2Q^*_D$) and ultra-catastrophic ($Q > 3Q^*_D$) impacts, to better quantify how much disruption takes place. The procedure is repeated until the total mass delivered by impacts exceeds $M_{\rm LHB}$. The size of the last impactor may be reduced ad-hoc to avoid overshooting the mass limit.

Note that we make the conservative assumption that any ejected mass is quickly reaccreted. The target's mass and radius thus remain constant throughout the simulation. This approach is conservative since if the target were allowed to lose mass between impacts we would have to adjust its Q^*_D according to eq. (2.2), making it progressively easier to disrupt.

We begin by setting $M^{\rm sat}_{\rm LHB}$ for each target scaled to match $M^{\rm Callisto}_{\rm LHB} = 3{\times}10^{20}$ kg as suggested by *Barr and Canup* (2010). Then we scale down the delivered mass until all saturnian satellites survive their respective LHBs. For each value of $M_{\rm LHB}$ we ran 200 simulations. The resulting statistics are described below.

2.3 Results

Figure 2.2 shows the fraction of Monte-Carlo runs that included at least one collision with energy greater than one, two, or three times Q^*_D, for 11 outer solar system satellites. Mimas, Enceladus, Tethys, and Miranda experienced a catastrophic impact in every simulation. In most runs, Mimas, Enceladus, and Tethys experienced *multiple* catastrophic impacts, including impacts with energy several times that required to completely disrupt the target. These satellites would be heavily modified by an LHB no matter what assumptions we make about the impactor popula-

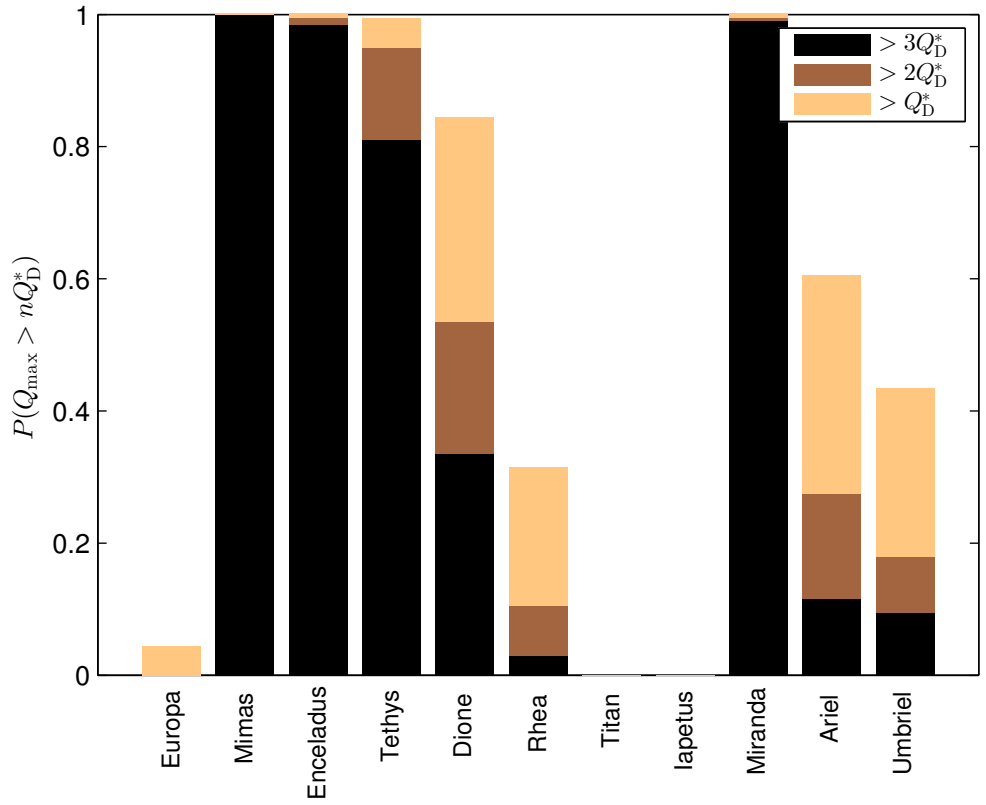

Figure 2.2: Fraction P of Monte-Carlo runs that included at least one impact with effective specific energy greater than one, two, or three times the catastrophic disruption threshold, Q^*_D. In these runs the mass delivered to each satellite was scaled to deliver $\sim 3 \times 10^{20}$ kg to Callisto (*Barr and Canup*, 2010).

tion or reaccretion efficiency. By contrast, the larger satellites (Europa, Ganymede, Callisto and Titan) are not expected to undergo disruption; nor are very distant objects such as Iapetus.

Figure 2.3 shows how the probability of catastrophic disruption drops when the total mass delivered in the simulation is reduced. A reduction by a factor of 3 is not enough to save Mimas or Enceladus, nor, probably, Tethys or Dione. Figure 2.3 shows that the mass delivered by a hypothetical LHB must be at least 30 times less than the value predicted by the Nice model to give Enceladus a decent chance of survival, and 100 times less to give Mimas any chance at all.

The expected number of destructive events and the overall destruction probabilities calculated in our Monte-Carlo simulations are much higher than those previously reported by *Charnoz et al.* (2009, their Table 3). The discrepancy is mainly due to the different values we calculate for the number of impactors larger than a given size expected to hit each satellite. For example,

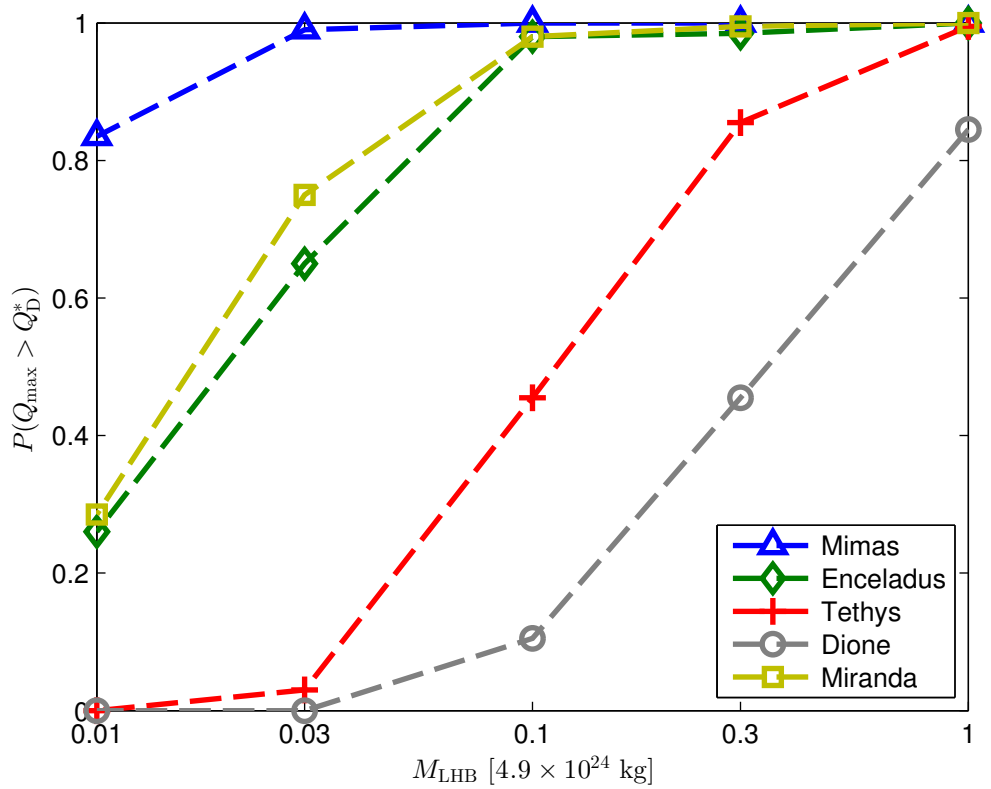

Figure 2.3: Fraction P of simulations that included at least one catastrophic impact, as a function of total mass delivered. The upper limit value corresponds to 3×10^{20} kg delivered to Callisto.

Charnoz et al. (2009, their fig. (8)) calculate that a 200 km satellite at 100,000 km is expected to see about one impact with a 20 km radius comet during the LHB, while a similar body in Mimas orbit is expected to see about 0.57 such comets. In contrast our Monte-Carlo runs, which are scaled from the 3×10^{20} kg striking Callisto, typically result in 30–50 such bodies striking Mimas.

The discrepancy suggests that, for a given primordial disk mass, the total mass that we expect to hit all outer planets and their satellites during the LHB is larger than the value calculated by *Charnoz et al.* (2009). With a primordial disk of 20 Earth masses, the 0.17% probability of impact on Saturn that Charnoz et al. calculate translates to about 2×10^{23} kg striking Saturn, and the relative collision probabilities calculated by *Zahnle et al.* (2003) result in 2.9×10^{19} kg striking Callisto, almost exactly an order of magnitude less than the value suggested by *Barr and Canup* (2010) based on the original Nice Model. There may also be other factors contributing

to the apparent discrepancy.

2.3.1 Caveats

The results given above were obtained using the specific scaling law for Q_D^*, eq. (2.2). This scaling law was derived with hydrocode simulations of impacts, where the equation-of-state (EOS) plays an important role. We chose to use the Tillotson EOS (*Melosh*, 1989) because it was the easiest to implement in our code, not because it is the best available EOS for ice in the pressure and temperature regime of interest (*Senft and Stewart*, 2008). Our simulations were also focused on ice targets: the parameters given to the Tillotson EOS were those appropriate for ice (*Melosh*, 1989). Real targets are likely a mix of ice and silicates, but an appropriate EOS for an unknown mixture of H_2O/SiO_2 is difficult to construct.

To verify the robustness of our results in light of the above caveats, we ran several Monte-Carlo simulations using a different scaling law. From values given by *Benz and Asphaug* (1999, their fig. 3) for basalt targets, we fit

$$Q_D^* \approx 1.48 \text{ J/kg} \times \left(\frac{R}{1 \text{ m}}\right)^{0.9893}. \tag{2.4}$$

For the targets we are interested in, eq. (2.4) yields values that are about an order of magnitude greater than eq. (2.2). Given the mixed composition of most satellites, we may assume that the two end members, eq. (2.2) for pure ice and eq. (2.4) for pure basalt, bracket the real Q_D^* value for any target.

Running our simulated LHBs with this upper limit Q_D^*, we find that the probability of many satellites' experiencing a catastrophic impact remains high. In particular, as shown in figure 2.4, Mimas, Enceladus, Tethys, and Miranda still experience a catastrophic impact in almost every run.

Different scaling laws for gravity regime impacts also exist. *Leinhardt and Stewart* (2012, hereafterLS12) suggest a velocity-dependent scaling law that increases the disruption threshold for high velocity impacts. The LS12 scaling, however, was based on simulated collisions with targets up to 100 km in radius, and does not agree with our SPH simulations of impacts into larger targets (see also Chapter 3). Nevertheless, we ran our Monte-Carlo simulation using the LS12 scaling as well. As expected, the total number of catastrophic collisions experienced by

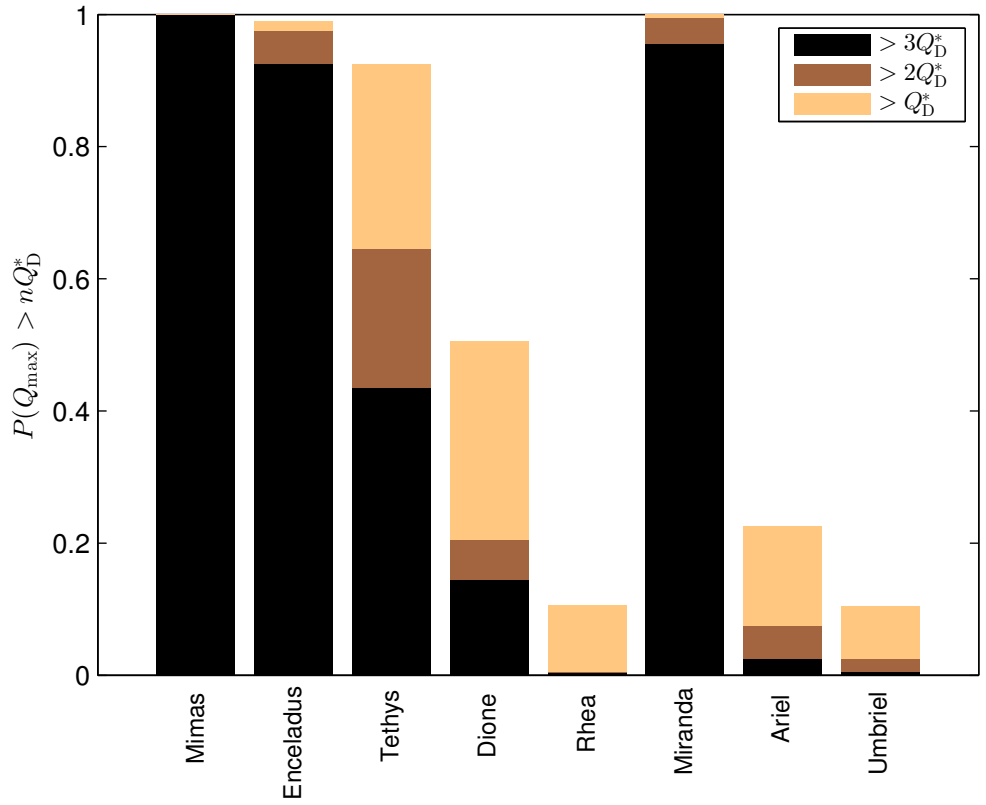

Figure 2.4: Same as figure 2.2 but with from runs using a Q^*_D scaling law derived for basalt targets (see text for details).

each target was reduced. But the probability of experiencing at least one such collision remained almost as high as in our baseline case, so our conclusions given in the following section hold with either scaling law. A direct comparison is shown in Appendix B.

2.4 Implications

Figures 2.2 and 2.3 suggest that the inner Saturnian and Uranian satellites were disrupted (and then re-accreted) several times during the putative LHB. Here we enumerate several consequences of this scenario.

1. The impact history recorded by these satellites prior to the LHB was erased. This conclusion is not in conflict with existing constraints on surface ages based on cratering rate calculations (*Zahnle et al.*, 2003). In striking contrast, Iapetus – which is not predicted to undergo disruption – has an anomalously large number of impact basins (*Dones et al.*,

2009), perhaps reflecting a contribution from the pre-LHB bombardment not recorded in the inner saturnian satellites. The ancient surface ages inferred for Callisto, Umbriel, and Oberon are also consistent with our results, since these bodies are not expected to have undergone disruption. Pluto and Charon may likewise have old surface ages, their distant orbit, large size, and low gravitational potential making them immune to any LHB.

2. Catastrophic disruption and prompt re-accretion is likely to lead to a "scrambled" body in which ice and rock are randomly distributed, and to initially high levels of porosity. For mid-sized satellites, neither the energy of reaccretion nor long-lived radioactive decay are sufficient to cause melting and subsequent differentiation (*Monteux et al.*, 2014; *Nagel et al.*, 2004). Later differentiation could have occurred due to tidal heating (e.g. Enceladus (*Meyer and Wisdom*, 2007), Tethys (*Chen and Nimmo*, 2008), perhaps Miranda (*Dermott et al.*, 1988)), while later impacts would have added ice-rich material to the surface. Nonetheless, the LHB implies that the interiors of Mimas and (perhaps) Miranda are largely undifferentiated. This prediction is potentially testable, because shape or gravity measurements can under certain circumstances be used to derive a body's moment of inertia (*Dermott and Thomas*, 1988). The shape of Mimas is non-hydrostatic (*Tajeddine et al.*, 2014; *Thomas*, 2010), which indicates a relatively cold, stiff body, but does not permit the moment of inertia to be inferred. The shape of Miranda is too uncertain to provide useful information (*Thomas*, 1988).

   Deep initial porosity will be removed by compression over time. However, even on tidally heated bodies like Enceladus, there will be a cold, near-surface layer, tens of km thick, in which porosity can survive (e.g. *Besserer et al.*, 2013). Inactive bodies such as Mimas could potentially have a thicker porous layer, thereby reducing their bulk density.

3. Although our calculations assume complete reaccretion in order to be conservative, collisions are stochastic and some will surely result in mass loss. In particular, for target bodies that are differentiated, the catastrophic collisions which occurred during the LHB are likely to have affected the ice-to-rock ratio. For instance, the apparently ice-rich nature of Tethys can readily be explained if Tethys is a spall fragment produced during a giant impact on a differentiated body (*Asphaug and Reufer*, 2013; *Sekine and Genda*, 2012). The satellites that we see today may in some cases be fragments of their former selves.

4. We have implicitly assumed that the satellites formed at the same time as the rest of the Solar System i.e. prior to the LHB. One way of avoiding disruption is to posit that the inner satellites formed during or after the LHB. *Charnoz et al.* (2011) and *Crida and Charnoz* (2012) suggest that the mid-sized moons of Saturn could have been formed by accretion from a massive, ice-rich ring (*Canup*, 2010) containing large silicate fragments. This scenario is consistent with a late (post-LHB) formation of the inner saturnian satellites and predicts a differentiated Mimas. Indeed, post-LHB satellite formation is a natural outcome if the ring progenitor itself were delivered (or disrupted) by the LHB.

2.5 Conclusions

The canonical Nice model scenario for the LHB (*Gomes et al.*, 2005) will have caused multiple catastrophic disruption and prompt re-accretion of many outer solar system satellites, particularly Mimas, Enceladus, Tethys, and Miranda. None of these bodies (unlike, say, Iapetus or Callisto) will have recorded any events on their surface prior to 3.9 Ga. The interior structures of Enceladus, Tethys, and Miranda may have been affected by subsequent tidal heating events, but the internal structure of Mimas is predicted to be a scrambled, largely undifferentiated jumble of rock and ice. If Mimas turns out to possess these characteristics, then that will provide strong evidence for the scenario outlined here. Conversely, if Mimas turns out to be a differentiated body, then either a heat source post-dating 3.9 Ga capable of causing differentiation but not surface tectonics has to be invoked; or Mimas is younger than 3.9 Ga; or the Nice model explanation for the LHB – when applied to the outer solar system – requires further modification (e.g. *Walsh et al.*, 2012).

Chapter 3

Impact disruption of gravity dominated bodies: new data and scaling

Abstract

We present data from a suite of 169 hydrocode simulations of collisions between planetary bodies with radii from 100 to 1000 km. The data is used to derive a simple scaling law for the threshold for catastrophic disruption, defined as a collision that leads to half the total colliding mass escaping the system post impact. For a target radius $100 \leq R_T \leq 1000$ km and a mass M_T and a projectile radius $r_p \leq R_T$ and mass m_p we find that a head-on impact with velocity magnitude v is catastrophic if the kinetic energy of the system in the center of mass frame, $K = 0.5 M_T m_p v^2/(M_T + m_p)$, exceeds $K^*_{\rm RD} = (3.3 \pm 0.6)\, U_R$ where $U_R = (3/5)GM_T^2/R_T + (3/5)Gm_p^2/r_p + GM_T m_p/(R_T + r_p)$ is the gravitational binding energy of the system at the moment of impact; G is the gravitational constant. Oblique impacts are catastrophic when the fraction of kinetic energy contained in the volume of the projectile intersecting the target at impact exceeds $\sim 1.9\, K^*_{\rm RD}$ for 30° impacts and $\sim 3.5\, K^*_{\rm RD}$ for 45° impacts. We compare predictions made with this scaling to those made with existing scaling laws in the literature extrapolated from numerical studies on smaller targets. We find significant divergence between

predictions where in general our data suggest a lower threshold for disruption except for highly oblique impacts with $r_p \ll R_T$. This result has implications for the efficiency of collisional grinding in the asteroid belt (Morbidelli, A., Bottke, W. F., Nesvorny, D., & Levison, H. F., 2009, Icarus, 204, 558573), Kuiper belt (Greenstreet, S., Gladman, B., & McKinnon, W. B., 2015, Icarus, 258, 267288), and early solar system accretion (Chambers, J. E., 2013, Icarus, 224, 4356).

3.1 Introduction

Collisions between planetary bodies have played a crucial role in the solar system's formation and subsequent evolution. The dynamical outcome of planetary scale collisions has, for this reason, been the subject of much research including theoretical, experimental, and numerical studies. Guided by scaling theory (see the review by *Holsapple*, 1993) many previous studies have reported results from laboratory and computer experiments carried out on portions of the parameter space (an incomplete list includes *Benz and Asphaug* (1999); *Jutzi et al.* (2010); *Leinhardt and Stewart* (2012); *Marcus et al.* (2010); *Stewart and Leinhardt* (2009) as well as reviews by *Holsapple et al.* (2002) and *Asphaug et al.* (2002)). But the huge range in sizes and energies of interest makes a general description of collision outcomes difficult.

A complete characterization of the outcome of a collision is a complex task even with perfect knowledge of the governing physics. The size and velocity distribution of fragments, the amount of melt or vaporization, the pressure history of different parts of the colliding bodies are all of interest in different applications. A more restricted problem that is of prime importance in models of planetesimal growth is the distinction between broad classes of possible collision outcomes: merging, accretion, erosion, or disruption; the definition of these categories being based on the masses of the colliding bodies before and after collision. An even more modest question that is nevertheless of great interest, both in its own right and as a basis for more complete characterization of outcomes, is that of the criteria for *catastrophic disruption* (a precise definition of which is given below). Describing these criteria for collisions involving bodies between 100 and 1000 km in radius is the focus of the present study.

We focus on the 100 to 1000 km size range for two reasons. First, many satellites of the outer planets have sizes in this range, and their origin and evolution were possibly heavily influenced by big impacts during the Late Heavy Bombardment (e.g. *Asphaug and Reufer*, 2013; *Movshovitz et al.*, 2015; *Nimmo and Korycansky*, 2012). Second, this size range seems to have been neglected by previous studies, which have simulated targets either smaller (e.g *Benz and Asphaug*, 1999; *Leinhardt and Stewart*, 2012) or much larger (e.g. *Marcus et al.*, 2010) than the icy satellites. Therefore, applying previously obtained scaling laws (*Benz and Asphaug*, 1999; *Leinhardt and Stewart*, 2012) to mid-sized satellites requires extrapolating beyond the size and velocity range of the simulations used to derive them. The results of such extrapolation, we show below, can

diverge from simulation data.

In the following we present in section 3.2 results from a new suite of hydrocode simulations of collisions involving bodies in the 100 to 1000 km size range and with impact velocities between 1 and 50 km/s. In section 3.3 we suggest a new scaling law that predicts the conditions for catastrophic disruption in this size range. We compare our results to previously obtained data and scaling laws in section 3.4 and summarize our conclusions in section 3.5.

3.2 New simulation data

In this section we present data from a suite of hydrocode simulations aimed at finding the conditions for critically catastrophic collisions (defined below) between planetary bodies in the 100 to 1000 km size range. We give our results first in table form followed by our reduction and interpretation of the data in sec. 3.3.

3.2.1 Definitions

In the size and velocity range of interest collisions are gravity dominated. By this we mean that shock-induced pressure at the impact site, and overburden pressure throughout most of the interior of both the colliding bodies overwhelm elastic strength of the material the bodies are made of. This simplifying assumption allows us to treat the colliding bodies as fluid spheres in hydrostatic equilibrium (prior to impact of course) fully described by their mass, radius, and an equation of state. The compositional difference between different planetary bodies (e.g. mostly icy versus mostly rocky bodies) affects the outcome mostly though the different bulk densities and the resulting gravitational fields. We also assume the colliding bodies are undifferentiated and non-rotating, and that both bodies have a similar composition, although this last assumption, made for convenience, is not critical and will not affect our results.

Note that the above simplifications, while surely unrealistic for many planetary bodies, are perhaps *least* problematic for bodies that are some hundreds of kilometers in size. In this respect the 100 to 1000 km size range is arguably the simplest to investigate numerically. A planetoid much smaller than 100 km in radius is likely to be heterogeneous and may be dominated by elastic stresses while a satellite or small planet much larger than 1000 km in radius is likely to be differentiated and may include strong thermal gradients keeping it away from hydrostatic

equilibrium.

With the above assumptions in mind consider a collision between a body of mass M_T and radius R_T and a second body of mass $m_p \leq M_T$ and radius $r_p \leq R_T$. We refer to the larger body as the *target* and to the smaller as the *projectile*. The relative velocity between the centers of the spheres at the moment of impact has magnitude v. The angle between the relative velocity vector and the line joining the target and projectile centers at the moment of impact is θ, and $b = \sin\theta$. These six initial conditions plus a choice of equation of state (already implied by the assumption of hydrostatic equilibrium) then fully define the collision.

We wish to find initial conditions that lead to *critically catastrophic* collisions, defined as collisions where the largest remaining post-collision gravitationally bound mass, denoted $M_{\rm LB}$, is exactly half the initial mass. Here we run into the first of several ambiguities found in the literature as "initial mass" may refer to either the target mass or the combined target and projectile mass. When $m_p \ll M_T$ it is of no consequence but when $m_p \approx M_T$ either choice can be defended. While considering only the target mass introduces an artificial asymmetry and degeneracy to the definitions, taking initial mass to mean combined system mass leads to the strange result that glancing or "near miss" collision (where both bodies separate mostly intact) are considered catastrophic when $m_p \approx M_T$ and therefore $M_{\rm LB} \approx M_T \approx (M_T + m_p)/2$. Following *Asphaug* (2010) and *Leinhardt and Stewart* (2012) we define a critically catastrophic collision as one that leaves the $M_{\rm LB}$ equal to half the combined mass:

$$f_{\rm LB} = \frac{M_{\rm LB}}{M_T + m_p} = \frac{1}{2}, \tag{3.1}$$

but restrict our discussion to *non-grazing* collisions, with

$$b \leq \frac{R_T}{R_T + r_p}. \tag{3.2}$$

The ad hoc criterion in (3.2) corresponds to the impact angle above which less than half the projectile volume intersects the target if the velocity vector remains constant throughout the collision. We discuss oblique and grazing impacts in more detail in sec. 3.3.

3.2.2 The parameter space

As discussed above, six initial conditions plus an equation of state define a collision. But the assumptions of homogeneity and hydrostatic equilibrium mean that the masses and sizes of the colliding bodies are not independent. A convenient way to explore the parameter space then is to first select the equation of state used to represent the colliding bodies' composition, then choose a target radius in the range of interest followed by a projectile radius some fraction of the target's, then a non-grazing impact angle. A series of hydrocode simulations is then run to find the impact velocity v that leads to $f_{\rm LB} = 0.5$, starting with an initial guess and adjusting the impact velocity up or down as needed. We use this approach to identify, from 169 simulations, 42 critical disruption conditions corresponding to two choices of composition (ice and rock) for 4 target radii, 3–4 projectiles per-target, and 2–3 impact angles per projectile.

Note that different choices are also possible; for example fixing the impact velocity and varying m_p (*Benz and Asphaug*, 1999) or fixing the ratio $\gamma = m_p/M_T$ and varying target and projectile size together (*Leinhardt and Stewart*, 2012). Each option offers some advantages but ultimately the data should cover the same region of parameter space. The main disadvantage of varying impact speed for a given projectile size is that for small targets and large projectiles disruption may happen at subsonic speed. Different physics might govern the coupling of energy to the target at supersonic and subsonic impacts and this may show as scatter in the critical disruption data.

3.2.3 Hydrocode simulations

We use the hydrocode SPHERAL (*Owen*, 2010, 2014; *Owen et al.*, 1998), a Lagrangian SPH based shock physics code coupled with an oct-tree gravity algorithm. We run the code in fluid mode, disabling elastic strength and damage calculations. For an equation of state we implemented the Tillotson EOS (*Melosh*, 1989; *Tillotson*, 1962) with parameters for basalt and water ice taken from *Benz and Asphaug* (1999, their Table 2).

We set the simulation to start at the moment of impact. This saves up considerable computation time but does not allow for tidal forces acting in the hours before impact. For targets in the size range of interest this is not expected to be a significant effect. However, in the upper end of our size range giving the target a constant density at the start of the simulation will result

in local velocities that are due to the layers collapsing or expanding to hydrostatic equilibrium and these particle velocities can be significant. To resolve this we start the simulation with the target and projectile given the pressure profile

$$p(r) = \frac{2\pi}{3} G\rho_0^2 (a^2 - r^2), \tag{3.3}$$

where p is the pressure at radial distance r, ρ_0 is the reference density of the equation of state (at zero internal energy), G is the gravitation constant, and a is R_T or r_p as appropriate. This pressure profile is then inverted (numerically) to yield a density profile that can be used for initial placement of the SPH nodes.

Most of our targets consist of $\sim$50,000 nodes and the number of nodes in the projectile is chosen to match the mass-per-node with that of the target's, typically resulting in a few thousand nodes in the projectile. Higher resolution is possible but we chose to complete more runs in less time and use higher resolution ($\sim$200,000 nodes) periodically as validation. We place the nodes initially in Hexagonal Close Packing arrangement trimmed to a sphere by removing nodes outside a given radius. This arrangement guarantees equal distance between the 12 immediate neighbors of each node and avoids possible artificial singularities that can result from a rectangular grid.

In SPHERAL the smoothing length h for each node is modified every time step by measuring distortions in the local node spacing (*Owen*, 2010) and is not expected to contain a constant number of nodes. We therefore limit the maximum smoothing length, $h_{\max}$, to avoid situations where escaping particles expands their smoothing length to encompass the entire simulation space. Typically $h_{\max}$ is a few times the initial node separation. For consistency, we then need to set a lower limit on node density: $\rho_{\min} = m_i/h_{\max}^3$ where m_i is the characteristic node mass.

We run a collision to a few gravity times, $t_{\text{grav}} = 1/\sqrt{G\rho_0}$, post impact. Immediately following impact the time steps are limited by a sound speed criterion. In later stages it is the acceleration due to gravity that limits the time step. We use a fraction of $t_{\text{acc}} = \sqrt{L/a_{\max}}$ where L is a length scale of the system and $a_{\max}$ is the largest instantaneous acceleration of an SPH node.

3.2.4 Largest gravitationally bound mass

We are interested in collisions that lead to $f_{\rm LB} = 0.5$ and so we need a way to estimate $f_{\rm LB}$. Strictly speaking the definition of $M_{\rm LB}$ requires that we integrate a collision to long times, first with the hydrocode until pressure drops to zero in the ejected mass and then with an n-body integrator until all mass has either collapsed into clumps or has escaped to infinity. This is possible but very computationally expensive and the mapping from the continuous hydrocode to the discrete n-body code is difficult. Instead, we run two predictive algorithms that estimate $M_{\rm LB}$ directly from the instantaneous velocity field established shortly after impact.

The first algorithm follows the procedure suggested in *Jutzi et al.* (2010) for the same purpose. We compute the gravitational potential at the location of each node due to all other nodes and identify the node with lowest (most negative) potential. This is the node that is, in a sense, deepest "inside" the mass distribution. The velocity of this node is used to define a moving reference frame and in this reference frame we locate all nodes with positive mechanical energy. These nodes are discarded and the entire procedure is repeated. The iterative algorithm terminates when a cycle completes with no nodes discarded. Convergence is usually achieved in 5–10 cycles. What remains is a mass distribution that is expected to remain bound except perhaps in some pathological cases. This is a *top-down* algorithm as it whittles down the list of bound nodes from an initial list containing all nodes.

The second algorithm also starts by identifying the node with lowest potential energy and using its velocity to define a moving reference frame. The position of the seed node is denoted $\mathbf{R}_c$, the velocity of the node is $\mathbf{V}_c$, and the mass of the seed node is denoted M_c. In this reference frame we look for all the nodes with

$$E_i = \frac{1}{2}\left|\mathbf{v}_i - \mathbf{V}_c\right|^2 + \frac{GM_c}{\left|\mathbf{r}_i - \mathbf{R}_c\right|} < 0, \tag{3.4}$$

Where $\mathbf{r}_i$ and $\mathbf{v}_i$ are the position and velocity of the i-th node. Then $\mathbf{R}_c$, $\mathbf{V}_c$, and M_c are redefined to be the center of mass position, velocity, and total mass of this list of nodes. The previous step is repeated with the new values, and the algorithm terminates when a cycle completes with no change to the value of these variables. What remains is a mass distribution that is very likely bound except perhaps in pathological cases. This algorithm is *bottom-up*, building a list of bound nodes starting from a single node.

Predictions of $f_{\rm LB}$ by the two above algorithms usually converge within two gravitation times post impact and agree to about 5% or better after that. For consistency, reported $f_{\rm LB}$ values in the following always refer to the average of the values reported by the two above algorithms at $t = 2t_{\rm grav}$. (This is $\sim$8070 s post impact for ice targets and $\sim$4700 s for basalt targets.)

3.2.5 Results

In table 3.1 we give initial conditions for 42 collisions that result in critically catastrophic disruption. For each set of target and projectile sizes, and for each of two choices of composition (reflected in the bulk density and the parameters for the equations of state) and 2–3 choices of impact angle, several runs were needed to identify an impact speed v that leads to $f_{\rm LB} \approx 0.5$ (usually $0.49 \leq f_{\rm LB} \leq 0.51$). The critical value v^* is then obtained by solving

$$f_{\rm LB} = 1 - \frac{1}{2}\left(\frac{v}{v^*}\right)^2 . \tag{3.5}$$

The assumption implicit in (3.5), that near the disruption threshold $f_{\rm LB}$ is linear with v^2, is justified after the fact. (See sec. 3.3.3.) A complete listing of all simulation results is given in Appendix D.

Note that radii given for the target and projectile are the uncompressed values. The values after adjustment to hydrostatic equilibrium will be slightly less. Note also that due to finite resolution the masses of the colliding bodies are not exactly equal to the reference density multiplied by the volume of a sphere.

The values in table 3.1 can be used to explore predictive scaling laws for catastrophic disruption. In the next section we suggest a reduction of the data to a relation between the total system kinetic energy and gravitational binding energy, and use it to propose a best-fit relation in the form of a linear function. We then compare the same data against different possible reductions.

Table 3.1: Summary of collisions found to result in critically catastrophic disruption

EOS	R_T (km)	M_T (kg)	r_p (km)	m_p (kg)	θ (deg)	v^* (m/s)	grazing
basalt	1000	1.128×10^{22}	794	5.68×10^{21}	0	3550	N
basalt	1000	1.128×10^{22}	794	5.68×10^{21}	45	7250	Y
basalt	1000	1.128×10^{22}	500	1.37×10^{21}	0	5230	N
basalt	1000	1.128×10^{22}	500	1.37×10^{21}	30	8010	N
basalt	1000	1.128×10^{22}	500	1.37×10^{21}	45	15600	N
basalt	1000	1.128×10^{22}	300	2.89×10^{20}	0	11600	N
basalt	1000	1.128×10^{22}	300	2.89×10^{20}	30	17400	N
basalt	1000	1.128×10^{22}	300	2.89×10^{20}	45	28100	N
basalt	1000	1.128×10^{22}	200	7.93×10^{19}	0	26800	N
basalt	1000	1.128×10^{22}	200	7.93×10^{19}	30	34100	N
basalt	1000	1.128×10^{22}	200	7.93×10^{19}	45	48300	N
basalt	500	1.395×10^{21}	500	1.38×10^{21}	0	1910	N
basalt	500	1.395×10^{21}	250	1.71×10^{20}	0	3070	N
basalt	500	1.395×10^{21}	250	1.71×10^{20}	30	4490	N
basalt	500	1.395×10^{21}	250	1.71×10^{20}	45	7970	N
basalt	500	1.395×10^{21}	100	9.91×10^{18}	0	14100	N
basalt	500	1.395×10^{21}	100	9.91×10^{18}	30	17900	N
basalt	500	1.395×10^{21}	100	9.91×10^{18}	45	25000	N
basalt	300	3.005×10^{20}	150	3.69×10^{19}	0	2020	N
basalt	300	3.005×10^{20}	150	3.69×10^{19}	30	3100	N
basalt	300	3.005×10^{20}	150	3.69×10^{19}	45	5140	N
basalt	300	3.005×10^{20}	60	2.14×10^{18}	0	8920	N
basalt	300	3.005×10^{20}	60	2.14×10^{18}	30	11600	N
basalt	300	3.005×10^{20}	60	2.14×10^{18}	45	16300	N
basalt	100	1.112×10^{19}	50	1.37×10^{18}	0	868	N
basalt	100	1.112×10^{19}	50	1.37×10^{18}	30	1360	N
basalt	100	1.112×10^{19}	50	1.37×10^{18}	45	2370	N
ice	1000	3.793×10^{21}	794	1.92×10^{21}	0	2200	N
ice	1000	3.793×10^{21}	794	1.92×10^{21}	45	4890	Y
ice	1000	3.793×10^{21}	794	1.92×10^{21}	55	7220	Y
ice	1000	3.793×10^{21}	500	4.65×10^{20}	0	3450	N
ice	1000	3.793×10^{21}	500	4.65×10^{20}	30	4960	N
ice	1000	3.793×10^{21}	500	4.65×10^{20}	45	9690	N
ice	1000	3.793×10^{21}	300	9.81×10^{19}	0	6820	N
ice	500	4.724×10^{20}	500	4.68×10^{20}	0	1190	N
ice	500	4.724×10^{20}	250	5.81×10^{19}	0	1980	N
ice	500	4.724×10^{20}	250	5.81×10^{19}	45	5120	N
ice	500	4.724×10^{20}	250	5.81×10^{19}	60	13000	Y
ice	500	4.724×10^{20}	100	3.36×10^{18}	0	8060	N
ice	300	1.020×10^{20}	150	1.25×10^{19}	0	1340	N
ice	300	1.020×10^{20}	60	7.27×10^{17}	0	5710	N
ice	100	3.775×10^{18}	50	4.64×10^{17}	0	591	N

3.3 A scaling law for critically catastrophic disruption

The conditions identifying a critically catastrophic collision involve six variables[1]. To make sense of the data and to enable predicting the outcome of collision with different initial conditions we would like to reduce the available data to a relationship between fewer variables, derived from the original six.

The choice of the derived variables is not obvious. Certainly the kinetic energy of the projectile is an obvious guess and indeed was often implicitly assumed to be the sole measure of the impact. The momentum of the projectile is another possible measure. *Housen and Holsapple* (1990) examine these assumptions and argue that the correct measure of the projectile is neither energy nor momentum, at least for impacts between strength-dominated bodies where experimental data is available. For our data, experimenting with several options we find that the best measure of the impact is the kinetic energy of system, in the center of mass frame, and that this measure should be compared with the system's gravitational binding energy to determine the outcome of the collision. This is similar to the assumption made in *Davis et al.* (1979, 1985) but we get a better fit to data from comparable size collisions when we consider the kinetic and gravitational energy of the system rather than those of the projectile and target, respectively.

3.3.1 Head-on impacts

Figure 3.1 is a plot of the subset of our simulation data consisting of critically catastrophic, head-on ($\theta = 0$) collisions. Plotted is the variable

$$K^*_{\mathrm{RD}} = \frac{1}{2}\frac{m_p M_T}{m_p + M_T} v^{*2}, \tag{3.6}$$

the kinetic energy of impact in the center of mass frame, against the variable

$$U_R = \frac{3GM_T^2}{5R_T} + \frac{3Gm_p^2}{5r_p} + \frac{GM_T m_p}{R_T + r_p}, \tag{3.7}$$

[1]Strictly speaking the masses and radii are not independent because of the assumption of hydrostatic equilibrium and a certain equation of state. But we choose to keep both variables for each colliding body because they are not easily reduced to each other and, more importantly, it is likely that the conditions for catastrophic disruption, in this gravity regime, are not sensitive to the details of the bodies' interiors but rather depend mostly on the total mass and radius. But this conjecture is not yet tested by simulation.

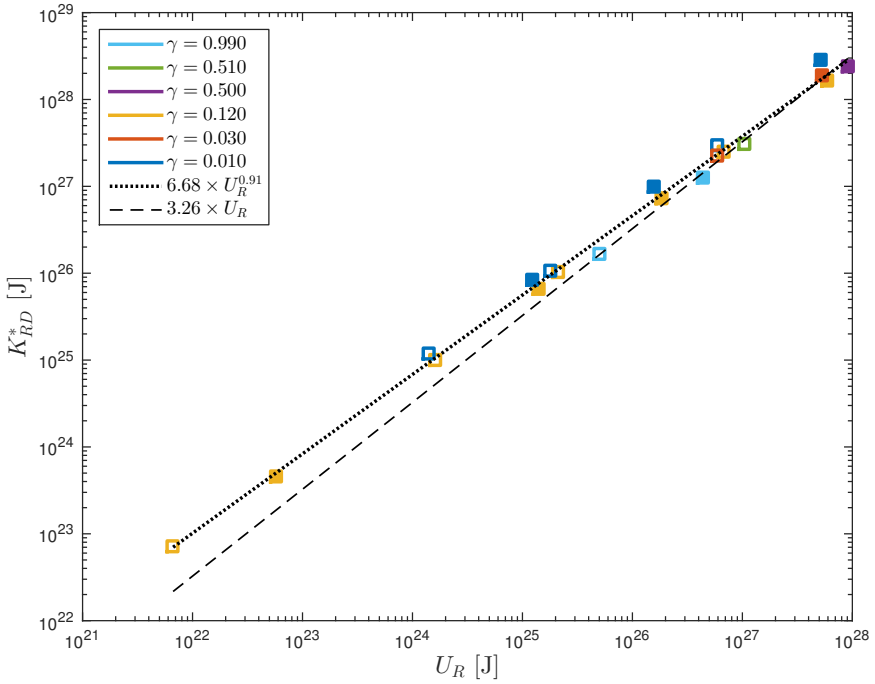

Figure 3.1: Kinetic energy of the system in the center-of-mass frame against the gravitational binding energy of the system at the moment of impact. Filled symbols indicate basalt bodies and empty symbols indicate ice bodies. Color indicates projectile-to-target mass ratio.

the system's gravitational binding energy at the moment of impact. We indicate $\gamma = m_p/M_T$ with color; the values of γ correspond to a projectile-to-target size ratio of between 1 and 0.2. Filled symbols indicate basalt bodies and empty symbols indicate ice bodies. All data seem to fall near a straight line in log scale, suggesting a simple power law relation. In fact the slope of the best-fit line is close to one, suggesting an even simpler, linear relation:

$$K^*_{\mathrm{RD}} = (3.3 \pm 0.6)\, U_R. \tag{3.8}$$

Although the power law with a somewhat shallower slope fits this particular data set better the linear relation is perhaps more physically justified.

3.3.2 Oblique impacts

For the same target and projectile an oblique impact ($\theta > 0$) requires higher speed to reach catastrophic disruption and in general higher θ requires higher v. Part of the reason, for collisions

between similar sized bodies, is a geometric effect (*Asphaug*, 2010; *Leinhardt and Stewart*, 2012). A fraction of the projectile "misses" the target and some fraction of momentum and kinetic energy is not deposited in the target during the collision. Using a simple, idealized geometric model that assumes the bodies are not deformed and the trajectory of the projectile does not change during impact *Leinhardt and Stewart* (2012) give an estimate of the fraction of projectile mass expected to be involved in the collision. If $l = (R_T + r_p)(1 - \sin\theta)$ then

$$\alpha = \begin{cases} \frac{3r_p l^2 - l^3}{4r_p^3}, & l < 2r_p, \\ 1, & l \geq 2r_p \end{cases} \tag{3.9}$$

is the fraction of m_p that is in the volume of the impactor that will overlap with the target if the impactor's trajectory is unchanged. We therefore call αm_p the *interacting mass*.

The interacting mass can be used to provide a zero-order correction when comparing K^*_{RD} for different impact geometries. If only a fraction α of the projectile mass is interacting in the collision then the available kinetic energy is

$$K_\alpha = \frac{1}{2}\Big(\frac{m_p M_T}{m_p + M_T}\Big)\Big(\frac{\alpha M_T + m_p}{m_p + M_T}\Big)v^2. \tag{3.10}$$

(Note that this factor is somewhat different from the one suggested in (*Leinhardt and Stewart*, 2012); a derivation is given in Appendix E.)

The critical disruption value corrected for this geometric effect is denoted $K^{*\alpha}_{\mathrm{RD}}$. Figure 3.2 plots critical disruption energies for impacts at $\theta = 30°$ and $\theta = 45°$ normalized by the value for the corresponding head-on impact. As can be seen, the correction (3.10) accounts for much, but not all of the extra energy required. There is no shortage of possible avenues for the kinetic energy of impact to go into when the impact angle increases and we plan a thorough study of the angle dependence of critical disruption energy in future work. From the data available so far it looks as if, all else being equal, a catastrophic collision at $\theta = 30°$ requires a factor of ~ 2 as much energy as a head on collision, and a collision at $\theta = 45°$ requires a factor of $\sim 3 - 4$ more energy. These estimates are for the *corrected* energy, based on the interacting mass fraction.

It is important to note that the data plotted in figure 3.2 are only those from non-grazing impacts. Grazing impacts are common (*Asphaug*, 2010) and their outcomes are less simple,

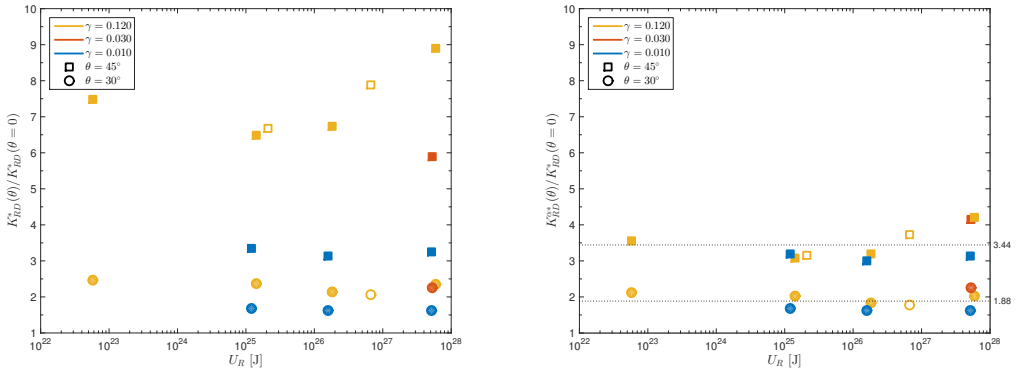

(a) (b)

Figure 3.2: Increase in kinetic energy required for catastrophic disruption with increasing impact angle θ; (a) before and (b) after applying the interacting mass correction, eq. (3.10). Data shown are for non-grazing impacts: $\sin\theta \leq R_T/(R_T + r_p)$. Dashed lines indicate mean values of the post-correction angle dependent factor.

transitioning abruptly from merging to hit-and-run with increasing impact speed.

3.3.3 Near-catastrophic collisions

We have defined a collision as critically catastrophic when $M_{\rm LB} = 0.5(M_T + m_p)$. This definition is merely a convenient reference; no sharp transition between qualitatively different outcomes is implied. Impact conditions that are close to the critical disruption threshold simply result in more or less mass remaining bound. We can be a little more precise by looking at how $M_{\rm LB}$ changes with K_R. A fortunate consequence of the procedure used to obtain our catastrophic disruption data is that we have several values of $M_{\rm LB}$ from *near* catastrophic impact simulations for each row of table 3.1, differing only in impact speed.

Figure 3.3 plots $M_{\rm LB}$ from all 144 non-grazing impact simulations as a function of impact speed v normalized by the critical value v^* for an impact with the same geometry and mass that led to $f_{\rm LB} = 0.5$. It is not surprising that $f_{\rm LB}$ is approximately linear with $(v/v^*)^2)$, when $v \approx v^*$. The usefulness of this relation should not be overstressed. The relation only holds for $v \approx v^*$ and as the exact value of v^* is not known we cannot hope to predict $M_{\rm LB}$ very precisely for a given collision. The best we can say is that if $K_R \gg K^*_{\rm RD}$ we expect the outcome to be supercatastrophic ($M_{\rm LB} \approx 0$) while if $K_R \ll K^*_{\rm RD}$ we expect the outcome to be moderate erosion or even accretion.

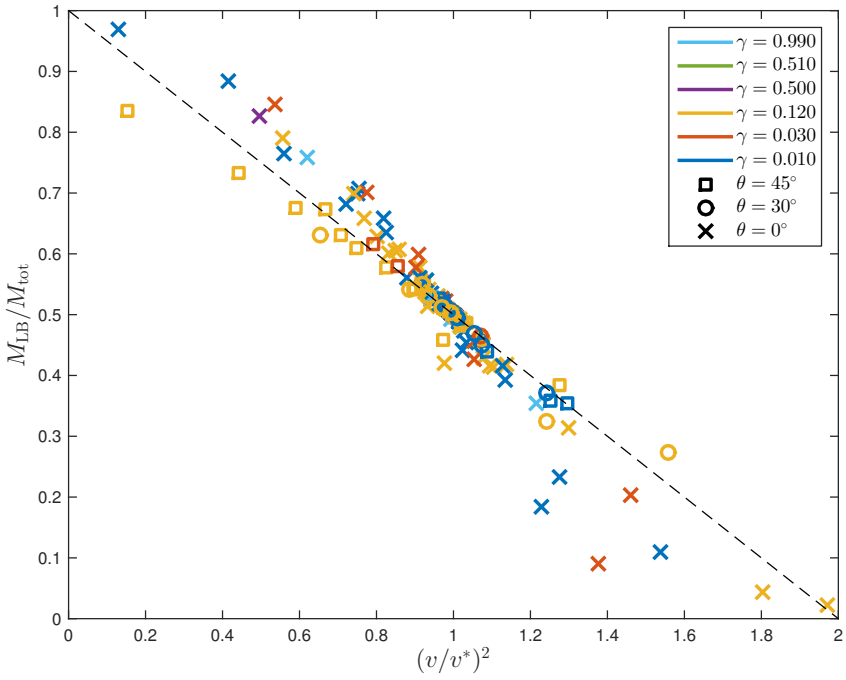

Figure 3.3: Remaining bound mass after near catastrophic impacts as a function of impact speed v. When $v \approx v^*$ the fraction of bound mass post collision is approximately linear with $(v/v^*)^2$.

3.4 Comparison with previous work

As mentioned in the introduction, numerical studies of collisions in the 100–1000 km range are missing but theoretical and numerical studies of collisions between gravitationally dominated bodies in general exist. In this section we compare our data to previously derived scaling laws.

3.4.1 Davis et al. (1985)

Davis et al. (1985) derive an algorithm for the outcome of collision between gravitationally dominated bodies in order to study the collisional evolution of asteroid families. Their algorithm consists of several assumptions. First, they assume that the target body has a material dependent impact strength that is a function of size. The impact strength is defined as the energy density required to shatter the target into fragments the largest of which contains half the initial target mass. *Davis et al.* (1985) propose that this impact strength consists of two terms. The first is the target material's tensile strength and the second, which becomes dominant for bodies

larger than 10–100 km in radius, is due to the overburden pressure averaged over the target's radius.

The second assumption is that the fragment velocity distribution is a power law and that disruption occurs when fragments with velocities greater than the target's escape velocity (presumably at the initial target radius) add up to greater than half the initial target mass. The slope of the velocity distribution is estimated from experimental data and the distribution is normalized with the assumption that some constant fraction of the impact kinetic energy is transfered to kinetic energy of fragments.

The dominant term in the target's impact strength, the term derived from the overburden pressure, increases with the square of the target size, just as the gravitational binding energy. Noting this *Davis et al.* (1985, their Fig. 7) compare, as we do, the collisional energy required for disruption with the gravitational binding energy. But as their algorithm contains several parameters that must be either guessed or extrapolated from experiment (over many orders of magnitude) they cannot get tight constraints for the critical disruption energy; putting the value between 8 and 80 times the gravitational binding energy. Compare this with the value of $\sim$3.3 found in sec. 3.3.1.

Note also that *Davis et al.* compare the kinetic energy of the projectile to the gravitational binding energy of the target, while we compare the kinetic and gravitational energy of the system (fig. 3.1). For $m_p \ll M_T$ this is of little consequence but for $m_p \approx M_T$ the distinction is important.

3.4.2 Benz and Asphaug (1999)

Benz and Asphaug (1999, hereafter, BA99) describe a scaling law for the conditions for catastrophic disruption derived from a suite of simulations generally similar to the ones carried out in this work but for targets with 1 cm $\leq R_T \leq$ 100 km. There are several differences in the details however that should be noted. First, because of the size range of interest the code used in BA99 included explicit treatment of elastic strength and fracture. Second, for practical reasons the code used in BA99 did *not* include self gravity in the dynamical simulations, although a strengthening due to gravity is accounted for in a way similar to that described in *Davis et al.* (1985) (see also *Asphaug and Melosh*, 1993). Third, the impact velocity was kept constant at two chosen values for each of the two material types (basalt and ice with Tillotson's equation

of state, same as here) and m_p was varied instead. Last, simulations were not carried out at or close to the exact conditions for catastrophic disruption. Instead three values of m_p were used for each target (and for each of several values of θ) producing three values of $M_{\rm LB}$. A parabolic fit was then used to predict the projectile kinetic (in the target frame) energy that would lead to $M_{\rm LB}/M_T = 0.5$.

From the data BA99 derive a scaling law based on the variable

$$Q_D^* = \frac{m_p v^2}{2M_T}, \tag{3.11}$$

the kinetic energy of the projectile, in the target frame and normalized by the target mass. Measuring collision outcomes in term of the specific energy, Q, is common in theories of collisional fragmentation. The reason for this is that if $\gamma \ll 1$, and if all simulations or experiments are carried out at the same velocity (varying m_p to find the catastrophic threshold for each M_T), and if the density of the colliding bodies was also kept constant, then $Q_D^*(R_T)$ is expected to follow a power law (*Housen and Holsapple*, 1990).

Figure 3.4 shows the same data as figure 3.1 but plotting the variable Q_D^* against R_T. Also shown for comparison are data from BA99. Figure 3.4 shows that $Q_D^*(R_T)$ indeed follows a power law but only for $\gamma \ll 1$, as expected. Impact with $\gamma > 0.5$ begin to deviate significantly from this power law.

A second weakness of this approach is that it leads to a different power law for each material. While this seems natural and perhaps unavoidable for strength-dominated collisions, in gravity dominated collisions the major property distinguishing one material from another is density, indirectly, through gravity. This is why a scaling law based on gravitational binding energy can be applied without reference to a specific material.

3.4.3 Leinhardt and Stewart (2012)

Leinhardt and Stewart (2012, hereafter LS12) derive a different scaling law based on a different reduction of catastrophic collision data from a suite of particle code simulations of low velocity impacts into targets with $R_T = 10$ km. The main idea behind the LS12 formalism is that with a different choice of variables all the data in figure 3.4 can be made to follow a single power law.

First, LS12 point out that the kinetic energy of interest is really that of the collision viewed

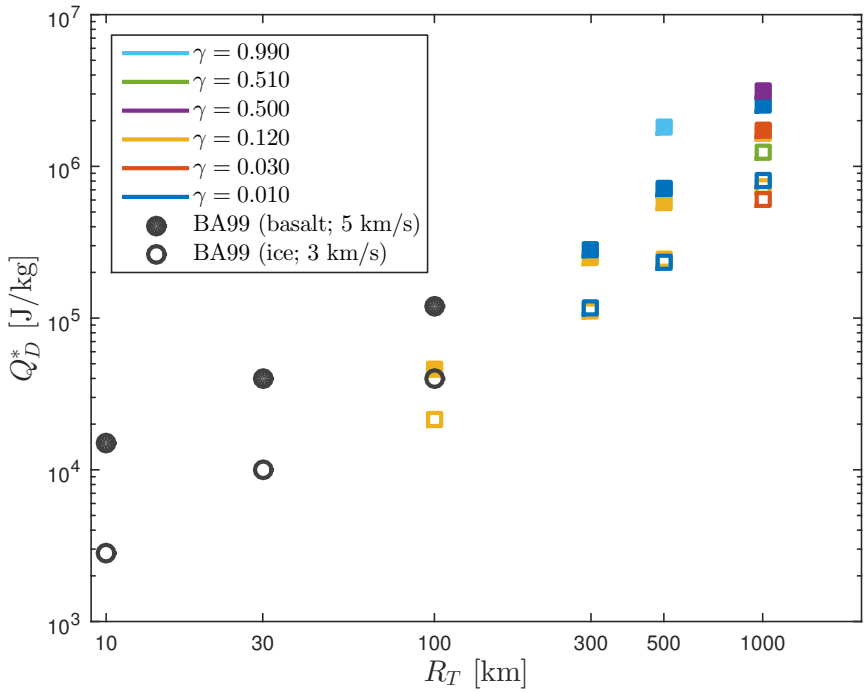

Figure 3.4: $Q_D^* = 0.5 m_p v^2 / M_T$ plotted against R_T for collisions at just the catastrophic threshold. Data from this work (squares) and from BA99 (circles). Filled symbols indicate basalt bodies and empty symbols indicate ice bodies. Color indicates projectile-to-target mass ratio, where known. BA99 mass ratios are not known precisely but are all between 0.001 and 0.01.

in the center-of-mass frame, and further that it should be normalized by the total colliding mass. They therefore suggest the variable

$$Q^*_{\mathrm{RD}} = \frac{M_T m_p v^2}{2(M_T + m_p)^2} \tag{3.12}$$

to replace Q_D^*. (We make the same choice, up to normalization, in eq. (3.6).) In addition, they suggest that scaling Q^*_{RD} using a variable with units of length that measures the *total* colliding mass, instead of R_T, will remove the degeneracy evident in figure 3.4 (several values of Q_D^* for each value of R_T) by taking into account the the projectile size and the different bulk densities of targets with different compositions. The variable they recommend is

$$R_{\mathrm{C1}} = \left(\frac{(M_T + m_p)}{\frac{4}{3}\pi (1000 \text{ kg/m}^3)} \right)^{1/3}. \tag{3.13}$$

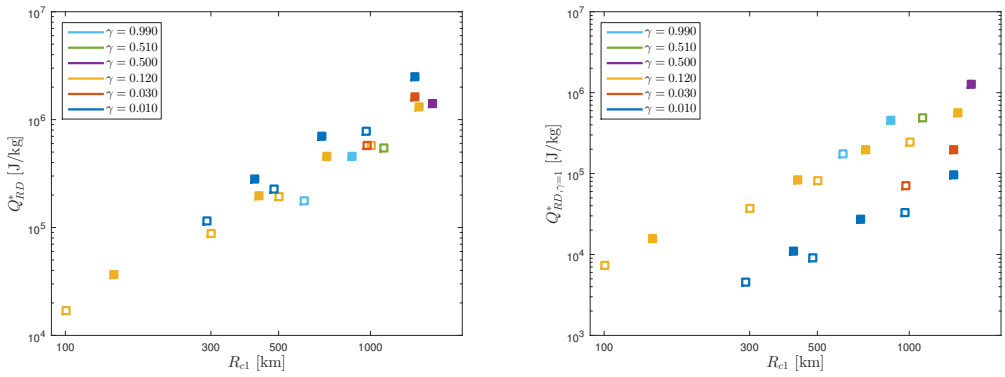

(a) (b)

Figure 3.5: (a) Same data as in fig. 3.1 but plotted using the variables suggested in LS12. (b) Same data after also applying the γ correction, eq. (3.14), with $\bar{\mu} = 0.35$.

When this is done the data indeed squeeze closer together and appear to follow a single power law (figure 3.5a), but with a lot of scatter.

LS12 then derive a correction factor meant to account for different projectile-to-target mass ratios by converting the value of $Q^*_{\rm RD}$ found for a given value of γ to an equivalent value, $Q^*_{\rm RD,\gamma=1}$, the critical disruption energy for a collision where the same total mass is distributed equally between target and projectile. The correction factor is (LS12 eq. (23))

$$Q^*_{\rm RD} = Q^*_{\rm RD,\gamma=1} \left(\frac{1}{4} \frac{(\gamma+1)^2}{\gamma} \right)^{\frac{2}{3\bar{\mu}}-1} \tag{3.14}$$

where $\bar{\mu}$ is the exponent in the coupling parameter (*Housen and Holsapple*, 1990)

$$C = r_p v^{\bar{\mu}} \rho_0^{1/3} \tag{3.15}$$

assumed to be the sole measure of the projectile.

Figure 3.5b shows our data plotted with the variables $Q^*_{\rm RD,\gamma=1}$ and $R_{\rm C1}$ and using the value $\bar{\mu} = 0.35$ recommended in LS12. For values of $\gamma \gtrsim 0.1$ the equivalent equal mass correction appears to work, in the sense that the data collapse to a power law as expected. But data for lower values of γ fall well below the apparent line. (Note that LS12 were limited by the use of a rigid body code to collisions with $v \lesssim 100$ m/s and thus indirectly to $\gamma \geq 0.025$.)

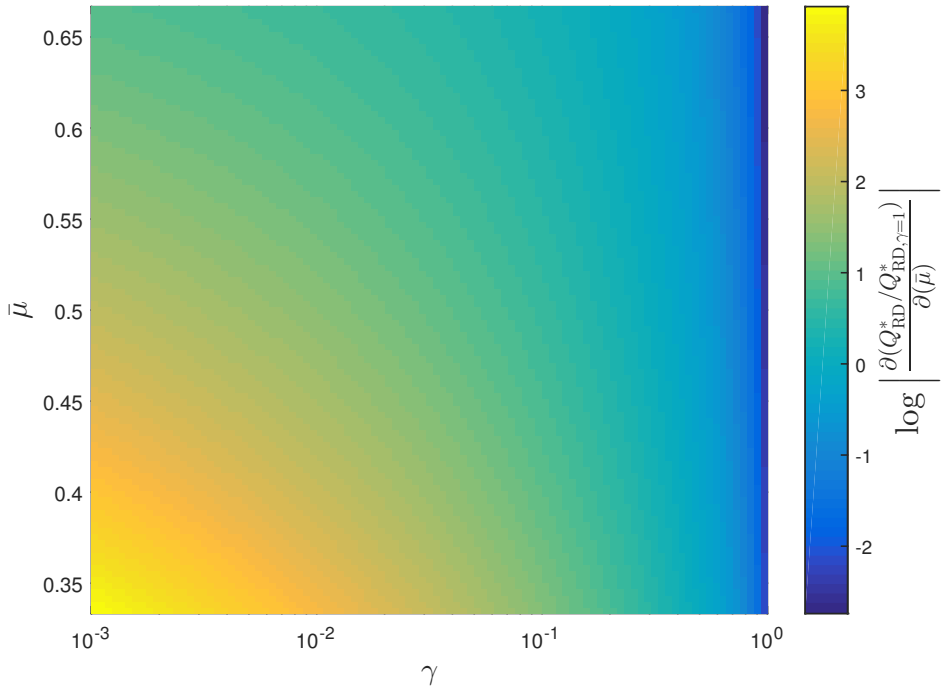

Figure 3.6: Sensitivity of eq. (3.14) to the coupling exponent $\bar{\mu}$.

Eq. 3.14 follows from the assumption that

$$Q^*_{\mathrm{RD}} \propto R^{3\bar{\mu}}_{\mathrm{C1}} v^{2-3\bar{\mu}} \tag{3.16}$$

(*Leinhardt and Stewart*, 2012) which is an extension of a power law,

$$Q^*_D \propto R^{3\bar{\mu}}_T v^{2-3\bar{\mu}}, \tag{3.17}$$

derived from dimensional analysis (*Housen and Holsapple*, 1990, see also a simplified derivation in Appendix F) to the new variables R_{C1} and Q^*_{RD}. However the use of these new variables violates the assumption that the coupling parameter is the only measure of the impact and so eq. (3.14) does not necessarily hold for all values of γ. Note that eq. (3.14) is quite sensitive to the exact value of $\bar{\mu}$ (figure 3.6) and so a value that appears to closely match simulation data for some projectile-to-target ratios can be a bad predictor of disruption conditions for other ratios.

3.4.4 Example

We illustrate the differences between existing scaling laws with the following example. Consider Mimas, the innermost of the major Saturnian moons. Let $R_T = 196$ km and $M_T = 3.8 \times 10^{19}$ kg. If the outer solar system had experienced a late heavy bombardment as predicted by the Nice model (*Gomes et al.*, 2005; *Tsiganis et al.*, 2005) then Mimas may have been struck by cometary material after its formation. Heliocentric projectiles impact at close to orbital speeds (e.g. *Zahnle et al.*, 2003) so let $v = \sqrt{3} v_{\rm orb} \approx 24$ km/s. How big a projectiles is required to disrupt Mimas?

Consider first the scaling law suggested in BA99 (their eq.(6) and table 3). BA99 deal with oblique impacts by averaging the values of Q_D^* obtained for different impact angles, weighted by the probability distribution of θ for isotropic (at infinity) incoming projectiles, and so the projectiles radius we will obtain should be interpreted as the expected size in a statistical sense. But as the impact angle distribution peaks at $\theta = 45^\circ$ the calculated disruption energy will be close to that of an impact at that angle. The BA99 scaling is material dependent but fortunately the low density of Mimas is probably comparable to that of a cometary impactor. We therefore use the BA99 scaling law with parameters for ice targets and take $\rho = 1.2$ g/cm^3. We find $Q_D^* \approx 2.2 \times 10^9$ erg/g and a projectile radius $r_p \approx 18$ km.

Next consider the scaling law in LS12 [2]. Using the recommended values for the parameters and taking $\rho = 1200$ kg/m^3 we find that a projectile-to-target mass ratio $\gamma = 0.0028$ leads to $f_{\rm LB} = 0.5$. The LS12 scaling law assumes a similar density of target and projectile and with this density the projectile radius is $r_p \approx 28$ km. LS12 deal with oblique impacts using an interacting mass correction (slightly different from eq. (3.10)) but for $r_p \ll R_T$ the interacting mass fraction $\alpha = 1$ for almost any impact angle and the predicted r_p for $\theta = 45^\circ$ is the same as that for a head on impact.

Finally, consider the scaling law proposed here. Expecting $r_p \ll R_T$ we neglect the last two terms in eq. (3.7) and obtain $U_R = 2.9 \times 10^{23}$ J. We take $\theta = 45^\circ$, the most likely value, and calculate the kinetic energy for disruption from eq. (3.8) and fig. 3.2. We get 2.8×10^{24} J $\lesssim K_{\rm RD}^* \lesssim 4 \times 10^{24}$ J. Our scaling makes no assumptions on projectile density and we are free to choose it how we want. For comparison with the above calculations we use again $\rho = 1200$ kg/m^3 to find 12 km $\lesssim r_p \lesssim 14$ km.

[2] The authors provide an implementation at http://mygeologypage.ucdavis.edu/stewart/resources/collision/

The diverging predictions of existing scaling laws are significant. Although at first glance a factor of two in size does not seem so bad note that this is almost an order of magnitude difference in mass (and energy!). Moreover, size distributions of typical impactor populations (comets or asteroids) are often steep-sloped power laws (e.g. *Charnoz et al.*, 2009) and $r_p \approx 10$ km projectiles may be much more abundant than $r_p \approx 30$ km ones. If the impact speed is allowed to change the predictions diverge even more, and similarly when oblique impacts between comparable sized bodies are considered.

We note that all three scaling laws used above were derived based on data from simulations at relatively low velocities and the results are therefore extrapolated to higher velocity collisions. However our simulation data is for targets in the 100 – 1000 km range so that we are interpolating rather than extrapolating at least in target radius.

3.5 Summary and discussion

The data in table 3.1 and figures 3.1 and 3.2 suggest the following simple procedure for determining the outcome of a (non-grazing) collision between gravity dominated bodies:

1. Calculate
$$K_R = \frac{1}{2}\frac{M_T m_p}{M_T + m_p} v^2. \tag{3.18}$$
For $m_p \ll M_T$ this is approximately $0.5 m_p v^2$.

2. For oblique collisions calculate also $l = (R_T + r_p)(1 - \sin\theta)$ and
$$\alpha = \begin{cases} \frac{3r_p l^2 - l^3}{4{r_p}^3}, & l < 2r_p, \\ 1, & l \geq 2r_p. \end{cases} \tag{3.19}$$
Then
$$K_\alpha = \left(\frac{\alpha M_T + m_p}{m_p + M_T}\right) K_R. \tag{3.20}$$
Verify also that the collision is not grazing, i.e. that $\sin\theta \leq R_T/(R_T + r_p)$.

3. Calculate
$$U_R = \frac{3GM_T^2}{5R_T} + \frac{3Gm_p^2}{5r_p} + \frac{GM_T m_p}{R_T + r_p}. \tag{3.21}$$

For $m_p \ll M_T$ this is approximately $(3GM_T^2)/(5R_T)$.

4. For head-on impacts, the collision is catastrophic if $K_R > K^*_{\rm RD}$. A nominal value is $K^*_{\rm RD} = 3.3\, U_R$.

5. Oblique (but non-grazing) impacts require higher energy for the catastrophic threshold. For $\theta = 30^\circ$ the collision is catastrophic if $K_\alpha \gtrsim 2\, K^*_{\rm RD}$ and for $\theta = 45^\circ$ the collision is catastrophic if $K_\alpha \gtrsim 3.5\, K^*_{\rm RD}$.

6. Grazing collisions are usually not catastrophic unless the speed of impact is very high. Note however that this does *not* mean that the target and/or projectile are not significantly affected by the impact. It simply means that $M_{\rm LB} \approx M_T$.

We have shown in sec. 3.4.4 that the above procedure can predict outcomes significantly different from those predicted using existing scaling laws (*Benz and Asphaug*, 1999; *Leinhardt and Stewart*, 2012) when applied to collisions in the 100 – 1000 km size range. In particular, our predictions diverge from those of *Benz and Asphaug* (1999) when $\gamma \gtrsim 0.1$ and from those of *Leinhardt and Stewart* (2012) when $\gamma \lesssim 0.01$. Additionally, our new scaling offers the advantage of being material independent and allowing for different densities for target and projectile.

Predictions of the threshold for collisional disruption have applications in many areas of planetary science but are especially important in post-formation evolution of asteroids and small to mid sized satellites. For example, *Morbidelli et al.* (2009) investigate collisional grinding in the asteroid belt in an attempt to connect the present day size frequency distribution with the primordial one – a connection with important implications to models of planetesimal growth. The authors use the scaling law of *Benz and Asphaug* (1999) for basalt targets and find that reproducing the present day observed size distribution requires the primordial belt to be mostly populated by big, $>$ 100 km diameter bodies. They also test their results with a reduced disruption threshold and find a worse fit to observational constraints, with the same initial conditions. It is not easy to guess how using the new scaling presented here would change the predicted primordial size distribution; we only note here that our scaling is consistent with a reduced threshold for disruption compared with BA99 values, especially for 100 km and larger targets.

A second area where a change in disruption threshold may have important implications is the question of a Late Heavy Bombardment in the outer solar system. For example, *Nimmo*

and Korycansky (2012) and *Movshovitz et al.* (2015) investigate the probability of catastrophic disruption of the satellites of Jupiter, Saturn, and Uranus during the LHB, using a disruption scaling similar to that of BA99 for ice targets. Using instead the scaling law suggested here would make these satellites generally more susceptible to disruption. However *Movshovitz et al.* (2015) account for oblique impacts using the interacting mass correction (as in eq. (3.10)) but *without* the additional factor we find here (fig. 3.2). So *Movshovitz et al.* (2015) may have overestimated the destructive power of impactors that are both very oblique and very small. We have verified these assertions with preliminary Monte-Carlo runs using the newly derived scaling law. The output of these is presented in appendix B and confirms the results of Chapter 2.

The Kuiper belt may have some collisional grinding as well, although typical impact speeds are somewhat lower than in the main belt. Recently, *Greenstreet et al.* (2015) estimate impact rates onto Pluto, Charon, and the system's four smaller moons, Styx, Nyx, Kerberos, and Hydra. They use these impact rates to estimate a disruption timescale for the four smaller moons and find that there is only a small probability the these moons had experienced a catastrophic disruption since formation. For threshold disruption energy they use the scaling law of LS12 which in this case is in general agreement with that of BA99. For example, for the satellites Nix and Hydra, assuming a diameter of 45 km and $v = 1.5$ km/s, they use a disruption threshold of $Q^*_{\mathrm{RD}} = 7 \times 10^3$ J/kg to derive a minimum projectile diameter of 8 km for collisional disruption. Our scaling law predicts that a projectile half that size would suffice ($1.3 \leq r_p \leq 2.2$ km). Note however that these small targets are near the lower bound for gravity-dominated bodies and their strength may play an important role.

3.5.1 Future work

Our treatment of oblique impacts was only preliminary. In future work we intend to investigate the impact angle dependence of $K^{*\alpha}_{\mathrm{RD}}$ and provide special treatment of grazing impacts. It is also important to emphasize again that the data and scaling presented here apply only to gravity-dominated collisions. We have not attempted yet to detect the boundary between strength and gravity regimes here. Previous research had put this boundary somewhere between 3 km and 30 km radius. We have therefore stayed on the safe side of the transition with $R_T \geq 100$ km. More simulation data is needed to determine how far down the size range can gravity scaling be used. In principle the same procedure used here can be continued with decreasing values of R_T but

SPH simulations of small, gravity-dominated bodies become increasingly difficult. The difficulty begins with the fact that the SPH formalism works best when all SPH nodes (sometimes called particles) have similar masses. To find the disruption threshold of small targets at high (ideally supersonic) v we must use much smaller projectiles, such that $\gamma \ll 1$. Therefore we are forced to use a very large number of nodes in the target in order to keep the mass-per-node roughly equal between the target and projectile. To make matters worse, the high spatial resolution in the target forces much smaller time steps (the CFL condition) to be taken, but the gravity time scale and therefore simulation end time are unchanged. These effects conspire to make simulations of disruption of $R_T = 100$ km bodies particularly time consuming.

Chapter 4

Numerical modeling of the disruption of Comet D/1993 F2 Shoemaker-Levy 9 representing the progenitor by a gravitationally bound assemblage of randomly shaped polyhedra

This chapter is a slightly edited reprint of work previously published as Movshovitz, N., E. Asphaug, and D. G. Korycansky (2012), Numerical Modeling of the Disruption of Comet D/1993 F2 Shoemaker-Levy 9 Representing the Progenitor By a Gravitationally Bound Assemblage of Randomly Shaped Polyhedra, *The Astrophysical Journal*, *759*(2), 93, doi: 10.1088/0004-637X/759/2/93.

Abstract

We advance the modeling of rubble-pile solid bodies by re-examining the tidal breakup of comet

Shoemaker-Levy 9, an event that occurred during a 1.33 $R_{\mathcal{U}}$ encounter with Jupiter in July 1992. Tidal disruption of the comet nucleus led to a chain of sub-nuclei $\sim 100 - 1000$ m diameter; these went on to collide with the planet two years later (*Chodas and Yeomans*, 1996). They were intensively studied prior to and during the collisions, making SL9 the best natural benchmark for physical models of small body disruption. For the first time in the study of this event, we use numerical codes treating rubble piles as collections of polyhedra (*Korycansky and Asphaug*, 2009). This introduces forces of dilatation and friction, and inelastic response. As in our previous studies (*Asphaug and Benz*, 1994, 1996) we conclude that the progenitor must have been a rubble pile, and we obtain approximately the same pre-breakup diameter (~ 1.5 km) in our best fits to the data. We find that the inclusion of realistic fragment shapes leads to grain locking and dilatancy, so that even in the absence of friction or other dissipation we find that disruption is overall more difficult than in our spheres-based simulations. We constrain the comet's bulk density at $300 \leq \rho_{\rm bulk} \leq 400$ kg m^{-3}, half that of our spheres-based predictions and consistent with recent estimates derived from spacecraft observations.

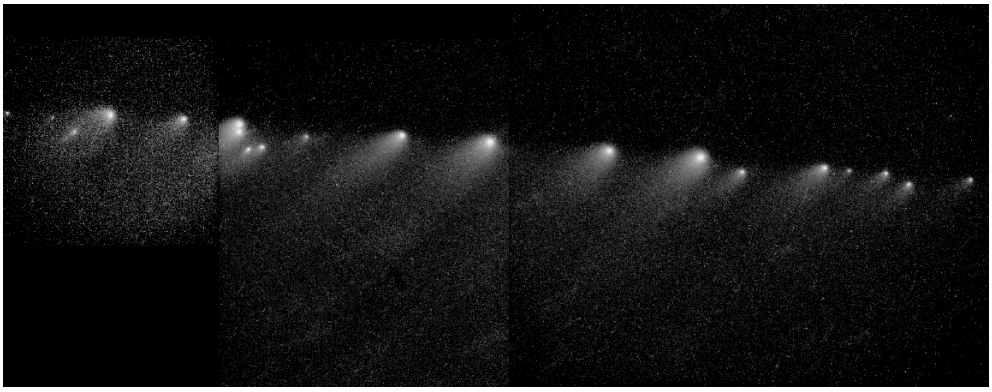

Figure 4.1: Hubble Space Telescope image (*Weaver et al.*, 1995) showing the 'string of pearls' comet Shoemaker-Levy 9 in March, 1994, four months before its collision with the planet Jupiter.

4.1 Introduction

Most kilometer-sized asteroids are likely rubble piles (*Asphaug*, 2009; *Fujiwara et al.*, 2006; *Richardson et al.*, 2002). Many comets may also be strengthless or nearly strengthless bodies, their fragility demonstrated when they break up far from perihelion for no obvious reason (*Weissman et al.*, 2004). One comet was observed shortly after it broke up for a very obvious reason: Comet Shoemaker- Levy 9 (SL9) made a spectacular plunge into Jupiter following a close approach two years previously, that tidally disrupted the original progenitor into at least 21 detectable pieces (Fig. 4.1), as summarized in *Noll et al.* (1996).

Tidal disruption by Jupiter is not unusual among the population of short-period comets. Numerous crater chains on Ganymede and Callisto (*Schenk et al.*, 1996) provide direct evidence for $\sim$10 events where comets disrupted by Jupiter slammed into one of the Galilean satellites. For each such imprint, many thousands of disrupted comets went on to become families of bodies. Similarly, comets coming too close to the Sun are tidally disrupted, the most famous being the Kreutz family of Sun-grazers studied by *Marsden* (1967) and *Knight et al.* (2010). Other planets also disrupt comets, although Saturn's density may be too low to lead to tidal disruption of bodies of cometary density without resulting in a collision. Asteroids, of higher density than comets, can be tidally disrupted as well, but only in encounters with correspondingly denser terrestrial planets. If we regard SL9 as a typical case, we may use the details of its final orbit to infer something about the physical properties of comets in general, and more broadly, about the physics of rubble piles.

4.1.1 Models of Tidal Disruption

A number of studies, conducted before and after the discovery of SL9, looked at the details of tidal distortion and disruption. Most directly applicable was the detailed analytical study by *Sridhar and Tremaine* (1992) who analyzed the tidal stresses exerted on a homogeneous, incompressible, viscous fluid as it passes by a planet on a parabolic trajectory. Assuming that the body remained ellipsoidal during deformation, they concluded that an orbit that results in mass shedding (that is, gravitational instability of the ellipsoid) must have pericenter distance $Q < 1.05(M_{\rm p}/\rho_0)^{1/3}$, where $M_{\rm p}$ is the mass of the planet and ρ_0 is the fluid (planetesimal) density.

Asphaug and Benz (1996) tested, extensively, the possible outcomes of a tidal encounter with Jupiter, for a small body of varying strength and density. They started by showing, using an SPH-based hydrocode with strength (*Benz and Asphaug*, 1994, 1995), that a solid body, no matter how weak, can be ruled out as the progenitor SL9. A solid body was found to break in half, as soon as the tidal stress was able to activate the weakest flaw and propagate a fracture across the body. The stress is thus relieved, and must build up again to an even higher value in the two resulting fragments, which have a higher failure threshold, and have a tidal stress reduced owing to their smaller size. On a nearly parabolic orbit, such as was deduced for SL9, this process is too slow to repeat more than once or twice, no matter how low the initial strength, and so is inconsistent with the > 20 fragments observed for SL9.

Asphaug and Benz (1996) then proceeded to test, using a particle code with elastic collisions, the possible outcomes when the progenitor is instead a rubble pile, with varying density. They first tested their rubble pile (or 'marble pile') code against the analytical predictions of *Sridhar and Tremaine* (1992) and found good agreement for the threshold of mass loss for incompressible fluid bodies on parabolic encounters. With some confidence in the physics of their code based on this good analytical match, they were then able to constrain a bulk density for the progenitor ($\rho \approx 600$ kg m^{-3}) from the resulting chain morphology (number and distribution of fragments). This was well within the allowable range predicted by *Boss* (1994), who predicted $\rho \lesssim 1100 - 2400$ kg m^{-3}. They were then able to constrain a diameter ($d \approx 1.5$ km) from the chain length. They were able to test the effect of friction, in a very simple approach where they froze all relative grain motions until the time of periapse, at which time if the comet was going

to disrupt, this would be the moment of peak stress, after which the modeled comet nucleus was again treated as a pile of frictionless spheres. The corresponding sizes and masses of fragments resulted in good agreement with the best fits to impact plume thermal characteristics observed by the Galileo spacecraft (which was at the time en route to Jupiter, as luck would have it) and modeled using the CTH hydrocode (*Crawford et al.*, 1995).

Earlier studies (*Asphaug and Benz*, 1994; *Solem*, 1994) applied similar models of cometary rubble piles, assuming elastic spheres bound together by only gravity, to derive a density and a diameter for SL9. Both groups obtained similar diameters and densities for the comet. *Asphaug and Benz* (1996) and *Schenk et al.* (1996) furthermore showed that a rubble-pile structure is the only possible explanation to SL9 that also fits the data of cometary disruption remnants imprinted upon the surfaces of Ganymede and Callisto. (Io and Europa have surfaces that are too young to record 'tidal catenae', the chains of craters formed by a tidally disrupted progenitor.)

Similar studies to constrain size, density and internal structure have been conducted for Near-Earth Asteroids (NEAs). *Solem and Hills* (1996) showed how a rubble pile of spherical "rocks", similar to the marble-piles just described, can deform to make an elongated post-encounter shape. *Bottke and Melosh* (1996) approximated a rubble pile asteroid as a rotating contact-binary (that is, two contacting spheres) and found that it takes one or more tidal encounters before impact to sufficiently separate the fragments, if these are to be the source of doublet craters on Earth or on Venus. This paper made the successful prediction that about one-sixth of all near-Earth asteroids are well separated binaries (*Merline et al.*, 2002; *Weidenschilling et al.*, 1989) in proportion to the fraction of primary impact craters that are doublets.

Richardson et al. (1998) used the PKDGRAV N-body particle code to make a thorough investigation of the possible outcomes of a close tidal encounter of a rubble-pile asteroid with the Earth. Their code, discussed further below, represented collisions somewhat more realistically, by including a tangential coefficient of restitution approximating friction, in addition to the normal coefficient of restitution. By considering elongated, rotating progenitors on a hyperbolic trajectory, they were able to peek into three previously closed dimensions of the parameter space. They showed how an elongated progenitor with prograde rotation is far easier to disrupt than a spherical, non-rotating one. Indeed one of their classes of outcomes was designated S-class, for "SL9-type" disruption.

In more recent studies, *Holsapple and Michel* (2006, 2008) have extended the work of *Roche* (1847) and *Jeans* (1917), removing the assumptions of a fluid body with a specific axes ratio and considering instead solid, spinning, ellipsoidal bodies subjected to tidal forces. Using a Drucker-Prager strength model with zero cohesion, parametrized by an angle of friction, they find limit distances for total failure for a long list of special cases, including the case of a stray asteroid passing by a primary. They find that bodies with even a moderate amount of strength can venture much closer to a planet than the classical Roche limit predicts. For example, with an angle of friction $\phi = 30°$ a passing prolate body with aspect ratio $\alpha = \beta = 0.6$ and no spin could approach as close as $d = 1.53\,R(\rho_{\rm P}/\rho)^{1/3}$ without disruption, R being the radius of the primary and $\rho_{\rm P}, \rho$ the densities of the primary and passing body, respectively. Being a static theory, however, the *Holsapple and Michel* theory does not include a possible spin-up of the asteroid as it passes the primary, or the dynamics of disruption when it does occur.

4.1.2 Asteroids and Comets

Two possible tidal catenae are identified on the Moon (*Melosh and Whitaker*, 1994), which would have been caused by the tidal breakup of NEOs (Near Earth Asteroids) around the Earth, crashing into the Moon after a voyage through space of some 30–60 Earth radii depending on whether the collisions happened early or late (*Bottke et al.*, 1997). They occur, as they must, on the Earth-facing hemisphere. In recent LROC images of the Moon there are additional possible examples of smaller catenae that appear to have tidal disruption morphologies, that would be caused by progenitors hundreds of meters across – the size of the rubble-pile, Earth- crossing asteroid 25143 Itokawa (*Fujiwara et al.*, 2006). It is, however, quite challenging to discern tidal catenae from garden-variety catenae that result from the far-flung secondary cratering ejecta common on the Moon; none of these smaller features have yet been validated or reported in the literature, and we remain agnostic.

The possibility of NEO-derived catenae on the Moon is a vital consideration, for if the Moon bears a record of kilometer-sized and smaller tidally disrupted NEOs, just as Ganymede and Callisto bear a record of tidally disrupted Jupiter-family comets (*Schenk et al.*, 1996), then we have the opportunity to learn NEO structural and mechanical characteristics in a manner that can allow for more informed planning of mitigation strategies for potentially hazardous NEOs (*Committee to Review Near-Earth Object Surveys and Hazard Mitigation Strategies Space*

Studies Board, 2010). Until then SL9 is arguably a reasonable proxy for studying rubble-pile asteroids, and perhaps the only available proxy. Asteroids are denser than comets, and Earth is denser than Jupiter by about the same fraction. So the key parameter being the Roche limit, these situations are not dissimilar, to the extent that either body can be represented as aggregates of polyhedra with specified coefficients of friction and restitution (as described below).

So long as the periapse distance is normalized to the Roche limit,

$$R_{\rm roche} = 2.44\ R_{\rm planet}(\rho_{\rm interloper}/\rho_{\rm planet})^{1/3}, \tag{4.1}$$

and the encounter velocity normalized to the escape velocity from the planet at the Roche distance, model outcomes such as those reported by *Asphaug and Benz* (1996) are scale invariant. That is, asteroids passing near the Earth are similar to comets passing near Jupiter (e.g. $\rho_{\rm interloper}/\rho_{\rm planet} \approx 0.3$ for each), and a 1 km rubble pile passing near Jupiter looks the same as a 100 km rubble pile on the same orbit, if the yardstick is 100 times as big. Scale invariance begins to break down when stress dependent parameters such as friction are introduced.

In that sense, the study of SL9 is a rather general study. Of key importance to making further scientific progress in the area of understanding the geophysics of small bodies, the *techniques* used for studying rubble-pile comets and rubble-pile asteroids are identical. What we learn from NEA simulations is useful when we turn to look at Jupiter crossing comets, and we expect that what we learn in this study of a Jupiter family comet to be applicable to any catenae that may be found on the Moon.

Concerning mitigation of hazardous comets and asteroids (*Belton et al.*, 2004) a typical technique is to use an impact or explosion to divert or destroy a body perhaps $\sim 100 - 1000$ m diameter. This involves accelerating material to at least a substantial fraction of the escape velocity of the target body. On Earth, this is 11.2 kilometers per second, much faster than any of the ejecta, so events unfold to completion quickly at the scales of cratering that can be observed in the laboratory or in the field. But on an SL9-sized body, escape velocity is about one meter per second, and the dynamical (self-gravitational) timescale is hours. The opening time of a disruptive collision is also measured in hours, and the speed is comparable to a low-velocity landslide – analogous in many respects to tidal disruption. Thus what we learn about tidal

disruption, is expected to be applicable generally to crater formation and disruption of comets and asteroid and NEOs.

4.1.3 From Marble Piles to Rubble Piles

One common feature of previous dynamical studies of SL9, and of Earth tidal encounters by rubble-pile NEOs, is the use of hard spheres as the building blocks of the simulated rubble pile. Considering the computational capabilities of the time of the Shoemaker-Levy 9 impacts, this was a necessity of being able to model the event at all in a 3D numerical framework: treating the components as radially symmetric and with a simple restitutive potential that balanced self-gravity at resting contact. But this approach does not fully capture the ability of a rubble pile to withstand shear stresses.

When a granular material is under shear stress, the maximum allowable stress before some failure occurs is a consequence of the interlocking of granular particles. This "strength" of the granular material is often assumed to be proportional to the confining pressure, since it results from the interlocking particles having to move each other out of the way, working against the confining pressure. The linear relationship between maximum shear stress and confining pressure is often characterized using a *friction angle* parameter, and it is known, for example, that closely packed, uniform, rigid, frictionless spheres support a friction angle (note the somewhat inappropriate name) of about 23° (*Albert et al.*, 1997). It is also known that this friction angle can be greatly modified (usually lowered) by using a size distribution of spheres, and it could be the case that materials composed of rough, non-spherical grains will also exhibit a different angle of friction, and thus a different response to tidal shearing.

A way to parametrize the effect of interlocking grains while still using spherical elements is to use a *soft sphere* method, such as implemented recently by *Schwartz et al.* (2012). In this method a spring and dashpot force is applied to interacting grains if they experience lateral relative motion, and the strength of the spring can be adjusted to mimic the desired friction angle. We chose to take a complementary approach, and simulate the interlocking directly by modeling a rubble pile with polyhedral grains. Polyhedral grains are expected to display different (likely higher) friction angles, since even rotating a single grain, in place, requires work to be done against the confining pressure. Simulating polyhedral grains, however, is considerably more difficult and computationally expensive than simulating contacts between spheres only. On the

up side, our approach avoids the use of very small time steps that are the hallmark of soft sphere methods.

In the present work we revisit the question of SL9's disruption with much improved computational capabilities and simulation methods. Our logic and procedure are very similar to the studies by *Asphaug and Benz* (1996) and *Richardson et al.* (1998), but with the advantage of faster machines and more versatile algorithms, including public domain and commercial codes originally developed for computer games, that are very well adaptable to the physics of rubble-pile collisions (*Korycansky and Asphaug*, 2009). Our goal, as was theirs, is to constrain SL9's structure, diameter and density, and thereby to gain a fundamental understanding of the physics of comets. Below we describe in detail our procedure and the numerical tools we employ. We then present the results of several sets of runs, and argue that these results suggest a value of $\rho \lesssim 300 - 400$ kg m^{-3} for SL9's bulk density.

But first, we must pause to entertain the notion that this is not the final answer to be obtained by N-body methods – that in another fifteen years, another paper will come along with still better methods, and claim a density half again smaller for SL9, defending our present attempts as what one would do with the crude technology of the early 2010s. We do not believe this to be the case, but we wish to emphasize the importance of finding benchmarks for these kinds of codes at every opportunity, including in space station experiments and other stable microgravity research platforms. The limitation to spherical particles was a fundamental one which is now lifted. Given that our results are only weakly dependent upon friction and restitution (see below), it appears that the major distinction between the models of the 1990s and our present models is the aspherical geometry, leading to grain stacking and dilatancy that limits grain motion. The next steps in granular modeling will be in even more detailed irregular shapes (e.g. with fractal-like rather than planar surfaces) and the inclusion of cohesion forces. However we can argue (though not perhaps convincingly, even to ourselves) that fractal-like surfaces, i.e. roughness, are already well represented in the planar friction model, and that cohesion was already ruled out on the basis of the 'string of pearls' morphology of the post-disruption SL9, indicative of a self-gravity dominated process (*Chandrasekhar*, 1961; *Hahn and Rettig*, 1998), and in the scale-invariance of the catenae on Ganymede and Callisto (*Schenk et al.*, 1996). But granular physics is still a young science and there may yet be devils in the details.

4.2 Method

4.2.1 Discrete Element Models

We employ DEM models using randomly shaped polyhedra as building blocks of the simulated rubble pile, with resolution much higher than previously applied to this problem. By using these polyhedral "grains" our models are attempting to directly simulate the cause of granular friction. As mentioned, *Asphaug and Benz* (1996) represented a maximal friction by not allowing any inter granular movement until the comet nucleus had arrived at periapse, on the premise that sliding friction is much lower than static friction. However the shapes of grains require work to be done in moving adjacent grains out of the way, in order to rotate, so that continuum shear is resisted by a force that may be called *dilatation*, to distinguish it from the Coulomb friction applied at the surface of the grains[1]. This force can only be directly simulated with non-spherical grains, as spherical grains are free to roll in place without resistance, unless this resistance is parametrized and explicitly supplied by the code, as in soft sphere methods.

It is easy to understand why we obtain, when all is said and done, a lower density than before. Friction resists the tidal shear stress, in a sense substituting for density (self-gravity) as the force that is holding the comet together against disruption. Friction being a short range force, and gravity being a long range force, their interplay defines the final morphology of the fragment chain, and thus we can still obtain a unique solution, even if the effect of friction influences our choice of bulk density.

The main difficulty when moving from a spheres-based simulation to more complex shapes is the implementation of a fast contact detection algorithm. The direct approach of solving the geometric equations for each side, vertex, and face of every element is out of the question. Fortunately there are better algorithms. GJK (*Gilbert et al.*, 1988) is perhaps the most popular as it operates in linear complexity (with the number of vertices for two convex objects) and can handle collisions between curved and polyhedral shapes. The challenge then becomes implementing the geometric algorithm in the most efficient way. As rough shapes necessarily

[1]It may be argued that the microscopic origin of Coulomb friction is simply the same dilatation effect at work on a smaller scale. In this work we use the term *dilatation* when the effect is the direct result of our very macroscopic grains interlocking. The use of polyhedral grains with flat faces also opens the possibility that grains will slide across each other much as a rectangular box slides down a sloped floor. In our models this is treated by applying a friction force to the surface of the interacting particles, parametrized by a coefficient of friction. Since these two effects are not easily distinguishable in our model, and since both are linearly proportional to the confining pressure, we often refer to the combined effect resisting shear as friction.

have many vertices, even a linear algorithm quickly becomes too slow when too many shapes are compared against each other. Collision detection must be followed by collision resolution (that is, physical treatment of the collision as before-and-after states). Although this is a well studied part of classical mechanics (e.g., *MacMillan*, 1936) it is again not simple to implement an optimal algorithm that can handle collisions (with and without friction) and resting contacts with minimum operations.

Fortunately, a vast amount of research into optimal collision detection and resolution has come out of the computer games industry. These algorithms are the main components of what the video game industry calls *physics engines*. Physics engines are at their core DEM simulations, and the financial incentive of the industry has resulted in the development of a number of reasonably accurate, but *very* fast implementations. The risk in adopting such physics engines is that what is good enough for a game, may not be good enough for science. On the other hand, a number of these engines have been found to be excellent in their accurate physical treatment of elastic collisions between objects with complex shapes (*Longshaw et al.*, 2009). In the present work we have used for the most part NVIDIA's PhysX engine[2], comparing it in key instances with the previous model of *Korycansky and Asphaug* (2009) utilizing the publicly available Open Dynamics Engine.

The PhysX engine combines rigid body dynamics and collision detection (and many other potentially useful features) in a single library, making it very easy to use as a basis for a DEM simulation. Among other rigid-body libraries, it stands out in terms of performance and stability. This high performance comes at a cost, however. PhysX uses single-precision floating-point numbers, and a first-order forward Euler scheme for dynamic integration. Being a closed source product (although free to use and distribute in binary form) these and other choices are not easily modified without acquisition of the source code or direct collaboration with its developers. What single precision, first order solution means in practice, is that we must be careful to chose small enough time steps for integration, much smaller than used in sophisticated state-of-the-art N-body integrators. We determine the appropriate time step by careful analysis of conservation in test simulations.

[2] http://developer.nvidia.com/physx

4.2.2 Validation

Over the past two years we have validated the correct behavior of the PhysX rigid-body module in simple and complex, dynamic and static scenarios. To validate the elementary rigid body physics, we performed a suite of fairly simple tests. A rotating-tumbling body with a full moment of inertia tensor was used to verify the correct integration of Euler's equations. A point mass orbiting in a central gravity potential verified the force and acceleration integrator, but more than 1000 time steps per orbit were required to maintain better than one percent conservation of orbital energy. Note that this is much worse than is possible with higher order integrators.

The planar friction model was validated by simulating a box sliding on an inclined plane. The box begins sliding at an incline angle θ where $\tan\theta = \mu$, the friction coefficient, and this behavior is independent of the acceleration of gravity as long as a time step is chosen that is not short enough to underflow the velocity change. A bouncing ball verified the conservation of energy and the correct handling of a restitution coefficient, ε, the ratio of relative speed of separation to the relative speed of impact, with the exception of *perfectly* elastic bodies ($\varepsilon = 1$) that can lead to unstable behavior over time.

Conservation of linear and angular momentum during collisions was also validated. Here two bodies with random shapes and sizes are set on a collision course and linear and angular momentum are measured before and after collision. Linear momentum is always conserved accurately. As for angular momentum, we found that bodies with simple, smooth shapes conserve angular momentum very accurately. However, the binary collision between two irregular, polyhedral shapes can lead to a change of the binary system's angular momentum vector by up to 30% in magnitude, perhaps corresponding to an approximation made in the collision detection. This is disappointing, and is possibly the result of an approximation made in the interest of speeding the engine[3]. The error, however, is randomly oriented, so that an ensemble of many bodies always conserves its total angular momentum very well.

This led to tests of more complex physical systems involving aggregates of bodies. We

[3]After publication I discovered the reason this apparent change in angular momentum during a collision was in fact a simplification in the way PhysX time steps a torque-free rigid body. In the interest of optimization, rather than integrate the full Euler equations the PhysX engine maintains a constant spin vector (relative to inertial space). This means that the angular momentum vector of an asymmetrical body precesses around a mean value. Angular momentum is in fact conserved in collisions, but is not constant *between* collisions. I can only speculate that this simplification leads to performance gains important enough to justify the unphysical behavior of asymmetrical bodies. This simplification is not of concern in this work, but we should remember that the PhysX engine in this form is not capable of simulating tumbling behavior of individual elements.

used PhysX to simulate an avalanche of polyhedral dice, beginning with a simple laboratory simulation where we let a tall pile of 1400 12-sided dice (the kind familiar to a different kind of gamer) collapse, in 1g, to a stable slope in a transparent rectangular container. We measured the average slope angle with a ruler. This process was then simulated with PhysX, for the same boundary geometry, and we found an excellent agreement between the measured and modeled angles of stable slope. This is particularly important because the slope angle depends on the correct application of sliding friction and resting contacts between grains.

We have also performed several of our simulations using a second implementation of a DEM, based on the Open Dynamics Engine (*Korycansky and Asphaug*, 2009), a DEM that uses different algorithms, and the results from both codes are always similar, although PhysX is an order of magnitude faster, thus allowing for much higher resolution simulations.

As in (*Asphaug and Benz*, 1996) we do not hope to resolve every actual granule in a cometary nucleus. At best, our grains are tens of meters across, representing an assemblage of much smaller particles. Even with billions of grains, we would simulate SL9 with at best meter-sized objects, when in fact comets may be composed of dust and ice. We merely hope to resolve the granular behavior at a scale smaller than the deformation occurring within the tidally disrupting cometary nucleus. *Asphaug and Benz* (1996) found similar behavior, with increasing N, once the comet was resolved with more than several hundreds of spheres. We likewise find similar behavior, but converging at higher 'resolution' (several 1000s polyhedral grains), owing to the fact that the grain-grain interactions are more complex. We note, however, that increasing the number of grains in a simulation will be necessary to test the effects of different grain size distributions, another potentially important dimension of the parameter space, not explored here.

We caution that 'resolution' is not really the appropriate word here, because even in the limit of infinite numbers of grains we are not resolving a continuum. Indeed at infinitesimal grain diameter the material would have infinite friction. Rather, each simulation, for a given N, is actually a somewhat different physical system. But as long as we have enough grains to simulate the inter granular effects such as dilatancy and stacking, and the frictional forces, further increases in N do not make any apparent difference in our primary scientific result, the determination of the density of SL9, or in the physical and morphological behavior of the comet's tidal disruption. Insofar as we can adequately capture shear friction in a granular mass, and insofar as we can capture the physics of dilatancy caused when rubble expands during shear

(requiring energy), the approach is likely to capture the most significant physical aspects of the tidal disruption of rubble piles.

4.2.3 Simulating tidal encounters

A rubble pile is simulated in a DEM by a collection of rigid body elements we call *grains*. We make a rubble pile by letting a collection of randomly shaped polyhedra collapse freely into a roughly spherical aggregate. Making a kilometer sized body out of several thousands elements, means that each element is ~ 100 m in size. (We use a uniform, narrow size distribution, intended only to inject more randomness to the grain assemblage. The smallest grain has a bounding sphere about half the diameter of the largest grain's bounding sphere.) An actual cometary rubble pile is surely made of a wide distribution of grain sizes, with the near-surface grains likely much smaller than a meter in the case of comets (based on imaging and thermal inertia data,e.g. *Fujiwara et al.*, 2006). Although this limitation is important to keep in mind, the essential physics of the process we investigate, namely granular shear flow, presents itself at these larger grain sizes. We cannot yet say whether or not a more realistic size distribution would lead to significantly different behavior but sec. 4.3.1 describes the convergence of behavior within our resolution limit.

When the "comet" is ready, we send it on a pre-calculated orbit past Jupiter. The orbit of SL9 was an almost parabolic orbit with eccentricity $e = 0.997$ and perijove $q = 1.33$ Jupiter radii (*Sekanina et al.*, 1994). To allow for pre-encounter tides, and to follow it out to dynamical completion, we calculate the comet's orbit between four Roche limits pre-perijove, and 15 Jupiter radii post- perijove. Thus the simulation starts before any significant tidal force is felt by the comet, and continues past the orbit of Ganymede. The orbit is divided into equal time steps of one thousandth of the dynamical time, $dt = 10^{-3}(2\rho G)^{-1/2}$, where G is the gravitational constant and ρ stands for the comet's average density, not the material density of grains. The average density is in fact the main control parameter of the simulation, and we set it by adjusting the individual grain masses after determining the approximate volume of the body.

For reasons of numerical accuracy, the simulation is done in the frame of reference of the comet. In every time step, the net force on each grain is calculated by adding the gravitational attraction from all other grains (computed pairwise), the gravitational attraction of Jupiter, whose position is read from the pre-calculated orbit, and the fictitious force from the non-inertial

comet- centered frame. These external forces are applied at each time step to every grain, while the accelerations resulting from collision between grains, as well as the time integration, are handled by the PhysX library. As mentioned, the conservation of energy and momentum are validated as described above, as well as the friction forces, and angular momentum is validated for interactions averaged over assemblages of grains.

The result of a typical test run with 4096 grains is shown in figure 4.2. The position of each grain is plotted in the plane of the orbit (the out-of-plane extent of the fragment train is relatively small). Red circles mark clusters of grains, somewhat subjectively defined as groups of touching or nearly touching grains with at least one per-cent of the mass of the initial body. (The red circles are just a visual aid, they have no physical meaning.) By this stage the clustering had completed, and the fragments continue to separate at a rate determined by simple, two-body orbital dynamics. (Non-interacting particles along the same parabolic orbit separate at a rate proportional to a 4/3 power of time [*Sridhar and Tremaine*, 1992] .) Once beyond the Roche limit of the planet, for appropriate bulk density rubble piles we see the signature SL9 'string of pearls,' i.e., a well separated, roughly linear train of more than a few, roughly equal sized fragments. The self-gravitational clumping instability that forms these new cometary nuclei was described by *Chandrasekhar* (1961) and by *Hahn and Rettig* (1998).

This clumping is a sensitive measure of progenitor density. Starting with an over dense progenitor, the outcome would instead of the above figure, be one or two large fragments containing almost all the mass of the comet. Conversely, if the progenitor's density was too low, no clustering would occur and the comet would "atomize" into individual boulders, gravels and dust. Because we know the encounter orbit so precisely (*Chodas and Yeomans*, 1996) it is possible to constrain the average density of SL9 in this manner. Although the classification of a given outcome is somewhat subjective (too few fragments, too many fragments, or just right) the two end members are easily and unambiguously spotted (see Sec. 4.3.2), leaving a narrow range of possible densities in between.

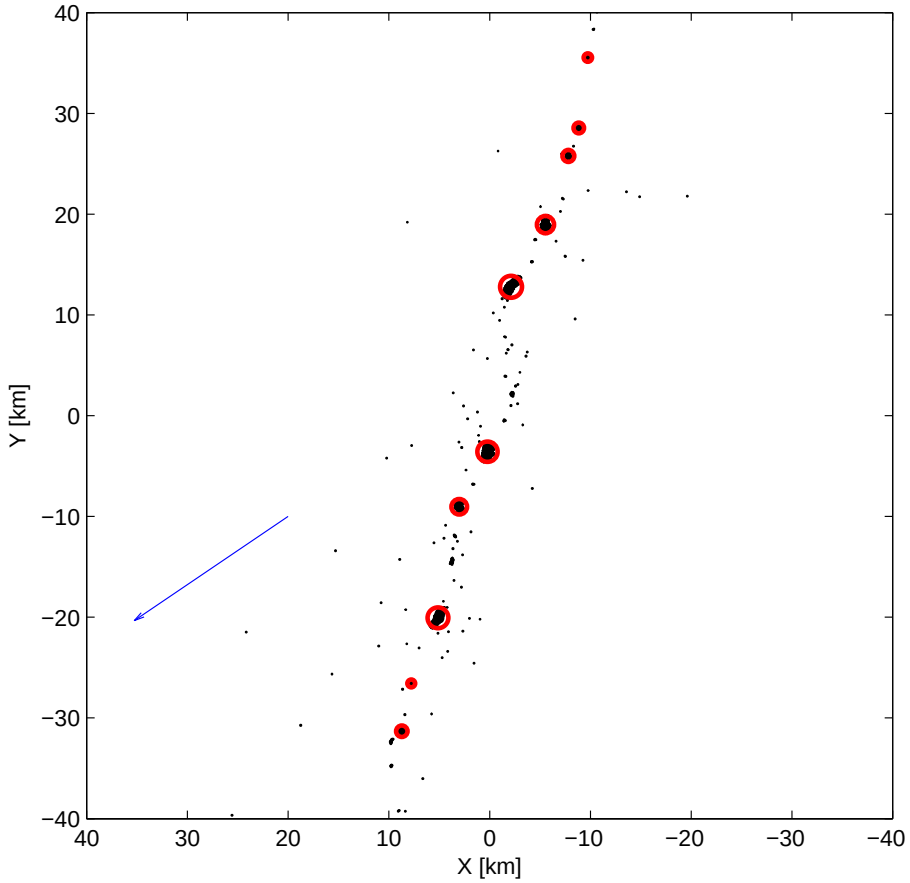

Figure 4.2: Tidal break-up of a simulated comet, shown a few hours after perijove. The projection on the plane of the orbit of each grain is marked by black dots. Thick circles mark some of the larger fragments, the largest of which contains about 19% of the original mass. The arrow points to the position of Jupiter, about 10^6 km away. This run was made with a bulk density $\rho = 300$ kg/m^3.

4.3 Results

4.3.1 Simulation parameters

The main quantity we are interested in constraining with these simulations is the bulk density of the progenitor SL9 comet. Several other physical parameters, however, are likely to influence a tidal encounter. The most important are discussed next.

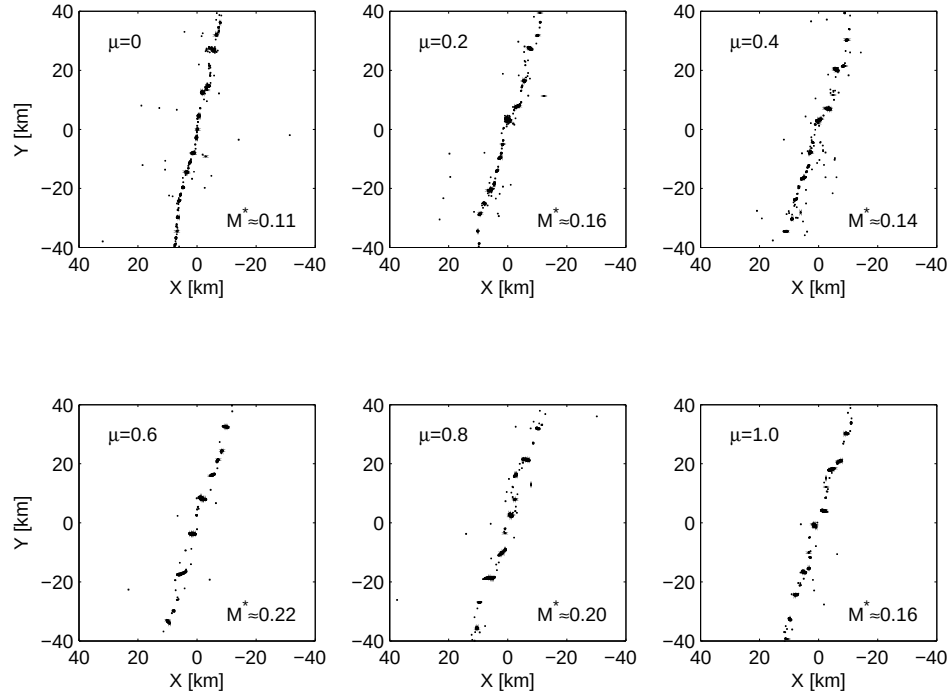

Figure 4.3: Projection to the plane of orbit of grains from tidally disrupted rubble piles. All runs followed the same orbit, and started as the same progenitor rubble pile, with a bulk density of $\rho = 300$ kg/m^3. The mass fraction contained in the largest clump is indicated by M^* (but note that our definition of "clump" is somewhat subjective). Friction is clearly a significant force, helping to delay breakup until tidal shear exceeds some critical value.

Friction coefficient

Although including *some* inter-granular friction in the simulation is crucial, and easily noticeable, our tests indicate that the exact value of the friction coefficient does not affect the outcome of a given tidal encounter very strongly (Fig. 4.3). This is fortunate, since the exact value of the friction coefficient between cometary material grains in vacuum is not well known. However, many measurements are obtained, especially in engineering applications of sea ice, concrete and other materials, where the effective coefficient of friction is of order $0.5 - 0.8$. We therefore use a friction coefficient of $\mu = 0.5$, typical of ices, rocks and other geological materials, in most of our runs, recognizing that it is possibly a lower limit, with only minor changes for increasing friction in the range of known values for common geologic materials.

Restitution coefficient

The restitution coefficient between cometary material grains in vacuum – that is, the ratio of the outgoing normal component of velocity, to the incoming normal component of velocity, corresponding to the height that a ball will bounce – is not known any better than the friction coefficient (see however *Durda et al.*, 2011; *Hartman*, 1978). Fortunately our numerical experiments indicate that the exact value of the restitution coefficient is likewise not a main concern (Fig.4.4), unless the value is extraordinarily high (perfectly elastic collisions) or extraordinarily low (perfectly inelastic, such as might be the case of extremely porous materials). The value of the restitution coefficient does play a role in the timing of the reaccumulaton, but does not affect the timing or extent of breakup, or the number of stable clumps after the encounter is over. Consistent with a number of experimental reports found in the literature (*Durda et al.*, 2011; *Imre et al.*, 2008) we use a value of $\varepsilon = 0.8$ for most of our runs. But as seen in the figure, even perfectly inelastic collisions are morphologically similar to the $\varepsilon = 0.8$ collisions. Thus, in summary, we find that using nominal values for μ and ε to be a justified approach in greatly reducing the parameter space.

Spin rate

There is no doubt that a rotating progenitor would exhibit a very different behavior, for a given orbit and density, than a non-rotating one. In fact, since the centrifugal acceleration would be added on top of all other forces, it is logical to expect that density and spin rate would be almost complementary. In other words, a range of disruption levels can be achieved either by adjusting density for a given spin rate, or by adjusting spin rate for a given density (*Asphaug and Benz*, 1996). Unfortunately, there is no information on SL9's rotation state prior to its breakup, other than statistical knowledge that Jupiter family comets have rotation periods ranging from ~ 6 hours to ~ 2 days, mostly in the slower range, regulated by their levels of activity. Furthermore there is no knowledge whether this is prograde rotation or retrograde rotation, or out of the plane. Thus, our results below apply only to a non-rotating comet. It is important to recognize that retrograde rotation can prevent the nucleus from disrupting tidally, forming a massive central clump that was not observed for SL9. Thus *Asphaug and Benz* (1996) considered only zero rotation or prograde rotation, finding that a fast-spinning prograde nucleus (period 9 h)

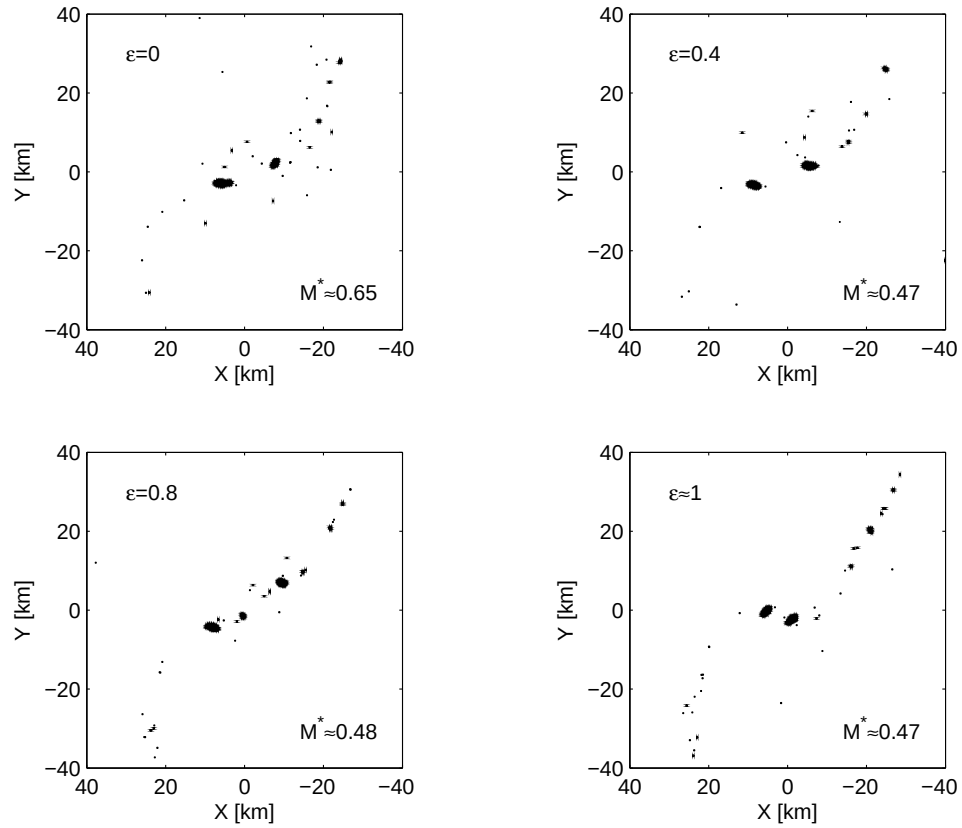

Figure 4.4: Same as Fig. 4.3 but with varying values of coefficient of restitution. Progenitor rubble piles had a bulk density of $\rho = 600$ kg/m^3. A larger coefficient of restitution speeds up the re-aggregation of clumps after tidal breakup, but by the time clumping is complete the final configuration is not sensitive to the exact value of ε.

would come apart similarly, even if it were $\sim 2/3$ the predicted diameter as a non-rotating nucleus, and $\sim 3/2$ the bulk density. We do not consider rotation in our present analysis, but anticipate similarly, that what we obtain below are lower limits to the bulk density, given the possibility (relatively minor) that SL9 could have been a prograde rapid rotator.

The effect of 'resolution'

In DEM models, the number of discrete, elementary particles is often considered the resolution of the model. This is appropriate in the sense that increasing this number as much as computation resources allow is desirable, and probably leads to more physical results, in the sense that asteroids and comets could be made of relatively fine materials. It is important, however,

to realize that this 'resolution' has a different meaning than what is usually ascribed to this parameter in numerical continuum models (such as hydrocodes). In a grid-based finite difference scheme, say, the goal is to approximate a continuous field by its value at a finite number of grid points, and the quality of the approximation can be rigorously related to the grid spacing – the resolution. A natural way to decide what is an appropriate resolution is to look for convergence of the predicted field value with successive halving of the grid spacing.

A DEM is not usually amenable to a rigorous error analysis. We do not have an upper bound to the expected error and no theoretical basis for selecting an appropriate resolution, unless – as in our laboratory experiment of 1400 12-sided dice falling to their angle of repose described above – we know it apriori. Unless we are modeling a very small system (or a small volume in a periodic system) we often must use a much smaller number of particles than exists in the physical system. In this work, for example, we use thousands of grains to model a rubble pile who must in reality contain billions of grains. And we have no theoretical estimate to guide us when trying to understand how good of an approximation we are making.

Worse, we cannot even expect that using more and more grains will make our simulations converge, in the usual sense. Figure (4.5) shows the result of a tidal encounter modeled at different resolutions. We do not see, and should not expect to see, a convergence in the positions of individual grains, or even of the largest clumps. Although we wish to model the same physical system (the comet) with increasingly better approximations, we are in fact modeling four quite different bodies. Indeed, to keep the mean density constant we must assign slightly different material densities to each of the rubble piles, as their bulk volume cannot be made exactly identical.

We can, however, expect a convergence of sorts with successive increase in resolution. We can expect that the general behavior of the ensemble of grains will not depend on the number of grains, in the sense that a pile of gravel pouring out of a dump truck, will behave similarly to a dump truck load full of sand, with similar total mass, grain size and shape and porosity, but with millions of times more grains. But a dump truck load of microfine powder will begin to behave differently, as will a dump truck containing four or five huge rocks. All we can expect, and require, is that any conclusions we draw from DEM simulations not depend too sensitively on the sizes of the elements. This is indeed the case with our SL9 tidal encounter simulations. The range of bulk densities we find necessary to match the appearance of post-periapse SL9

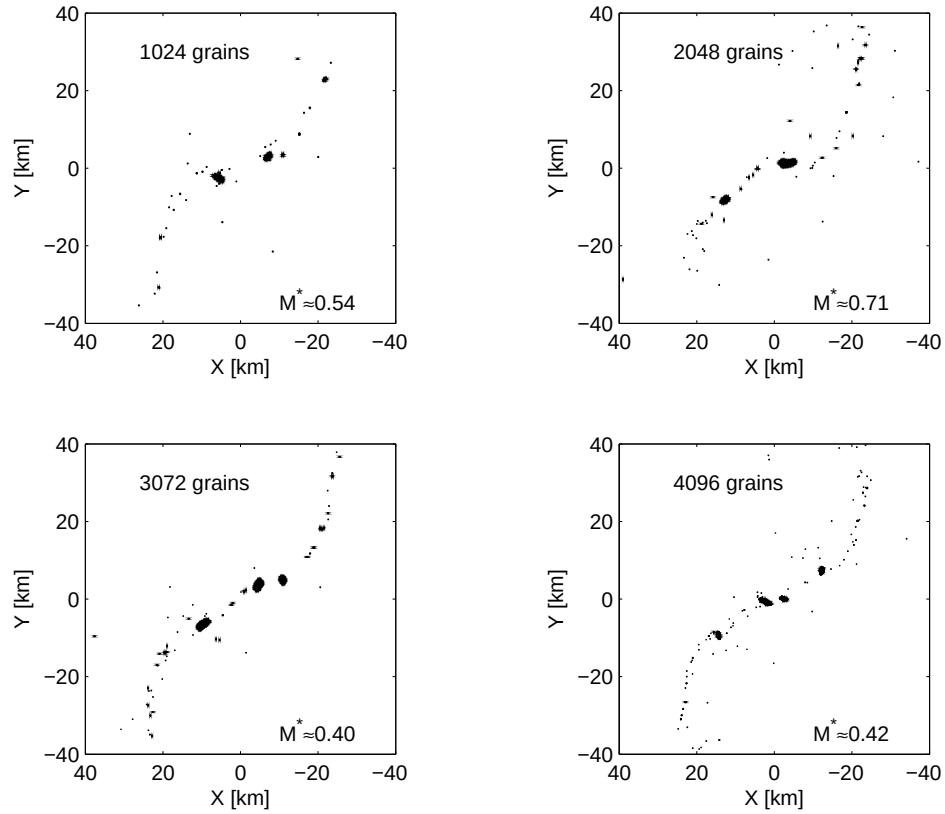

Figure 4.5: Same as Fig. 4.4 but with different number of grains in the progenitor rubble pile. The rubble piles had a bulk density of $\rho = 600$ kg/m^3. The general ensemble behavior is captured almost as well with 1024 grains as with 4096 grains. Whether or not either is a good approximation to an ensemble of billions of grains remains open.

remains the same when we run our simulations with 1024 grains as when we ran it with 4096 grains. In this sense we believe we have used adequate resolution, a belief that must be retested when computation resources allow.

Grain geometry

As mentioned above, all previous studies of SL9 using DEM techniques has been done with spherical elements. Our DEM is capable of implementing arbitrary shapes, so another dimension of the parameter space opens up – what shapes to use? It seems the logical answer is to use random, angular shapes, since there is no reason to think planetary rubble pile elements would have a special shape. However there is some expectation that fragments generated by past cratering and disruption events will have an average aspect ratio $2 : \sqrt{2} : 1$ (*Fujiwara et al.*,

1989). All our runs so far were made with 20 sided polyhedra, generated by a prescription that avoids sharp "knife-edges" and extreme aspect ratios but is otherwise random.

A related question is just how important is the use of non-spherical grains. This is an important question since computer codes that employ only spherical grains can typically run at much higher resolutions, making them perhaps the better choice. We find this choice to be quite important. We have compared runs with rubble piles composed of spherical grains (using the same PhysX engine) to runs with similar rubble piles (same shape, same bulk density) made out of random polyhedra. We find that the outcome of a simulated tidal disruption can be significantly different in the two cases (Fig. 4.6). Spherical grains appear to be adequate for very "dynamic" encounters, where the progenitor is quickly disrupted and the outcome is determined by the play of long range gravity forces between grains. But for gentler encounters, where friction and dilatation forces nearly balance the tidal stress (that is, the kinds of threshold breakups that probably dominate such events), the use of polyhedral grains can make enough of a difference to keep a rubble pile from disrupting at all.

In future work studying the more general aspects of rubble-pile disruption, we shall focus on the specifics of the aspect ratios of the polyhedra, as these are closely related to what we perceive to be the dominant factors that distinguish the present model from the previous sphere-based models of SL9, namely the physics of grain locking and shear dilatation.

4.3.2 Progenitor's bulk density

A tidal encounter between a cohesionless rubble pile and a planet is a tug-of-war game between the gravitational pull of the primary planet, and the self-gravity of the interloping body. The self gravity has three expressions, the most obvious being the long range force that holds particles together. But intergranular friction also scales with the local normal stress, and thus can be considered a result of self-gravity. The third expression is dilatation, the fact that irregular grains, while rotating locally in response to shear, most move other bodies aside, posisbly against the local normal stress. So again, dilatation can be considered an expression of self-gravity.

It is therefore ultimately the rubble pile's bulk density that will determine the outcome of the encounter (or more precisely, the ratio of the rubble pile's density to the density of the primary, to the 1/3 power), for a given structural configuration. Conversely, knowing that the outcome of SL9's encounter with Jupiter was a train of sizable fragments, we may use this to bracket the

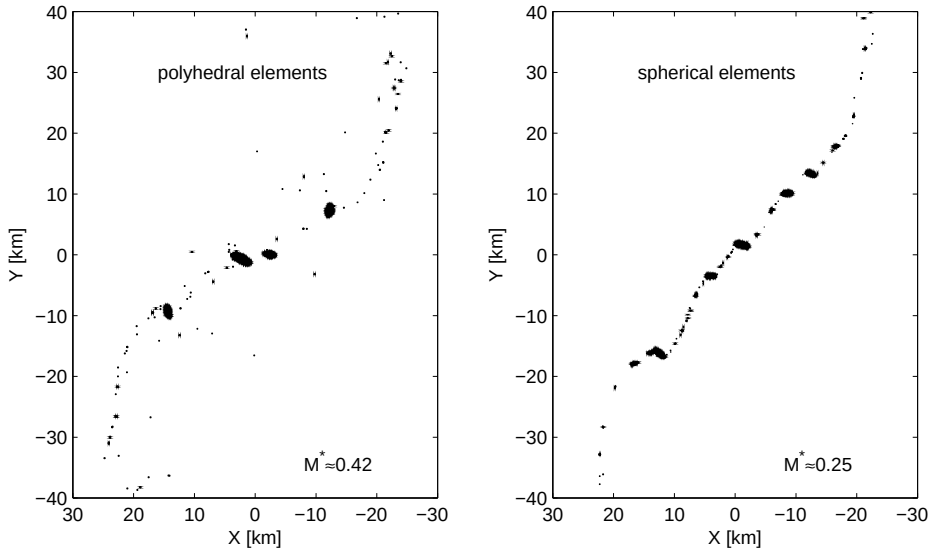

Figure 4.6: Following the same orbit, a rubble pile made of spherical grains behaves differently than a pile made of polyhedral grains. The onset of deformation occurs sooner with spherical grains, and the resulting fragment train contains a larger number of smaller mass fragments. This is probably due to the more pronounced friction and dilatation experienced by polyhedral grains.

possible density values of the progenitor rubble pile.

Using nominal values for the coefficients of friction and restitution, we ran simulated tidal encounters of a non-rotating, 1 km rubble pile of 4096 randomly shaped polyhedra, along SL9's 1992 nearly-parabolic orbit, varying the comet's bulk density from 100 to 600 kg m^{-3}. Figure 4.7 shows how varying the bulk density affects the outcome of the encounter. We can see that a density smaller than ~ 300 kg m^{-3}, or greater than ~ 400 kg m^{-3} would be inconsistent with the fragment train observed in the case of SL9, or expected from the appearance of linear crater chains on Ganymede.

4.4 Conclusions

The tidal disruption of comet Shoemaker-Levy 9 has been revisited using state of the art computational techniques for the behavior of rubble piles. The primary difference between these new models and what has been done in previous efforts (*Asphaug and Benz*, 1994, 1996; *Richardson et al.*, 1998) is the use of non-spherical, and thus presumably more realistic grain shapes, so that instead of 'marble piles' we have true rubble piles with grains that can lock and jam and pack

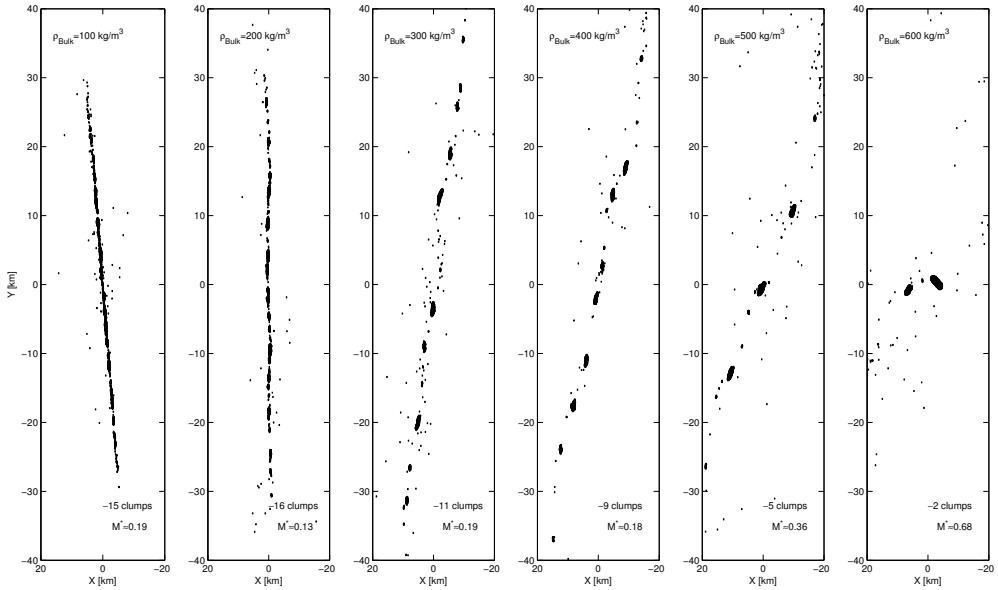

Figure 4.7: Positions of mass fragments, in the orbit plane, of a rubble-pile body following SL9's 1992 orbit, shown ~ 5 hours after perijove. For these runs a friction coefficient $\mu = 0.5$ and restitution coefficient $\varepsilon = 0.8$ were used. The lowest and highest bulk density values are wholly inconsistent with the appearance of the SL9 chain, thus providing a revised constraint on the density of this comet.

differently than spheres, and which must do work in order to achieve any amount of shear strain or even rotate in place. In this sense, dilatancy can be considered a force resisting tidal sheer, and this force may well have been underestimated when spherical grains were used to model a rubble pile, for in that case individual grains can respond to sheer by freely rotating in-place, unless measures are taken to explicitly constrain them.

While we include coefficients of friction and coefficients of restitution in our simulations, we find that varying these widely, but within reasonable values, does little to affect the final outcome of tidal disruption. These parameters do affect the timing of disruption and re-aggregation however. Increasing the coefficient of friction allows the progenitor body to better resist tidal sheer, and so the point of runaway deformation and disruption is postponed. Increasing the coefficient of restitution, the elasticity of individual grains, causes the re-aggregation phase to continue for a longer time, as grains bounce off of each other and may take hours to settle in stable clumps.

These observations, however, are unlikely to be the last word on the topic, because friction as implemented is a very simple force, acting when contact surfaces shear past one another

at the resolution scale of tens of meters. For much smaller-scale assemblages (piles of dust, perhaps) internal friction can be much greater. That said, the overall morphology of the clumps from Shoemaker-Levy 9 are self-gravitational in signature. This being one example, *Schenk et al.* (1996) looked to the much larger record of a dozen or more tidal disruption catenae imprinted on the satellites of Jupiter. Specifically they found no correlation between the number of clumps in a chain, versus the diameter of the progenitor forming the chain. In other words, the clumping process is scale invariant, suggesting self-gravitation rather than fragmentation, which does depend on scale, is the dominant process. As for coefficient of restitution, we find even less sensitivity to this parameter, with the range of outcomes being similar within the range of values that might be applicable.

A bulk density $\sim$ 300–400 kg m^{-3} is obtained for Shoemaker- Levy 9. This is in good agreement with the recent estimates of cometary bulk density from the Deep Impact mission (highly uncertain), estimated from the rate of fallback of crater ejecta (*Richardson et al.*, 2007), and from the dynamics of orbiting blocks that were imaged by the same spacecraft when it flew by Comet Hartley 2 (*A'Hearn et al.*, 2011); further constrained by the comet's dog-bone shape. (*A'Hearn et al.* found that $\rho = 220$ kg m^{-3} works best when fitting potential contours to the geometry of the waist.) This latter result advises caution in blindly adopting the physical realism of ours or any other forward model, because it shows that even our present treatment, however technically advanced, does not yet address such factors as shape and initial rotation.

That said, it is important to study these rare events because they are the only tests we shall have, at a cosmic-geological scale, of global scale catastrophic disruption of small bodies. It is the only way, pending spacecraft investigations that activate a comet nucleus globally (e.g. seismology) or that form mega-craters on small asteroids (precursors to hazard mitigation, or for science), that we are going to be able to learn how rubble piles behave, and evolve, and respond to energetic impulses and planetary encounters. By advancing the predictive capability of rubble-pile models, and benchmarking them against known small bodies data, we are making forward predictions more reliable.

Appendix A

Gravity dominated impact simulations with SPHERAL

SPHERAL++ is a Lagrangian, ASPH-based hydrocode coupled with an oct-tree gravitational code. The Adaptive SPH algorithm, originally developed for cosmological applications, is described in (*Owen*, 2010; *Owen et al.*, 1998).

For the gravity-regime collisions of interest in this work, we made some modifications to the original, cosmological code. These include:

1. Addition of an equation-of-state for ice and rock. We implemented the Tillotson EOS (*Melosh*, 1989; *Tillotson*, 1962). For water ice and for basalt we use the parameters suggested by *Benz and Asphaug* (1999, their Table II). Because the Tillotson EOS is fully analytical, it is very computationally efficient and easy to implement. It may not be as complete or as accurate as the latest tabulated equations-of-state (*Senft and Stewart*, 2008), however, given the mixed composition of our targets (they are surely neither pure ice not pure rock) and the fact that we are interested in an order-of-magnitude question only, we chose expediency over thermodynamical accuracy.

2. A gravity time step based on local accelerations instead of local densities. During and immediately following impact, the time steps in a simulation are limited by a sound speed criterion. In later stages, it is the gravity time scale that controls the time stepping. For

large scale structures, some fraction of

$$t_{\rm grav} = (G\rho)^{-1/2}, \tag{A.1}$$

where G is the gravitational constant and ρ is an average density, can be used. But when the structure contains high- and low-density regions, as in the case of a large sheet of ejected material, this criterion is not useful. We look instead at the local accelerations of each SPH node, and a time step that is some fraction of

$$t_{\rm acc} = \sqrt{L/a_{\rm max}}, \tag{A.2}$$

where L is a length scale of the system and $a_{\rm max}$ is the maximum instantaneous acceleration of any SPH node.

3. Initial condition generators for a target in hydrostatic equilibrium. The targets we are interested in here are in the 200–2000 km range. In the upper end of this size range, giving a target an initial constant density at the start of the simulation will result in local velocities that are due to the target collapsing or expanding under its own weight, and having nothing to do with the impact. To resolve this, it is important to start the target as close to hydrostatic equilibrium as possible. In our case, because the targets are only slightly compressed at equilibrium, we can use the first-order approximation:

$$p(r) = \frac{2\pi}{3} G\rho^2 (a^2 - r^2), \tag{A.3}$$

where p is the pressure at radial distance r from the center, ρ is the average density, and a is the satellite's radius. This pressure profile can then be inverted (numerically) using the chosen equation-of-state to yield a density profile that can be used for initial SPH node placement.

When setting initial positions of SPH nodes, it is also important to keep a constant distance between neighboring nodes. We have experimented with several methods of node placement, including (a) on a rectangular grid, (b) on spherical shells, (c) randomized placement with uniform spatial probability, and (d) an Hexagonal Close Packing arrangement. The

Hexagonal Close Packing arrangement, trimmed to a spherical shape by removing nodes outside a given radius, seems to work best. It guarantees equal distance between all 12 immediate neighbors of a node, and avoids the artificial singularities that result from a rectangular grid, especially if impactor is slightly translated or rotated with respect to the target. We have not noticed any artificial behavior that can be attributed to the geometry.

Our targets consist of 160,000 nodes (60 nodes across) and the number of nodes in the impactors is chosen to match the mass-per-node with the target as closely as possible. This results in $\sim$2000 nodes in a 250 km impactor. We simulate head-on collisions, so the impactor is set right next to the target with their centers almost aligned. (We set the impactor a few degrees above the target to break the artificial lattice symmetry.)

In SPHERAL the smoothing length h for each node is advanced based on measuring distortions in the local particle spacing via moments of the point distribution (*Owen*, 2010) and is not guaranteed contain a fixed number of neighbors. We thus need to limit the maximum smoothing length $h_{\max}$ to avoid a situation where escaping nodes expand their smoothing length to encompass the entire simulated space. Typically, $h_{\max}$ is a few times the initial separation between nodes. For consistency, we then need to set a lower bound on node density:

$$\rho_{\min} = m_{\text{node}}/h_{\max}^3. \tag{A.4}$$

Of the two standard ways to calculate density in SPH simulations, we usually employ the method of integrating the continuity equation.

Appendix B

Additional Monte-Carlo LHB runs

The scaling of Q_D^* used in most of the Monte-Carlo runs described in chapter 2 is a velocity-independent function of target size only, derived by fitting a power law to the combined results of SPH simulations from this work and those of *Benz and Asphaug* (1999) (see section 2.2 in the main text and appendix A for detail). In contrast, *Leinhardt and Stewart* (2012, hereafter LS12) derive a more complete scaling law that makes Q_D^* an increasing function of impact velocity. This scaling law implies that using a value of Q_D^* for a given target size from SPH simulations at a given velocity to predict the outcome of higher velocity impacts might overestimate the disruption.

To test this possibility we ran our baseline Monte-Carlo simulation using the LS12 disruption scaling. The procedure to determine the total mass remaining post collision, M_{lr}, is as follows.

Given the target mass and radius, R and M, the impactor mass and radius, r and m, the impact velocity v and the impact angle θ, we first calculate m' the mass in the volume of

impactor intercepting the target:

$$l = (R + r)(1 - \sin\theta), \tag{B.1}$$

$$\alpha = \begin{cases} \frac{3rl^2 - l^3}{4r^3}, & l < 2r, \\ 1, & \text{otherwise}, \end{cases} \tag{B.2}$$

$$m' = \alpha m. \tag{B.3}$$

Next we compare the impact velocity with $v'_{\rm esc}$ defined by

$$v'_{\rm esc} = \sqrt{2G(M + m')/(R + r)}. \tag{B.4}$$

If $v < v'_{\rm esc}$ the result is perfect merging and $M_{lr} = M + m$. Otherwise we calculate:

$$\rho_1 = 1000 \text{ kg/m}^3, \tag{B.5}$$

$$R_{c1} = \Big(\frac{3(M + m)}{4\pi\rho_1}\Big)^{1/3}, \tag{B.6}$$

$$Q^*_{RD,\gamma=1} = c^* \frac{4\pi}{5} \rho_1 G R^2_{c1}, \tag{B.7}$$

where $c^* = 1.9$ and G is the gravitational constant. We also need the reduced mass μ and reduced interacting mass μ':

$$\mu = \frac{Mm}{M + m}, \tag{B.8}$$

$$\mu' = \frac{Mm'}{M + m'}. \tag{B.9}$$

The disruption critical energy for head-on impacts is

$$Q^*_{RD} = Q^*_{RD,\gamma=1} \Big(\frac{1}{4}\frac{(\gamma + 1)^2}{\gamma}\Big)^{\frac{2}{3\bar{\mu}} - 1}, \tag{B.10}$$

with $\bar{\mu} = 0.35$, and the modified value for an oblique impact is

$$Q^{*\prime}_{RD} = Q^*_{RD} \Big(\frac{\mu}{\mu'}\Big)^{2 - \frac{3}{2}\bar{\mu}}. \tag{B.11}$$

With the disruption criterion we can calculate the impact velocity at the onset of erosion:

$$Q_e = 2Q'^{*}_{RD}(1 - M/(M+m)), \tag{B.12}$$

$$v_e = \sqrt{2Q_e(M+m)/\mu}. \tag{B.13}$$

If the collision is *grazing* (defined by $\sin\theta > (R/(R+r))$) and $v < v_e$ then the predicted result is a hit-and-run collision and $M_{lr} \approx M$. Otherwise, we compare the impact velocity with the critical velocity for *super-catastrophic* collisions, defined by $M_{lr} = 0.1M$:

$$Q_{sc} = 2Q'^{*}_{RD}(1 - 0.1M/(M+m)), \tag{B.14}$$

$$v_{sc} = \sqrt{2Q_{sc}(M+m)/\mu}. \tag{B.15}$$

If $v > v_{sc}$ then we use the power law

$$M_{lr} = (M+m)\frac{0.1}{1.8^{\eta}}\Big(\frac{Q_R}{Q'^{*}_{RD}}\Big)^{\eta}, \tag{B.16}$$

where $\eta = -1.5$ and $Q_R = \mu v^2/(2(M+m))$. Otherwise the collision is in the disruption regime and the linear relationship

$$M_{lr} = (M+m)\Big(1 - \frac{1}{2}\frac{Q_R}{Q'^{*}_{RD}}\Big) \tag{B.17}$$

holds.

Figure B.1 shows the fraction of Monte-Carlo runs that included at least one collision with energy greater than one, two, or three times Q'^{*}_{RD}. Comparing with figure 2.2 in the main text, we see that, as expected, using the velocity-dependent Q'^{*}_{RD} scaling of LS12 results in less severe destruction. We get many fewer catastrophic collisions for each target. However, the probability of getting at least *one* catastrophic disruption remains high. Our conclusions about the implications of the LHB for the mid-sized moons therefore hold, regardless of the scaling law used.

It is worth noting that while the LS12 velocity-dependent formalism is much more complete than the simple power law scaling (eq. (2.2) in the main text), it is not necessarily more accurate when extrapolated to larger targets. Indeed, the LS12 scaling law does a poor job matching our own SPH simulations. For example, LS12 predicts that a 200 km radius projectile hitting

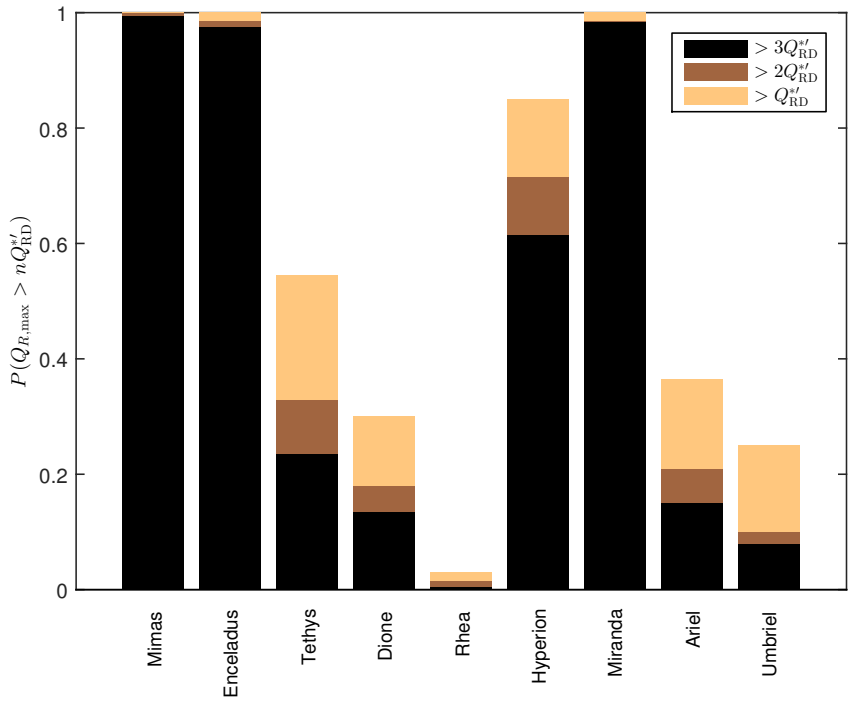

Figure B.1: Fraction P of Monte-Carlo runs that included at least one impact with effective specific energy greater than one, two, or three times the catastrophic disruption threshold $Q^{*\prime}_{RD}$, eq. (B.11). Compare with figure 2.2 in the main text.

a 1000 km radius target head-on would have to impact at about 40 km/s for a catastrophic disruption, while our simulations show the same level of destruction at only 13 km/s. So while we have no choice but to extrapolate to higher velocities, by using our modification to the *Benz and Asphaug* (1999) scaling we do not need to extrapolate to the target size.

Shortly after publication of the work reported in chapter 2 we used a suite of new SPH simulations to develop yet another scaling law for catastrophic disruption, different from both the Q^*_D power law and the more recent LS12 formalism. This new scaling is the subject of chapter 3. Figure B.2 shows the results of running the baseline Monte-Carlo simulation of chapter 2 using the newly derived scaling from chapter 3. As noted in sec. 3.5, using the new scaling leads to a lower threshold for catastrophic disruption, and this is evident when comparing figures B.2 and 2.2. Based on this comparison we conclude that our predictions made in chapter 2 are if anything too conservative. In other words, removing the danger of catastrophic disruption during an LHB for all mid sized moons would require even less cometary mass delivered to the

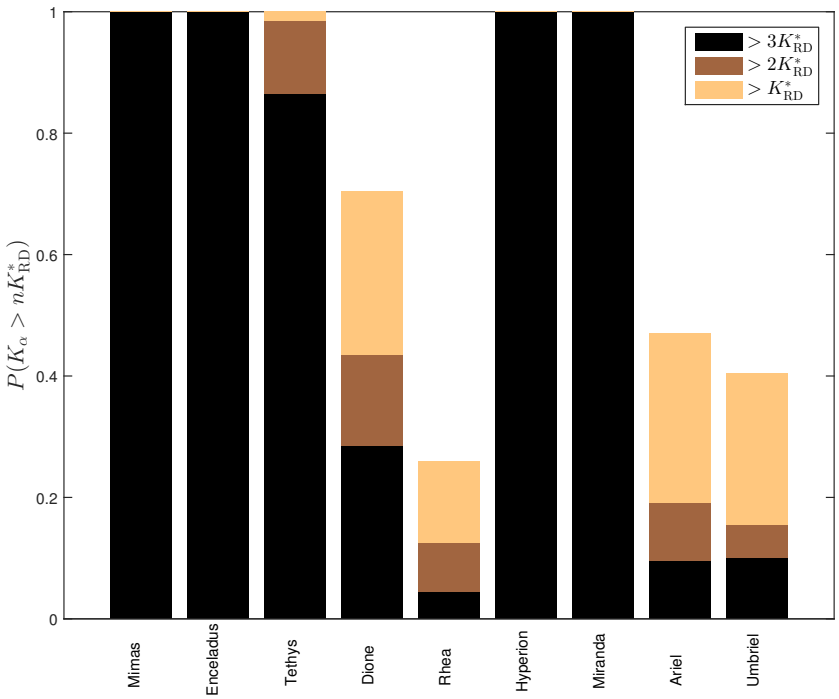

Figure B.2: Fraction P of Monte-Carlo runs that included at least one impact with effective specific energy greater than one, two, or three times the catastrophic disruption threshold using the scaling derived in chapter 3. Compare with fig. B.1 and fig. 2.2.

outer solar system than we had considered.

Appendix C

Practical implementation of the Iapetus Scaled Distribution

In principle, a normalized power law distribution is completely defined by its power index, α. A segmented power law is completely defined by several indices α_i and the corresponding break points r_i. In practice, fully implementing the distribution requires attention to some seemingly minor details that are easy to overlook. I record here the complete procedure for obtaining the size and mass distributions of cometary impactors in the outer Solar System, including the drawing of a pseudo-random sample from a uniform random number generator.

C.1 The Iapetus Scaled Distribution

Based on crater counts on Iapetus *Charnoz et al.* (2009) recommend the following differential distribution for the population of heliocentric comets presumably responsible, which they call the Iapetus Scaled Distribution (ISD):

$$\begin{cases} \frac{dN}{dr} & \propto r^{-2.5}, \quad 0 < r < r_1 = 7.5, \\ \frac{dN}{dr} & \propto r^{-3.5}, \quad r_1 < r < r_2 = 100, \\ \frac{dN}{dr} & \propto r^{-4.5}, \quad r_2 < r. \end{cases} \tag{C.1}$$

In the above equation r is the comet's radius in kilometers, and $N(r)$ is the cumulative fraction of comets with radius greater than r.

Equation (C.1) is not enough to uniquely define the distribution. We need to make one more assumption, which is that $N(r)$ is a power law too[1]. In general, for each branch in eq. (C.1), $N(r)$ can be of the form

$$N(r) = c_i r^{-\alpha_i} + b_i,$$

with c_i and b_i undetermined constants. Continuity and normalization will provide some constraints but not enough to completely fix N unless we require that N be a power law, i.e. that $b_i = 0$. With this choice we get

$$N(r) = \begin{cases} c_1 r^{-1.5}, & 0 < r < r_1, \\ c_2 r^{-2.5}, & r_1 < r < r_2, \\ c_3 r^{-3.5}, & r_2 < r, \end{cases} \tag{C.2}$$

and continuity at the break points[2] requires that $c_3 = r_2 c_2 = r_2 r_1 c_1$.

We have a problem with $\lim_{r\to 0} N(r) = \infty$. This power law cannot extend to arbitrarily small comets. We can't normalize the distribution until we choose a minimum comet size, $r_{\min}$, below which $N(r < r_{\min}) = 1$. We have to be careful with this choice though, because setting $r_{\min}$ too small will fill up our population (and computer memory) with tiny comets, while choosing a too large $r_{\min}$ means our population will be missing some mass. I return to this question later, when looking at the mass distribution. For now we keep $r_{\min}$ unspecified.

Knowing that $N(0 < r < r_{\min}) = 1$ and that $N(r)$ must be continuous at $r_{\min}$ we can finally write the complete normalized distribution:

$$N(r) = \begin{cases} 1, & r < r_{\min}, \\ r_{\min}^{1.5} r^{-1.5}, & r_{\min} < r < r_1, \\ r_1\, r_{\min}^{1.5} r^{-2.5}, & r_1 < r < r_2, \\ r_1 r_2\, r_{\min}^{1.5} r^{-3.5}, & r_2 < r. \end{cases} \tag{C.3}$$

[1] Or that the differential distribution is continuous, or that the proportionality in eq. (C.1) is the same for all branches.

[2] The *cumulative* distribution is always continuous, even if the *differential* distribution is not.

C.2 The mass distribution

To find the normalized differential mass distribution we need to use the *unnormalized* size distribution first:

$$\tilde{N}_c(r) = N_{\rm tot} N_c(r), \tag{C.4}$$

where $N_{\rm tot}$ is the total number of comets. I also use $N_c = 1 - N$ to make the integration slightly cleaner. The parameter $N_{\rm tot}$ is usually unknown. Luckily, we will see that $N_{\rm tot} r_{\rm min}^{1.5}$ can be simply related to the total mass in the distribution, $M_{\rm tot}$, in the limit $r_{\rm min} \to 0$. The mass $d\tilde{M}_c$ in the size bin rdr is

$$d\tilde{M}_c = \rho \frac{4\pi}{3} r^3 d\tilde{N}_c(r) = \rho \frac{4\pi}{3} N_{\rm tot} r^3 dN_c(r), \tag{C.5}$$

where ρ is a comet's bulk density in kilograms per cubic kilometer. The normalized differential mass is

$$dM_c = \frac{d\tilde{M}_c}{M_{\rm tot}} = \rho \frac{4\pi}{3} \frac{N_{\rm tot}}{M_{\rm tot}} r^3 dN_c(r). \tag{C.6}$$

Integrating, we find

$$M_c(R < r) = \int_0^r \frac{dM_c(r')}{dr'} dr' =$$
$$\rho \frac{4\pi}{3} \frac{N_{\rm tot} r_{\rm min}^{1.5}}{M_{\rm tot}} \begin{cases} 0, & r < r_{\rm min}, \\ r^{1.5} - r_{\rm min}^{1.5}, & r_{\rm min} < r < r_1, \\ r_1^{1.5} - r_{\rm min}^{1.5} + 5 r_1 r^{0.5} - 5 r_1^{1.5}, & r_1 < r < r_2, \\ r_1^{1.5} - r_{\rm min}^{1.5} + 5 r_1 r_2^{0.5} - 5 r_1^{1.5} - 7 r_1 r_2 r^{-0.5} + 7 r_1 r_2^{0.5}, & r_2 < r. \end{cases} \tag{C.7}$$

Now we can use the normalization requirement $M(\infty) = 1$ to eliminate $N_{\rm tot} r_{\rm min}^{1.5}$. If we denote

$$\eta^{-1} = -4 r_1^{1.5} + 12 r_1 r_2^{0.5} - r_{\rm min}^{1.5}, \tag{C.8}$$

we can write the complete normalized mass distribution:

$$M_c(r) = \eta \begin{cases} 0, & r < r_{\min}, \\ r^{1.5} - r_{\min}^{1.5}, & r_{\min} < r < r_1, \\ -4r_1^{1.5} - r_{\min}^{1.5} + 5r_1 r^{0.5}, & r_1 < r < r_2, \\ -4r_1^{1.5} - r_{\min}^{1.5} + 12r_1 r_2^{0.5} - 7r_1 r_2 r^{-0.5}, & r_2 < r, \end{cases} \tag{C.9}$$

and the unnormalized distribution in terms of M_{tot}:

$$\tilde{M}_c = M_{\text{tot}} M_c.$$

For the ISD $\eta^{-1} \approx 818 - r_{\min}^{1.5}$.

Now we can finally take the limit $r_{\min} \to 0$. We couldn't do this before, because we know that, for a given total mass, as $r_{\min}$ goes to zero N_{tot} increases without limit. But now we know that $N_{\text{tot}} r_{\min}^{1.5}$ does have a limit:

$$\lim_{r_{\min} \to 0} \rho \frac{4\pi}{3} \frac{N_{\text{tot}} r_{\min}^{1.5}}{M_{\text{tot}}} = 12 r_1 r_2^{0.5} - 4 r_1^{1.5},$$

or $\sim$0.0012 for the ISD.

We were able to normalize the mass distribution without any reference to $r_{\min}$. We can see that in the ISD only about 0.1% of the mass resides in comets smaller than 1 km, and only about 3% of the mass resides in comets smaller than 10 km. This gives us some confidence in choosing a reasonably large $r_{\min}$ to make the number distribution practical to work with.

C.3 Generating a pseudo-random ISD sample

Consider the cumulative distribution function (CDF):

$$F(r) = 1 - N(r) = \begin{cases} 0, & r < r_{\min}, \\ 1 - r_{\min}^{1.5} r^{-1.5}, & r_{\min} < r < r_1, \\ 1 - r_1\, r_{\min}^{1.5} r^{-2.5}, & r_1 < r < r_2, \\ 1 - r_1 r_2\, r_{\min}^{1.5} r^{-3.5}, & r_2 < r. \end{cases} \tag{C.10}$$

If X is a random variable with a uniform distribution on $[0, 1]$ then

$$R = F^{-1}(X) \tag{C.11}$$

is a random variable with the CDF $F(r)$. To see this is true, evaluate the probability $P(R < r)$:

$$P(R < r) = P\big(F^{-1}(X) < F^{-1}(x)\big) = P(X < x) = x = F(r), \tag{C.12}$$

where the last couple of steps are valid because F is monotonic and X is uniform. So, to draw a random radius, in kilometers, from the ISD, we can draw a uniform random x from $[0, 1]$ with a pseudo-random number generator and then compute

$$r = \begin{cases} r_{\min}, & x = 0, \\ \left(\frac{(1-x)}{r_{\min}^{1.5}}\right)^{-1/1.5}, & 0 < x < 1 - r_{\min}^{1.5} r_1^{-1.5}, \\ \left(\frac{(1-x)}{r_1 r_{\min}^{1.5}}\right)^{-1/2.5}, & 1 - r_{\min}^{1.5} r_1^{-1.5} < x < 1 - r_1 r_{\min}^{1.5} r_2^{-2.5}, \\ \left(\frac{(1-x)}{r_1 r_2 r_{\min}^{1.5}}\right)^{-1/3.5}, & 1 - r_1 r_{\min}^{1.5} r_2^{-2.5} < x. \end{cases} \tag{C.13}$$

Figure C.1 shows an empirical CDF of a pseudo-random sample of 10^7 radii drawn using this method. Compare with fig. (2) in *Charnoz et al.* (2009).

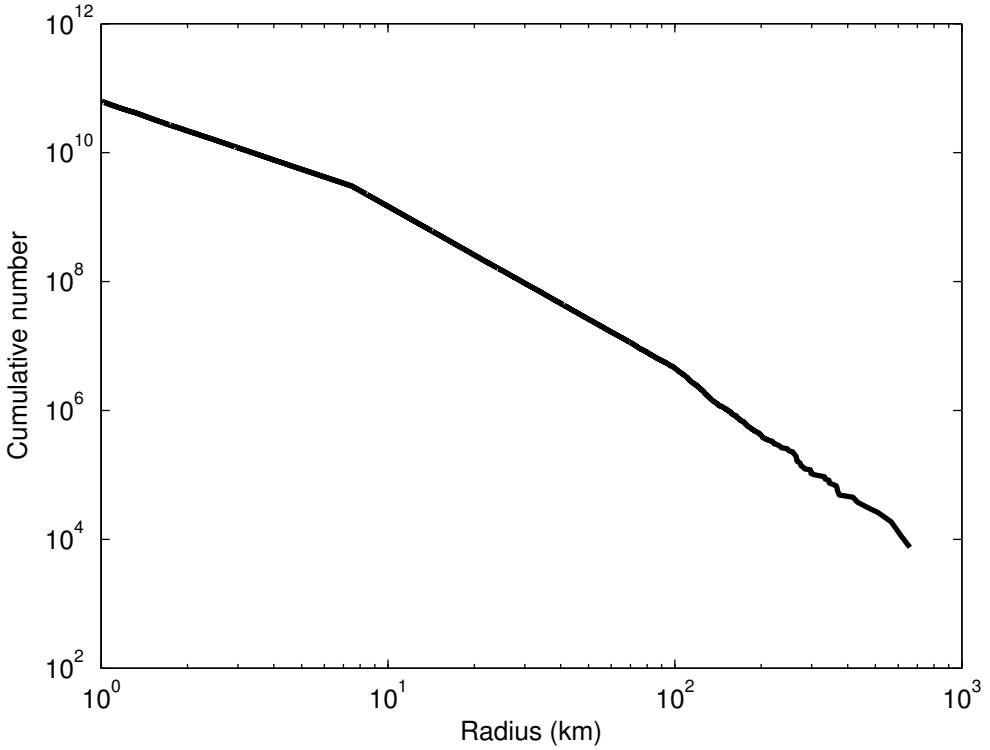

Figure C.1: Cumulative number of comets with radii greater than a given value, summed from a pseudo-random sample of the distribution (C.10) with $r_{\min} = 1$ and scaled to give 800 Pluto sized bodies.

C.4 Summary

Here are the relevant equations with the values recommended in *Charnoz et al.* (2009) for α_i and r_i and with $r_{\min} = 1$ km.

- Fraction of bodies with radius greater than r (in kilometers):

$$N(r) = \begin{cases} 1, & 0 < r < 1, \\ r^{-1.5}, & 1 < r < 7.5, \\ 7.5\, r^{-2.5}, & 7.5 < r < 100, \\ 750\, r^{-3.5}, & 100 < r. \end{cases}$$

- The fraction of total mass in bodies with radius less than r (in kilometers):

$$M_c(r) \approx \frac{1}{818} \begin{cases} r^{1.5}, & 0 < r < 7.5, \\ -82 + 37.5\, r^{0.5}, & 7.5 < r < 100, \\ 818 - 5250\, r^{-0.5}, & 100 < r. \end{cases}$$

- To draw a random radius, first draw a uniform $0 \leq x \leq 1$, and then evaluate:

$$r = \begin{cases} 1, & x = 0, \\ (1-x)^{-2/3}, & 0 < x < 0.951314, \\ 2.238847(1-x)^{-2/5}, & 0.951314 < x < 0.999925, \\ 6.628970(1-x)^{-2/7}, & 0.999925 < x. \end{cases}$$

Appendix D

Summary of all hydrcocode simulation results used to derive the scaling law of chapter 3

Table D.1: Summary of all impact simulation parametrs and results

EOS	R_T (km)	M_T (kg)	r_p (km)	m_p (kg)	θ (deg)	v (m/s)	$f_{\mathrm{LB}}{}^1$	$f_{\mathrm{LB}}{}^2$	grazing
ice	1000	3.793×10^{21}	794	1.92×10^{21}	0	2170	0.499	0.531	N
ice	1000	3.793×10^{21}	794	1.92×10^{21}	0	2225	0.462	0.496	N
ice	1000	1.128×10^{22}	794	5.68×10^{21}	0	2500	0.824	0.829	N
ice	1000	1.128×10^{22}	794	5.68×10^{21}	0	3500	0.506	0.531	N
ice	1000	1.128×10^{22}	794	5.68×10^{21}	0	3560	0.484	0.510	N
ice	1000	3.793×10^{21}	794	1.92×10^{21}	45	5235	0.428	0.425	Y
ice	1000	3.793×10^{21}	794	1.92×10^{21}	45	6000	0.343	0.343	Y
ice	1000	1.128×10^{22}	794	5.68×10^{21}	45	7300	0.494	0.492	Y
ice	1000	1.128×10^{22}	794	5.68×10^{21}	45	7400	0.489	0.488	Y
ice	1000	1.128×10^{22}	794	5.68×10^{21}	45	7520	0.482	0.481	Y
ice	1000	1.128×10^{22}	794	5.68×10^{21}	45	7800	0.465	0.463	Y

Table D.1: Summary of all impact simulation results (Continued)

EOS	R_T (km)	M_T (kg)	r_p (km)	m_p (kg)	θ (deg)	v (m/s)	$f_{\mathrm{LB}}{}^1$	$f_{\mathrm{LB}}{}^2$	grazing
ice	1000	1.128×10^{22}	794	5.68×10^{21}	45	8200	0.442	0.442	Y
ice	1000	1.128×10^{22}	794	5.68×10^{21}	45	9000	0.393	0.393	Y
ice	1000	1.128×10^{22}	794	5.68×10^{21}	45	10000	0.333	0.333	Y
ice	1000	3.793×10^{21}	794	1.92×10^{21}	55	6800	0.558	0.556	Y
ice	1000	3.793×10^{21}	500	4.65×10^{20}	0	3200	0.604	0.609	N
ice	1000	3.793×10^{21}	500	4.65×10^{20}	0	3330	0.514	0.514	N
ice	1000	3.793×10^{21}	500	4.65×10^{20}	0	3380	0.520	0.542	N
ice	1000	3.793×10^{21}	500	4.65×10^{20}	0	3440	0.489	0.516	N
ice	1000	3.793×10^{21}	500	4.65×10^{20}	0	3480	0.469	0.496	N
ice	1000	3.793×10^{21}	500	4.65×10^{20}	0	3610	0.409	0.425	N
ice	1000	1.128×10^{22}	500	1.37×10^{21}	0	4500	0.697	0.702	N
ice	1000	1.128×10^{22}	500	1.37×10^{21}	0	5000	0.566	0.588	N
ice	1000	1.128×10^{22}	500	1.37×10^{21}	0	5300	0.471	0.502	N
ice	1000	1.128×10^{22}	500	1.37×10^{21}	0	5500	0.393	0.434	N
ice	1000	3.793×10^{21}	500	4.65×10^{20}	30	4750	0.561	0.552	N
ice	1000	3.793×10^{21}	500	4.65×10^{20}	30	4900	0.517	0.509	N
ice	1000	3.793×10^{21}	500	4.65×10^{20}	30	4950	0.504	0.498	N
ice	1000	1.128×10^{22}	500	1.37×10^{21}	30	7990	0.504	0.501	N
ice	1000	1.128×10^{22}	500	1.37×10^{21}	30	8300	0.463	0.459	N
ice	1000	1.128×10^{22}	500	1.37×10^{21}	30	10000	0.268	0.281	N
ice	1000	3.793×10^{21}	500	4.65×10^{20}	45	9175	0.542	0.542	N
ice	1000	3.793×10^{21}	500	4.65×10^{20}	45	9400	0.525	0.524	N
ice	1000	3.793×10^{21}	500	4.65×10^{20}	45	9600	0.510	0.508	N
ice	1000	1.128×10^{22}	500	1.37×10^{21}	45	12000	0.674	0.676	N
ice	1000	1.128×10^{22}	500	1.37×10^{21}	45	13500	0.609	0.610	N
ice	1000	1.128×10^{22}	500	1.37×10^{21}	45	14800	0.542	0.544	N
ice	1000	1.128×10^{22}	500	1.37×10^{21}	45	15400	0.510	0.513	N

Table D.1: Summary of all impact simulation results (Continued)

EOS	R_T (km)	M_T (kg)	r_p (km)	m_p (kg)	θ (deg)	v (m/s)	$f_{\mathrm{LB}}{}^1$	$f_{\mathrm{LB}}{}^2$	grazing
ice	1000	1.128×10^{22}	500	1.37×10^{21}	45	15500	0.505	0.508	N
ice	1000	3.793×10^{21}	300	9.81×10^{19}	0	5000	0.853	0.840	N
ice	1000	3.793×10^{21}	300	9.81×10^{19}	0	6000	0.699	0.703	N
ice	1000	3.793×10^{21}	300	9.81×10^{19}	0	6500	0.590	0.608	N
ice	1000	3.793×10^{21}	300	9.81×10^{19}	0	6750	0.507	0.538	N
ice	1000	3.793×10^{21}	300	9.81×10^{19}	0	6800	0.487	0.519	N
ice	1000	3.793×10^{21}	300	9.81×10^{19}	0	7000	0.410	0.445	N
ice	1000	3.793×10^{21}	300	9.81×10^{19}	0	8000	0.077	0.103	N
ice	1000	1.128×10^{22}	300	2.89×10^{20}	0	11000	0.568	0.589	N
ice	1000	1.128×10^{22}	300	2.89×10^{20}	0	11400	0.514	0.537	N
ice	1000	1.128×10^{22}	300	2.89×10^{20}	0	11600	0.486	0.511	N
ice	1000	1.128×10^{22}	300	2.89×10^{20}	0	11900	0.445	0.469	N
ice	1000	1.128×10^{22}	300	2.89×10^{20}	0	14000	0.194	0.213	N
ice	1000	1.128×10^{22}	300	2.89×10^{20}	30	17380	0.498	0.504	N
ice	1000	1.128×10^{22}	300	2.89×10^{20}	30	18000	0.462	0.466	N
ice	1000	1.128×10^{22}	300	2.89×10^{20}	45	25000	0.613	0.617	N
ice	1000	1.128×10^{22}	300	2.89×10^{20}	45	26000	0.578	0.582	N
ice	1000	1.128×10^{22}	300	2.89×10^{20}	45	28000	0.508	0.500	N
ice	1000	3.795×10^{21}	200	2.91×10^{19}	0	13560	0.564	0.556	N
ice	1000	1.128×10^{22}	200	7.93×10^{19}	0	20000	0.762	0.767	N
ice	1000	1.128×10^{22}	200	7.93×10^{19}	0	26000	0.532	0.538	N
ice	1000	1.128×10^{22}	200	7.93×10^{19}	0	26800	0.500	0.498	N
ice	1000	1.128×10^{22}	200	7.93×10^{19}	30	34000	0.505	0.500	N
ice	1000	1.128×10^{22}	200	7.93×10^{19}	30	35000	0.475	0.463	N
ice	1000	1.128×10^{22}	200	7.93×10^{19}	45	48000	0.512	0.503	N
ice	1000	1.128×10^{22}	200	7.93×10^{19}	45	48200	0.507	0.498	N
ice	1000	1.128×10^{22}	200	7.93×10^{19}	45	50000	0.467	0.452	N

Table D.1: Summary of all impact simulation results (Continued)

EOS	R_T (km)	M_T (kg)	r_p (km)	m_p (kg)	θ (deg)	v (m/s)	$f_{\mathrm{LB}}{}^1$	$f_{\mathrm{LB}}{}^2$	grazing
ice	1000	1.128×10^{22}	200	7.93×10^{19}	45	55000	0.360	0.348	N
ice	500	4.724×10^{20}	500	4.68×10^{20}	0	1170	0.506	0.537	N
ice	500	4.724×10^{20}	500	4.68×10^{20}	0	1190	0.481	0.514	N
ice	500	1.395×10^{21}	500	1.38×10^{21}	0	1500	0.753	0.766	N
ice	500	1.395×10^{21}	500	1.38×10^{21}	0	1850	0.513	0.543	N
ice	500	1.395×10^{21}	500	1.38×10^{21}	0	1900	0.478	0.508	N
ice	500	1.395×10^{21}	500	1.38×10^{21}	0	2100	0.335	0.376	N
ice	500	1.395×10^{21}	500	1.38×10^{21}	45	1400	0.475	0.474	Y
ice	500	1.395×10^{21}	500	1.38×10^{21}	45	1600	0.462	0.460	Y
ice	500	1.395×10^{21}	500	1.38×10^{21}	45	1800	0.450	0.448	Y
ice	500	1.395×10^{21}	500	1.38×10^{21}	45	2000	0.439	0.437	Y
ice	500	1.395×10^{21}	500	1.38×10^{21}	45	2220	0.424	0.422	Y
ice	500	1.395×10^{21}	500	1.38×10^{21}	45	2450	0.410	0.407	Y
ice	500	1.395×10^{21}	500	1.38×10^{21}	45	2700	0.393	0.391	Y
ice	500	1.395×10^{21}	500	1.38×10^{21}	45	3000	0.374	0.373	Y
ice	500	4.724×10^{20}	250	5.81×10^{19}	0	1740	0.659	0.658	N
ice	500	4.724×10^{20}	250	5.81×10^{19}	0	1960	0.421	0.421	N
ice	500	4.724×10^{20}	250	5.81×10^{19}	0	2000	0.482	0.502	N
ice	500	4.724×10^{20}	250	5.81×10^{19}	0	2050	0.448	0.469	N
ice	500	4.724×10^{20}	250	5.81×10^{19}	0	2117	0.412	0.423	N
ice	500	1.395×10^{21}	250	1.71×10^{20}	0	2800	0.598	0.606	N
ice	500	1.395×10^{21}	250	1.71×10^{20}	0	3000	0.518	0.537	N
ice	500	1.395×10^{21}	250	1.71×10^{20}	0	3040	0.498	0.521	N
ice	500	1.395×10^{21}	250	1.71×10^{20}	0	3100	0.467	0.492	N
ice	500	1.395×10^{21}	250	1.71×10^{20}	30	4300	0.554	0.547	N
ice	500	1.395×10^{21}	250	1.71×10^{20}	30	4470	0.506	0.501	N
ice	500	1.395×10^{21}	250	1.71×10^{20}	30	4530	0.489	0.483	N

Table D.1: Summary of all impact simulation results (Continued)

EOS	R_T (km)	M_T (kg)	r_p (km)	m_p (kg)	θ (deg)	v (m/s)	$f_{\mathrm{LB}}{}^1$	$f_{\mathrm{LB}}{}^2$	grazing
ice	500	1.395×10^{21}	250	1.71×10^{20}	30	5000	0.321	0.329	N
ice	500	4.713×10^{20}	250	5.80×10^{19}	45	2000	0.835	0.834	N
ice	500	4.724×10^{20}	250	5.81×10^{19}	45	3400	0.733	0.733	N
ice	500	4.724×10^{20}	250	5.81×10^{19}	45	4650	0.577	0.577	N
ice	500	4.724×10^{20}	250	5.81×10^{19}	45	5053	0.457	0.460	N
ice	500	4.724×10^{20}	250	5.81×10^{19}	45	5100	0.503	0.506	N
ice	500	1.395×10^{21}	250	1.71×10^{20}	45	8000	0.494	0.498	N
ice	500	1.395×10^{21}	250	1.71×10^{20}	45	8100	0.482	0.488	N
ice	500	1.395×10^{21}	250	1.71×10^{20}	45	9000	0.380	0.387	N
ice	500	4.724×10^{20}	250	5.81×10^{19}	60	6000	0.792	0.792	Y
ice	500	4.724×10^{20}	250	5.81×10^{19}	60	9305	0.703	0.703	Y
ice	500	4.724×10^{20}	250	5.81×10^{19}	60	12070	0.556	0.558	Y
ice	500	4.724×10^{20}	250	5.81×10^{19}	60	12900	0.503	0.508	Y
ice	500	4.713×10^{20}	250	5.80×10^{19}	75	3000	0.888	0.888	Y
ice	500	4.724×10^{20}	250	5.81×10^{19}	75	6200	0.878	0.878	Y
ice	500	4.724×10^{20}	250	5.81×10^{19}	75	12000	0.862	0.862	Y
ice	500	4.724×10^{20}	100	3.36×10^{18}	0	5200	0.886	0.884	N
ice	500	4.724×10^{20}	100	3.36×10^{18}	0	7000	0.704	0.709	N
ice	500	4.724×10^{20}	100	3.36×10^{18}	0	7300	0.654	0.664	N
ice	500	4.724×10^{20}	100	3.36×10^{18}	0	8000	0.495	0.520	N
ice	500	4.724×10^{20}	100	3.36×10^{18}	0	8200	0.439	0.468	N
ice	500	4.724×10^{20}	100	3.36×10^{18}	0	9100	0.213	0.252	N
ice	500	4.724×10^{20}	100	3.36×10^{18}	0	10000	0.104	0.114	N
ice	500	1.395×10^{21}	100	9.91×10^{18}	0	12000	0.678	0.687	N
ice	500	1.395×10^{21}	100	9.91×10^{18}	0	13500	0.552	0.567	N
ice	500	1.395×10^{21}	100	9.91×10^{18}	0	14100	0.495	0.509	N
ice	500	1.395×10^{21}	100	9.91×10^{18}	0	15000	0.411	0.423	N

Table D.1: Summary of all impact simulation results (Continued)

EOS	R_T (km)	M_T (kg)	r_p (km)	m_p (kg)	θ (deg)	v (m/s)	$f_{\mathrm{LB}}{}^1$	$f_{\mathrm{LB}}{}^2$	grazing
ice	500	1.395×10^{21}	100	9.91×10^{18}	30	17840	0.501	0.515	N
ice	500	1.395×10^{21}	100	9.91×10^{18}	30	18000	0.490	0.503	N
ice	500	1.395×10^{21}	100	9.91×10^{18}	30	20000	0.369	0.375	N
ice	500	1.395×10^{21}	100	9.91×10^{18}	45	25000	0.495	0.506	N
ice	500	1.395×10^{21}	100	9.91×10^{18}	45	28000	0.362	0.357	N
ice	300	1.020×10^{20}	150	1.25×10^{19}	0	1000	0.793	0.789	N
ice	300	1.020×10^{20}	150	1.25×10^{19}	0	1200	0.627	0.630	N
ice	300	1.020×10^{20}	150	1.25×10^{19}	0	1290	0.530	0.543	N
ice	300	1.020×10^{20}	150	1.25×10^{19}	0	1390	0.417	0.440	N
ice	300	1.020×10^{20}	150	1.25×10^{19}	0	1800	0.036	0.051	N
ice	300	3.005×10^{20}	150	3.69×10^{19}	0	1950	0.534	0.548	N
ice	300	3.005×10^{20}	150	3.69×10^{19}	0	2015	0.491	0.511	N
ice	300	3.005×10^{20}	150	3.69×10^{19}	0	2030	0.482	0.501	N
ice	300	3.005×10^{20}	150	3.69×10^{19}	0	2300	0.296	0.331	N
ice	300	3.005×10^{20}	150	3.69×10^{19}	30	3000	0.533	0.530	N
ice	300	3.005×10^{20}	150	3.69×10^{19}	30	3100	0.500	0.500	N
ice	300	3.005×10^{20}	150	3.69×10^{19}	45	4200	0.674	0.672	N
ice	300	3.005×10^{20}	150	3.69×10^{19}	45	5110	0.503	0.508	N
ice	300	3.005×10^{20}	150	3.69×10^{19}	45	5200	0.480	0.485	N
ice	300	3.005×10^{20}	60	2.14×10^{18}	0	3200	0.970	0.970	N
ice	300	1.020×10^{20}	60	7.27×10^{17}	0	4945	0.697	0.700	N
ice	300	1.020×10^{20}	60	7.27×10^{17}	0	5500	0.545	0.567	N
ice	300	1.020×10^{20}	60	7.27×10^{17}	0	5600	0.507	0.529	N
ice	300	1.020×10^{20}	60	7.27×10^{17}	0	5770	0.424	0.459	N
ice	300	1.020×10^{20}	60	7.27×10^{17}	0	6320	0.180	0.188	N
ice	300	3.005×10^{20}	60	2.14×10^{18}	0	8100	0.629	0.642	N
ice	300	3.005×10^{20}	60	2.14×10^{18}	0	8600	0.549	0.566	N

Table D.1: Summary of all impact simulation results (Continued)

EOS	R_T (km)	M_T (kg)	r_p (km)	m_p (kg)	θ (deg)	v (m/s)	$f_{\mathrm{LB}}{}^1$	$f_{\mathrm{LB}}{}^2$	grazing
ice	300	3.005×10^{20}	60	2.14×10^{18}	0	8800	0.512	0.531	N
ice	300	3.005×10^{20}	60	2.14×10^{18}	0	8900	0.493	0.512	N
ice	300	3.005×10^{20}	60	2.14×10^{18}	0	8980	0.477	0.500	N
ice	300	3.005×10^{20}	60	2.14×10^{18}	0	9040	0.463	0.483	N
ice	300	3.005×10^{20}	60	2.14×10^{18}	0	9500	0.378	0.406	N
ice	300	3.005×10^{20}	60	2.14×10^{18}	30	11450	0.508	0.523	N
ice	300	3.005×10^{20}	60	2.14×10^{18}	30	11630	0.488	0.503	N
ice	300	3.005×10^{20}	60	2.14×10^{18}	30	12000	0.441	0.459	N
ice	300	3.005×10^{20}	60	2.14×10^{18}	45	16000	0.519	0.533	N
ice	300	3.005×10^{20}	60	2.14×10^{18}	45	16250	0.495	0.511	N
ice	300	3.005×10^{20}	60	2.14×10^{18}	45	16400	0.481	0.497	N
ice	300	3.005×10^{20}	60	2.14×10^{18}	45	17000	0.431	0.448	N
ice	100	3.775×10^{18}	50	4.64×10^{17}	0	590	0.496	0.508	N
ice	100	1.112×10^{19}	50	1.37×10^{18}	0	800	0.603	0.606	N
ice	100	3.775×10^{18}	50	4.64×10^{17}	0	830	0.019	0.027	N
ice	100	1.112×10^{19}	50	1.37×10^{18}	0	860	0.502	0.516	N
ice	100	1.112×10^{19}	50	1.37×10^{18}	30	1100	0.632	0.629	N
ice	100	1.112×10^{19}	50	1.37×10^{18}	30	1280	0.544	0.541	N
ice	100	1.112×10^{19}	50	1.37×10^{18}	30	1340	0.513	0.511	N
ice	100	1.112×10^{19}	50	1.37×10^{18}	30	1355	0.505	0.503	N
ice	100	1.112×10^{19}	50	1.37×10^{18}	45	2000	0.633	0.630	N
ice	100	1.112×10^{19}	50	1.37×10^{18}	45	2370	0.502	0.502	N
ice	100	1.112×10^{19}	50	1.37×10^{18}	45	2400	0.489	0.490	N

[1] Gravitationally bound mass fraction as detected by the bottom-up algorithm of sec. 3.2.4.

[2] Gravitationally bound mass fraction as detected by the top-down algorithm of sec. 3.2.4.

Appendix E

Derivation of interacting mass and energy

Consider the collision geometry illustrated in figure E.1. We are interested in the fraction of projectile mass between the two horizontal lines tangent to the bottom of the projectile and the top of the target. The hemispheric cap above height l from the bottom of the projectile is assumed to not interact with the target and its kinetic energy is not available for disruption. The height l is given by

$$l = r_p + [R_T - (R_T + r_p)\sin\theta] = (R_T + r_p)(1 - \sin\theta). \tag{E.1}$$

If $l < 2r_p$ the volume of the projectile below height l can be calculated by adding cylinders of thickness dh and base a at height h above the bottom of the projectile. The base at height h must satisfy $(r_p - h)^2 + a^2 = r_p^2$, so that

$$V_\alpha = \int_0^l \pi a(h)^2\, dh = \int_0^l 2\pi r_p h\, dh - \int_0^l \pi h^2\, dh = \pi r_p l^2 - \frac{\pi l^3}{3}. \tag{E.2}$$

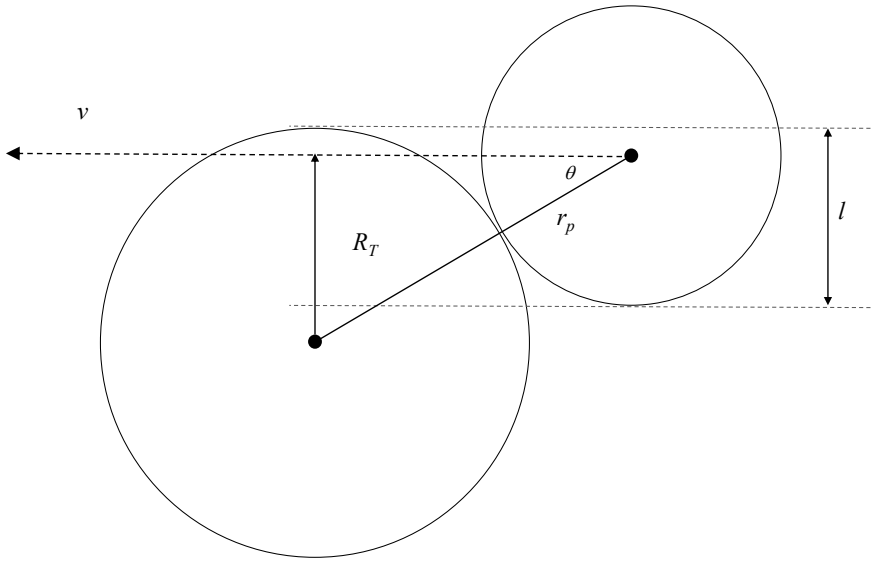

Figure E.1: Diagram of collision geometry at the moment of impact.

Dividing by the total volume of the projectile we find the fraction of projectile mass intersected by the target:

$$\alpha = \begin{cases} \frac{3r_p l^2 - l^3}{4r_p^3}, & l < 2r_p. \\ 1, & l \geq 2r_p \end{cases} \tag{E.3}$$

In the center-of-mass frame the kinetic energy available in the collision is then

$$K_\alpha = \frac{1}{2}\alpha m_p v_p^2 + \frac{1}{2} M_T v_T^2, \tag{E.4}$$

where the velocities v_p and v_T are relative to the center of mass. If the projectile and target centers are at $\mathbf{x}_p$ and $\mathbf{x}_T$, respectively, then the center of mass is at

$$(m_p \mathbf{x}_p + M_T \mathbf{x}_T)/(M_T + m_p) = \mathbf{0}. \tag{E.5a}$$

To express the kinetic energy in terms of the *relative* velocity v we write the target and projectile

positions in terms of the relative position vector:

$$\mathbf{x} = \mathbf{x}_T - \mathbf{x}_p, \tag{E.5b}$$

$$\mathbf{x}_p = -\frac{M_T}{M_T + m_p}\mathbf{x}, \tag{E.5c}$$

and

$$\mathbf{x}_T = \frac{m_p}{M_T + m_p}\mathbf{x}. \tag{E.5d}$$

Differentiating eqs. (E.5) with respect to time and plugging into eq. (E.4) we get

$$K_\alpha = \frac{1}{2}\Big(\frac{m_p M_T}{m_p + M_T}\Big)\Big(\frac{\alpha M_T + m_p}{m_p + M_T}\Big)v^2. \tag{E.6}$$

Appendix F

Derivation of power law scaling of Q_D^*

Housen and Holsapple (1990) derive several scaling laws for impact phenomena for both strength and gravity dominated bodies from dimensional considerations and experimental evidence. Here we re-derive eq. (F.7) (*Housen and Holsapple*, 1990, eq. 48) in a much simplified way that sacrifices generality for brevity.

The fundamental assumption is that the measure of the projectile (assumed to be much smaller than the target) that determines the outcome of the collision is not its size and velocity independently but rather some product of them, such that a smaller projectile moving faster will result in the same outcome as a larger projectile moving slower, at least for any quantity measured far from the impact site and at times long compared with the time scale of the impact itself. This assumption leads to the definition of the *coupling parameter*

$$C = m_p v^{\tilde{\mu}}, \tag{F.1}$$

where $1 \leq \tilde{\mu} \leq 2$. (*Housen and Holsapple* (1990) use a more general definition that allows the radius and density of the projectile to enter the coupling parameter in a combination that is not necessarily the mass of the projectile. They therefore have a second undetermined power index for the projectile's density, which is carried throughout the analysis only to be set at the end to

the value that makes the combination of size and density be, in fact, just the mass. Assuming from the start that it the mass of the projectile that controls its "heavyness" rather than its size and density to some unknown power is what simplifies the following greatly.)

The mass of the largest post-collision bound fragment, $M_{\rm LB}$, is an unknown function of the following:

$$M_{\rm LB} = F(M_T, R_T, C, G) \tag{F.2}$$

where G is the universal constant of gravity. The pi theorem says there should be a relationship between two dimensionless parameters made from these variables. We can choose:

$$\frac{M_{\rm LB}}{M_T} = F(\Pi_g) \tag{F.3}$$

where F is a (different) unknown function and

$$\Pi_g = C G^{-\tilde{\mu}/2} M_T^{-\tilde{\mu}/2-1} R_T^{\tilde{\mu}/2}. \tag{F.4}$$

For some particular constant value Π_g^* the parameter $M_{\rm LB}/M_T$ will equal one half. Consequently, for given values of M_T and R_T, there will be a single value C^* such that

$$\Pi_g^* = C^* G^{-\tilde{\mu}/2} M_T^{-\tilde{\mu}/2-1} R_T^{\tilde{\mu}/2}. \tag{F.5}$$

For comparison with experimental results it is convenient to rewrite eq. (F.5) in terms of the variable $Q = 0.5 m_p v^2/M_T$:

$$\Pi_g^* = 2Q^* G^{-\tilde{\mu}/2} M_T^{-\tilde{\mu}/2} R_T^{\tilde{\mu}/2} v^{\tilde{\mu}-2}. \tag{F.6}$$

Replacing target mass with an assumed average density ρ we get the *Housen and Holsapple* (1990) result:

$$Q^* \propto \rho^{\tilde{\mu}/2} G^{\tilde{\mu}/2} R_T^{\tilde{\mu}} v^{2-\tilde{\mu}}. \tag{F.7}$$

The only thing to note is that since we started with a slightly different coupling parameter our power index $\tilde{\mu}$ is different from their power index μ, but of course actual powers of R_T and v are the same. (The relationship is $\tilde{\mu} = 3\mu$.)

Note that the dimensional analysis relies on the fact that m_p and v cannot appear in equations except in the combination C. The fundamental result is eq. (F.5) not eq. (F.6) or eq. (F.7). We can rearrange eq. (F.5) using different variables but we cannot expect the same scaling law to hold between other variables like $Q^*_{\rm RD}$ and $R_{\rm C1}$. We also have no reason to expect the coupling parameter assumption to hold when the projectile is comparable in size and mass to the target. For example, in the gravity regime the gravitational potential of the projectile is surely important in determining the outcome of the collision. So the projectile mass and radius have an effect on the outcome that is not coupled to the impact speed at all. The interacting mass fraction is another variable that depends on projectile size but not its velocity. And of course there could be other factors.

Bibliography

A'Hearn, M., M. J. S. Belton, W. A. Delamere, L. M. Feaga, D. Hampton, J. Kissel, K. P. Klaasen, L. a. McFadden, K. J. Meech, H. Melosh, P. H. Schultz, J. M. Sunshine, P. C. Thomas, J. Veverka, D. D. Wellnitz, D. Yeomans, S. Besse, D. Bodewits, T. J. Bowling, B. Carcich, S. M. Collins, T. L. Farnham, O. Groussin, B. Hermalyn, M. S. Kelley, J.-Y. Li, D. J. Lindler, C. Lisse, S. a. McLaughlin, F. Merlin, S. Protopapa, J. Richardson, and J. L. Williams (2011), EPOXI at comet Hartley 2., *Science (New York, N.Y.)*, *332*(6036), 1396–400, doi: 10.1126/science.1204054.

Albert, R., I. Albert, D. Hornbaker, P. Schiffer, and A.-L. Barabási (1997), Maximum angle of stability in wet and dry spherical granular media, *Physical Review E*, *56*(6), R6271–R6274, doi: 10.1103/PhysRevE.56.R6271.

Asphaug, E. (2009), Growth and Evolution of Asteroids, *Annual Review of Earth and Planetary Sciences*, *37*(1), 413–448, doi: 10.1146/annurev.earth.36.031207.124214.

Asphaug, E. (2010), Similar-sized collisions and the diversity of planets, *Chemie der Erde - Geochemistry*, *70*(3), 199–219, doi: 10.1016/j.chemer.2010.01.004.

Asphaug, E., and W. Benz (1994), Density of comet ShoemakerLevy 9 deduced by modelling breakup of the parent'rubble pile', *Nature*, *370*(6485), 120–124.

Asphaug, E., and W. Benz (1996), Size, density, and structure of Comet Shoemaker-Levy 9 inferred from the physics of tidal breakup, *Icarus*, *121*, 225–248.

Asphaug, E., and H. Melosh (1993), The Stickney impact of Phobos: A dynamical model, *Icarus*, *101*(1), 144–164.

Asphaug, E., and A. Reufer (2013), Late origin of the Saturn system, *Icarus*, *223*(1), 544–565, doi: 10.1016/j.icarus.2012.12.009.

Asphaug, E., E. Ryan, and M. T. Zuber (2002), Asteroid interiors, *Asteroids III*, pp. 463–484.

Barr, A. C., and R. M. Canup (2010), Origin of the Ganymede–Callisto dichotomy by impacts during the late heavy bombardment, *Nature Geoscience*, *3*(3), 164–167, doi: 10.1038/ngeo746.

Belton, M. J. S., T. H. Morgan, N. H. Samarasinha, and D. Yeomans (2004), Mitigation of Hazardous Comets and Asteroids, in *Mitigation of Hazardous Comets and Asteroids*.

Benz, W., and E. Asphaug (1994), Impact simulations with fracture. I. Method and tests, *Icarus*, *107*(1), 98–116.

Benz, W., and E. Asphaug (1995), Simulations of brittle solids using smooth particle hydrodynamics, *Computer physics communications*, *87*(1-2), 253–265.

Benz, W., and E. Asphaug (1999), Catastrophic disruptions revisited, *Icarus*, *142*, 5–20.

Besserer, J., F. Nimmo, J. H. Roberts, and R. T. Pappalardo (2013), Convection-driven compaction as a possible origin of Enceladus's long wavelength topography, *Journal of Geophysical Research: Planets*, *118*(5), 908–915, doi: 10.1002/jgre.20079.

Boss, A. (1994), Tidal disruption of periodic comet Shoemaker-Levy 9 and a constraint on its mean density, *Icarus*, *107*, 422–426.

Bottke, W. F., and H. Melosh (1996), Binary Asteroids and the Formation of Doublet Craters, *Icarus*, *124*(2), 372–391, doi: 10.1006/icar.1996.0215.

Bottke, W. F., D. C. Richardson, and S. G. Love (1997), Can Tidal Disruption of Asteroids Make Crater Chains on the Earth and Moon?, *Icarus*, *126*(2), 470–474.

Canup, R. M. (2005), A Giant Impact Origin of Pluto-Charon, *Science*, *307*, 546–550, doi: 10.1126/science.1102556.

Canup, R. M. (2010), Origin of Saturn's rings and inner moons by mass removal from a lost Titan-sized satellite., *Nature*, *468*(7326), 943–6, doi: 10.1038/nature09661.

Canup, R. M., and E. Asphaug (2001), Origin of the Moon in a giant impact near the end of the Earth's formation., *Nature*, *412*(6848), 708–712, doi: 10.1038/35089010.

Chambers, J. (2013), Late-stage planetary accretion including hit-and-run collisions and fragmentation, *Icarus*, *224*(1), 43–56, doi: 10.1016/j.icarus.2013.02.015.

Chandrasekhar, S. (1961), *Hydrodynamic and hydromagnetic stability*, Oxford University Press.

Charnoz, S., A. Morbidelli, L. Dones, and J. Salmon (2009), Did Saturn's rings form during the Late Heavy Bombardment?, *Icarus*, *199*(2), 413–428, doi: 10.1016/j.icarus.2008.10.019.

Charnoz, S., A. Crida, J. C. Castillo-Rogez, V. Lainey, L. Dones, O. Karatekin, G. Tobie, S. Mathis, C. Le Poncin-Lafitte, and J. Salmon (2011), Accretion of Saturn's mid-sized moons during the viscous spreading of young massive rings: Solving the paradox of silicate-poor rings versus silicate-rich moons, *Icarus*, *216*(2), 535–550, doi: 10.1016/j.icarus.2011.09.017.

Chen, E. M. A., and F. Nimmo (2008), Implications from Ithaca Chasma for the thermal and orbital history of Tethys, *Geophysical Research Letters*, *35*(19), L19,203, doi: 10.1029/2008GL035402.

Chodas, P., and D. Yeomans (1996), The orbital motion and impact circumstances of Comet Shoemaker-Levy 9, in *The Collision of Comet Shoemaker-Levy 9 and Jupiter*, edited by K. Noll, H. Weaver, and P. Feldman, pp. 1–30, Cambridge Univ. Press, Cambridge.

Committee to Review Near-Earth Object Surveys and Hazard Mitigation Strategies Space Studies Board (2010), *Defending Planet Earth:Near-Earth Object Surveys and Hazard Mitigation Strategies*, The National Academies Press.

Crawford, D., M. Boslough, T. Trucano, and A. Robinson (1995), The impact of periodic comet Shoemaker-Levy 9 on Jupiter, *International journal of impact engineering*, *17*(1-3), 253–262.

Crida, A., and S. Charnoz (2012), Formation of Regular Satellites from Ancient Massive Rings in the Solar System, *Science*, *338*.

Davis, D., C. R. Chapman, R. Greenberg, S. J. Weidenschilling, and A. Harris (1979), Collisional evolution of asteroids: populations, rotations, and velocities, in *Asteroids*, edited by T. Gehrels, pp. 528–557, University of Arizona Press, Tucson, AZ.

Davis, D. R., C. R. Chapman, S. J. Weidenschilling, and R. Greenberg (1985), Collisional history of asteroids: Evidence from Vesta and the Hirayama families, *Icarus*, *62*, 30–53, doi: 10.1016/0019-1035(85)90170-8.

Dermott, S. F., and P. C. Thomas (1988), The Shape and Internal Structure of Mimas, *Icarus*, *73*, 25–65.

Dermott, S. F., M. Renu, and C. D. Murray (1988), Dynamics of the Uranian and Saturnian Satellite Systems: A Chaotic Route to Melting Miranda?, *Icarus*, *76*, 295–334.

Dones, L., and H. Levison (2013), The impact rate on Giant Planet satellites during the Late Heavy Bombardment, in *44th Lunar and Planetary Science Conference (2013)*.

Dones, L., C. R. Chapman, W. B. Mckinnon, H. Melosh, M. R. Kirchoff, G. Neukum, and K. Zahnle (2009), Icy Satellites of Saturn: Impact Cratering and Age Determination, in *Saturn from Cassini-Huygens*, edited by M. K. Dougherty, L. W. Esposito, and S. M. Krimigis, Johnson 1978, pp. 613–635, Springer Netherlands, Dordrecht, doi: 10.1007/978-1-4020-9217-6.

Durda, D. D., N. Movshovitz, D. C. Richardson, E. Asphaug, A. Morgan, A. R. Rawlings, and C. Vest (2011), Experimental determination of the coefficient of restitution for meter-scale granite spheres, *Icarus*, *211*(1), 849–855, doi: 10.1016/j.icarus.2010.09.003.

Fujiwara, A., P. Cerroni, D. Davis, E. Ryan, and M. di Martino (1989), Experiments and scaling laws for catastrophic collisions, in *Asteroids II*, pp. 240–265.

Fujiwara, A., J. Kawaguchi, D. Yeomans, M. Abe, T. Mukai, T. Okada, J. Saito, H. Yano, M. Yoshikawa, D. J. Scheeres, O. Barnouin-Jha, a. F. Cheng, H. Demura, R. W. Gaskell, N. Hirata, H. Ikeda, T. Kominato, H. Miyamoto, A. Nakamura, R. Nakamura, S. Sasaki, and K. Uesugi (2006), The rubble-pile asteroid Itokawa as observed by Hayabusa., *Science (New York, N.Y.)*, *312*(5778), 1330–4, doi: 10.1126/science.1125841.

Gilbert, E., D. Johnson, and S. Keerthi (1988), A fast procedure for computing the distance between complex objects in three-dimensional space, *IEEE Journal on Robotics and Automation*, *4*(2), 193–203, doi: 10.1109/56.2083.

Gladman, B., and J. Coffey (2009), Mercurian impact ejecta: Meteorites and mantle, *Meteoritics & Planetary Science*, *44*(2), 285–291, doi: 10.1111/j.1945-5100.2009.tb00734.x.

Gomes, R., H. Levison, K. Tsiganis, and A. Morbidelli (2005), Origin of the cataclysmic Late Heavy Bombardment period of the terrestrial planets., *Nature*, *435*(7041), 466–9, doi: 10.1038/nature03676.

Greenstreet, S., B. Gladman, and W. B. McKinnon (2015), Impact and cratering rates onto Pluto, *Icarus*, *258*, 267–288, doi: 10.1016/j.icarus.2015.05.026.

Hahn, J., and T. Rettig (1998), Tidal disruption of strengthless rubble piles-a dimensional analysis, *Planetary and Space Science*, *46*(11-12), 1677–1682, doi: 10.1016/S0032-0633(98)00055-5.

Hartman, W. (1978), Planet formation - Mechanism of early growth, *Icarus*, *33*, 50–61.

Holsapple, K. A. (1993), The scaling of impact processes in planetary sciences, *Annual Review of Earth and Planetary Sciences*, *21*, 333–373.

Holsapple, K. A., and P. Michel (2006), Tidal disruptions: A continuum theory for solid bodies, *Icarus*, *183*(2), 331–348, doi: 10.1016/j.icarus.2006.03.013.

Holsapple, K. A., and P. Michel (2008), Tidal disruptions II. A continuum theory for solid bodies with strength, with applications to the Solar System, *Icarus*, *193*(1), 283–301, doi: 10.1016/j.icarus.2007.09.011.

Holsapple, K. A., I. Giblin, K. R. Housen, A. Nakamura, and E. Ryan (2002), Asteroid Impacts : Laboratory Experiments and Scaling Laws, in *Asteroids III*, edited by W. F. Bottke, A. Cellino, P. Paolicchi, and R. Binzel, pp. 443–462, University of Arizona Press, Tucson.

Housen, K. R., and K. A. Holsapple (1990), On the Fragmentation of Asteroids and Planetary Satellites, *Icarus*, *84*, 226–253.

Imre, B., S. Räbsamen, and S. Springman (2008), A coefficient of restitution of rock materials, *Computers & Geosciences*, *34*(4), 339–350, doi: 10.1016/j.cageo.2007.04.004.

Jeans, J. (1917), No Title, in *Mem. R. Astron. Soc. London 62*, pp. 1–48.

Jutzi, M., P. Michel, W. Benz, and D. C. Richardson (2010), Fragment properties at the catastrophic disruption threshold: The effect of the parent bodys internal structure, *Icarus*, *207*(1), 54–65, doi: 10.1016/j.icarus.2009.11.016.

Knight, M., M. A'Hearn, D. Biesecker, G. Faury, D. Hamilton, P. Lamy, and A. Llebaria (2010), Photometric Study of the Kreutz Comets Observed by SOHO from 1996 to 2005, *The Astrophysical Journal*, *139*, 926–949.

Korycansky, D. G., and E. Asphaug (2009), Low-speed impacts between rubble piles modeled as collections of polyhedra, 2, *Icarus*, *204*(1), 316–329, doi: 10.1016/j.icarus.2009.06.006.

Kraus, R. G., L. E. Senft, and S. T. Stewart (2011), Impacts onto H2O ice: Scaling laws for melting, vaporization, excavation, and final crater size, *Icarus*, *214*(2), 724–738, doi: 10.1016/j.icarus.2011.05.016.

Leinhardt, Z. M., and S. T. Stewart (2012), Collisions Between Gravity-Dominated Bodies. I. Outcome Regimes and Scaling Laws, *The Astrophysical Journal*, *745*(1), 79, doi: 10.1088/0004-637X/745/1/79.

Longshaw, S. M., M. J. Turner, E. Finch, and R. Gawthorpe (2009), Discrete Element Modelling Using a Parallelised Physics Engine, *EG UK Theory and Practice of Computer Graphics*.

MacMillan, W. D. (1936), *Dynamics of Rigid Bodies*, 478 pp., Dover Publications, New York, New York, USA.

Marcus, R. a., D. Sasselov, S. T. Stewart, and L. Hernquist (2010), Water/Icy Super-Earths: Giant Impacts and Maximum Water Content, *The Astrophysical Journal Letters*, *719*, L45–L49, doi: 10.1088/2041-8205/719/1/L45.

Marsden, B. G. (1967), The sungrazing comet group, *The Astronomical Journal*, *72*, 1170.

Melosh, H. (1989), *Impact cratering: a geologic process*, 245 pp., Oxford University Press.

Melosh, H., and E. Whitaker (1994), Lunar crater chains, *Nature*, *369*, 713–714.

Merline, W. J., S. J. Weidenschilling, D. D. Durda, J. Margot, P. Pravec, and A. Storrs (2002), Asteroids Do Have Satellites, in *Asteroids III*, pp. 289–312.

Meyer, J., and J. Wisdom (2007), Tidal heating in Enceladus, *Icarus*, *188*(2), 535–539, doi: 10.1016/j.icarus.2007.03.001.

Monteux, J., G. Tobie, G. Choblet, and M. Le Feuvre (2014), Can large icy moons accrete undifferentiated?, *Icarus*, *237*, 377–387, doi: 10.1016/j.icarus.2014.04.041.

Morbidelli, A., W. F. Bottke, D. Nesvorný, and H. F. Levison (2009), Asteroids were born big, *Icarus*, *204*(2), 558–573, doi: 10.1016/j.icarus.2009.07.011.

Movshovitz, N., E. Asphaug, and D. G. Korycansky (2012), Numerical Modeling of the Disruption of Comet D/1993 F2 Shoemaker-Levy 9 Representing the Progenitor By a Gravitationally Bound Assemblage of Randomly Shaped Polyhedra, *The Astrophysical Journal*, *759*(2), 93, doi: 10.1088/0004-637X/759/2/93.

Movshovitz, N., F. Nimmo, D. G. Korycansky, E. Asphaug, and J. M. Owen (2015), Disruption and reaccretion of midsized moons during an outer solar system Late Heavy Bombardment, *Geophysical Research Letters*, *42*, 256–263.

Nagel, K., D. Breuer, and T. Spohn (2004), A model for the interior structure, evolution, and differentiation of Callisto, *Icarus*, *169*(2), 402–412, doi: 10.1016/j.icarus.2003.12.019.

Nesvorný, D. (2011), Young solar system's fifth giant planet?, *The Astrophysical Journal*, *742*(2), L22, doi: 10.1088/2041-8205/742/2/L22.

Nesvorný, D., D. Vokrouhlický, and A. Morbidelli (2013), Capture of Trojans By Jumping Jupiter, *The Astrophysical Journal*, *768*, 45, doi: 10.1088/0004-637X/768/1/45.

Nimmo, F., and D. G. Korycansky (2012), Impact-driven ice loss in outer Solar System satellites: Consequences for the Late Heavy Bombardment, *Icarus*, *219*(1), 508–510, doi: 10.1016/j.icarus.2012.01.016.

Noll, K., H. Weaver, and P. Feldman (1996), The Collision of Comet Shoemaker-Levy 9 and Jupiter, in *IAU Colloq. 156: The Collision of Comet Shoemaker-Levy 9 and Jupiter*, edited by K. Noll, H. Weaver, and P. Feldman.

Owen, J. M. (2010), ASPH modeling of Material Damage and Failure, in *5th International SPHERIC SPH Workshop*, pp. 297–304, Manchester, United Kingdom.

Owen, J. M. (2014), A compatibly differenced total energy conserving form of SPH, *International Journal for Numerical Methods in Fluids*, *75*, 749–775, doi: 10.1002/fld.3912.

Owen, J. M., J. Villumsen, P. Shapiro, and H. Martel (1998), Adaptive smoothed particle hydrodynamics : Methodology. II., *The Astrophysical Journal Supplement Series*, *116*, 155–209.

Pollack, J. B., O. Hubickyj, P. Bodenheimer, J. J. Lissauer, M. Podolak, and Y. Greenzweig (1996), Formation of the giant planets by concurrent accretion of solids and gas, *Icarus*, *124*, 62–85.

Richardson, D. C., W. F. Bottke, and S. G. Love (1998), Tidal Distortion and Disruption of Earth-Crossing Asteroids, *Icarus*, *134*(1), 47–76, doi: 10.1006/icar.1998.5954.

Richardson, D. C., Z. M. Leinhardt, H. Melosh, W. F. Bottke, and E. Asphaug (2002), Gravitational Aggregates : Evidence and Evolution, in *Asteroids III*, edited by W. F. Bottke, A. Cellino, P. Paolocchi, and R. Binzel, pp. 501–515, University of Arizona Press, Tucson.

Richardson, J., H. Melosh, C. Lisse, and B. Carcich (2007), A ballistics analysis of the Deep Impact ejecta plume: determining comet Tempel 1's gravity, mass, and density, *Icarus*, *190*, 357–390.

Roche, E. (1847), No Title, in *Acad. Sci. Lett. Montpelier. Mem. Section Sci. 1*, pp. 243–262.

Schenk, P., E. Asphaug, W. McKinnon, H. Melosh, and P. Weissman (1996), Cometary nuclei and tidal disruption: The geologic record of crater chains on Callisto and Ganymede, *Icarus*, *121*(2), 249–274.

Schwartz, S. R., D. C. Richardson, and P. Michel (2012), An implementation of the soft-sphere discrete element method in a high-performance parallel gravity tree-code, *Granular Matter*, *14*(3), 363–380, doi: 10.1007/s10035-012-0346-z.

Sekanina, Z., P. Chodas, and D. Yeomans (1994), Tidal disruption and the appearance of periodic comet Shoemaker-Levy 9, *Astronomy and Astrophysics*, *289*, 607–636.

Sekine, Y., and H. Genda (2012), Giant impacts in the Saturnian system: A possible origin of diversity in the inner mid-sized satellites, *Planetary and Space Science*, *63-64*, 133–138, doi: 10.1016/j.pss.2011.05.015.

Senft, L. E., and S. T. Stewart (2008), Impact crater formation in icy layered terrains on Mars, *Meteoritics & Planetary Science*, *43*(12), 1993–2013, doi: 10.1111/j.1945-5100.2008.tb00657.x.

Shoemaker, E. M., and R. Wolfe (1982), Cratering time scales for the Galilean satellites, in *Satellites of Jupiter*, edited by D. Morrison, pp. 277–339, University of Arizona Press.

Smith, B. A., L. A. Soderblom, R. Batson, F. Bridges, J. Inge, H. Masursky, E. M. Shoemaker, R. Beebe, J. M. Boyce, G. A. Briggs, A. Bunker, S. A. Collins, C. J. Hansen, T. V. Johnson, J. I. M. L. Mitchell, R. J. Terrile, A. F. Cook, J. N. Cuzzi, J. B. Pollack, G. E. Danielson, A. P. Ingersoll, M. E. Davies, G. E. Hunt, D. Morrison, T. Owen, C. Sagan, J. Veverka, R. G. Strom, and V. E. Suomi (1982), A New Look at the Saturn System: The Voyager 2 Images, *Science*, *215*(4532), 504–537, doi: 10.1126/science.215.4532.504.

Smith, B. A., L. A. Soderblom, R. Beebe, D. Bliss, J. M. Boyce, A. Brahic, G. A. Briggs, R. H. Brown, S. A. Collins, A. F. Cook, S. K. Croft, J. N. Cuzzi, G. E. Danielson, M. E. Davies, T. E. Dowling, D. Godfrey, C. J. Hansen, C. Harris, G. E. Hunt, A. P. Ingersoll, T. V. Johnson, R. G. Kraus, H. Masursky, D. Morrison, T. Owen, J. B. Plescia, J. B. Pollack, C. C. Porco, K. Rages, C. Sagan, E. M. Shoemaker, L. A. Sromovsky, C. Stoker, R. G. Strom, V. E. Suomi, S. P. Synnott, R. J. Terrile, P. C. Thomas, W. R. Thompson, and J. Veverka (1986), Voyager 2 in the Uranian System: Imaging Science Results., *Science*, *233*(4759), 43–64, doi: 10.1126/science.233.4759.43.

Solem, J. (1994), Density and size of comet Shoemaker-Levy 9 deduced from a tidal breakup model, *Nature*, *370*(6488), 349–351.

Solem, J., and J. G. Hills (1996), Shaping of Earth-crossing asteroids by tidal forces, *The Astronomical Journal*, *111*(3), 1382–1387.

Sridhar, S., and S. Tremaine (1992), Tidal disruption of viscous bodies, *Icarus*, *95*(1), 86–99, doi: 10.1016/0019-1035(92)90193-B.

Stewart, S. T., and Z. M. Leinhardt (2009), Velocity-Dependent Catastrophic Disruption Criteria for Planetesimals, *The Astrophysical Journal*, *691*(2), L133–L137, doi: 10.1088/0004-637X/691/2/L133.

Tajeddine, R., N. Rambaux, V. Lainey, S. Charnoz, A. Richard, A. Rivoldini, and B. Noyelles (2014), Constraints on Mimas' interior from Cassini ISS libration measurements., *Science (New York, N.Y.)*, *346*(6207), 322–4, doi: 10.1126/science.1255299.

Thomas, P. C. (1988), Radii , Shapes, and Topography of the Satellites of Uranus from Limb Coordinates, *Icarus*, *73*, 427–441.

Thomas, P. C. (2010), Sizes, shapes, and derived properties of the saturnian satellites after the Cassini nominal mission, *Icarus*, *208*, 395–401, doi: 10.1016/j.icarus.2010.01.025.

Tillotson, J. (1962), Metallic equations of state for hypervelocity impact, *Tech. rep.*, General Dynamics General Atomics Div, San Diego CA.

Tsiganis, K., R. Gomes, A. Morbidelli, and H. Levison (2005), Origin of the orbital architecture of the giant planets of the Solar System., *Nature*, *435*(7041), 459–61, doi: 10.1038/nature03539.

Walsh, K. J., A. Morbidelli, S. N. Raymond, D. P. OBrien, and a. M. Mandell (2012), Populating the asteroid belt from two parent source regions due to the migration of giant planets-The Grand Tack, *Meteoritics & Planetary Science*, *47*(12), 1941–1947, doi: 10.1111/j.1945-5100.2012.01418.x.

Weaver, H., M. A'Hearn, C. Arpigny, D. Boice, P. Feldman, S. Larson, P. Lamy, D. Levy, B. G. Marsden, and K. J. Meech (1995), The Hubble Space Telescope (HST) observing campaign on Comet Shoemaker-Levy 9, *Science*, *267*(5202), 1282–1288.

Weidenschilling, S. J., P. Paolicchi, and V. Zappala (1989), Do asteroids have satellites?, in *Asteroids II*, pp. 643–658.

Weissman, P., E. Asphaug, and S. Lowry (2004), Structure and density of cometary nuclei, in *Comets II*, edited by M. Festou, H. Keller, and H. Weaver, pp. 337–357, University of Arizona Press.

Zahnle, K., L. Dones, and H. Levison (1998), Cratering rates on the Galilean satellites., *Icarus*, *136*(2), 202–22.

Zahnle, K., P. Schenk, H. Levison, and L. Dones (2003), Cratering rates in the outer Solar System, *Icarus*, *163*(2), 263–289, doi: 10.1016/S0019-1035(03)00048-4.